Search for Pair Production of Supersymmetric Top Quarks in Dilepton Events at the Tevatron

By

William Johnson

B.S. (University of California, Davis) 2005

DISSERTATION

Submitted in partial satisfaction of the requirements for the degree of

DOCTOR OF PHILOSOPHY

in

Physics

in the

OFFICE OF GRADUATE STUDIES

of the

UNIVERSITY OF CALIFORNIA

DAVIS

Approved:

Robin Erbacher

John Conway

David Pellett

Committee in Charge

2010

Contents

William Casey Johnson
June 2010
Physics

Search for Pair Production of Supersymmetric Top Quarks in Dilepton Events at the Tevatron

Abstract

We search for pair production of the supersymmetric partner of the top quark, the stop quark $\tilde{t}_1$, decaying to a b-quark and a chargino $\tilde{\chi}_1^{\pm}$ with a subsequent $\tilde{\chi}_1^{\pm}$ decay into a neutralino $\tilde{\chi}_1^0$, lepton ℓ, and neutrino ν. Using 2.7 fb^{-1} of $\sqrt{s} = 1.96$ TeV $p\overline{p}$ collision data collected by the CDF II experiment, we reconstruct the mass of candidate stop events and fit the observed mass spectrum to a combination of standard model processes and stop signal. No evidence of $\tilde{t}_1\bar{\tilde{t}}_1$ production is found, therefore we set 95% C.L. limits on the masses of the stop and the neutralino for several values of the chargino mass and the branching ratio $\mathcal{B}\left(\tilde{\chi}_1^{\pm} \to \tilde{\chi}_1^0 \ell^{\pm} \nu\right)$.

0.1. Acknowledgments

This thesis is dedicated to my parents, LaVeda and Mark Johnson.

I would like to thank my advisor, Professor Robin Erbacher, for supporting, encouraging, and nurturing my development in experimental physics; always knowing what I needed in order to succeed and progress, especially when I didn't. I also owe Professor Andrew Ivanov more credit and thanks than I am able to express. He was nothing less than impressive in teaching me how to do experimental particle physics throughout the course of the research presented in this thesis. The quality and integrity of my future scientific work will greatly benefit from the opportunity to learn from and work with him.

I can't think of a better research environment than that provided by the UCD HEP group. From the professors of the third floor of the physics building who consistently go above and beyond the call of duty for students and research, to the UCD post docs located at the Tevatron who provided a pleasant and productive learning environment while always looking out for the best interests of the students. In particular I owe a special thanks to: Professor Pellet for my favorite series of classes in undergrad, electronics, and for him introducing me to research through work on the silicon Pixel detector; Professor Conway for his inspirational passion for performing research, and his class on statistics which turned a subject of mystery into my favorite part of experimental physics; Professors Chertok, Tripathi and Dr Smith for their excellent classes, and great discussions; and to the UCD post docs Tom Schwarz, Alison Lister, Aron Soha, and Andrew Ivanov, for not only always being willing to help out or answer questions, but also for the many BBQ's, lunches, discussions over drinks, and outings that made my stay at Fermilab immensely more enjoyable.

I am still amazed with the caliber of people I was privileged enough to interact with at CDF. From the conveners of the Top group to the many people who were always willing to have discussions about physics. Dr Charles Plager and Dr Thomas Junk particularly stand out in my mind. Charles helped to instill in me the level of work I should strive for, both for physics and programming. Thomas was always able to instantly provide comprehensive answers to my questions, and working with him made me really understand many things I thought I understood.

I am also thankful to all of my friends who have understood when I couldn't spend time with them, or attend their parties because of school. I am especially thankful to my good friends and rock climbing partners David Cherney and Lisa Hardy. The many trips rock climbing with these two helped me to remain sane the first two years of grad school. Starting from community college, David was perhaps the greatest influence in shaping my philosophy of and approach towards science; Lisa not only showed me how impressive the human intellect can be, but also at one point physically forced me to staying in grad school, when I otherwise wouldn't have.

I am most thankful to my family. My parents have selflessly sacrificed so much, and worked so hard to provide my sibling and I with the best opportunities they could. They unknowingly conditioned me to pursue physics when I was young, encouraged me through college, and were always there for me in grad school, even though I don't think we knew or understood where it would go or what it could be useful for. For my families unconditional love, I will always be grateful.

0.2. Introduction

The research in this thesis was performed from August 2006 though May 2009, by Andrew Ivanov, Robin Erbacher and the author. The results represent the effort of a much larger group of people however. The accelerator division at Fermilab who run the Tevatron to give the D0 and CDF experiments their data. The people at CDF who built the detector, who run the online system to collect the data, who perform offline calibrations, data handling, computing support, software creation, and much more. This research also benefited from the techniques and tools pioneered by the researchers before us, which made this this analysis possible. Additionally, many people at CDF contributed to this analysis by helping to review it's integrity, as well as suggest improvements.

CHAPTER 1

Theory of the Standard Model and Beyond

1.1. Introduction

The goal of particle physics is to develop and test a coherent and consistent mathematical framework which describes the fundamental constituents and forces of the universe. The standard model of Particle Physics (SM) embodies a significant amount of the progress and knowledge that people have gathered to this end. Of the four known fundamental forces that are believed to be the cause for all interactions and phenomena, the SM unifies and provides a predictive mathematical framework for three of them: the electromagnetic, weak, and strong forces, while ignoring the much weaker force: gravity. The SM also lists and describes the properties of the particles which compose the matter we interact with.

This chapter attempts to introduce the SM only so far as to give a flavor of how it is theoretically constructed, to motivate potential reasons why it is incomplete, and to justify the introduction to supersymmetry (SUSY), a natural extension to the theoretical framework of the SM. The experimental search for a hypothetical SUSY particle, the stop quark, is the topic of this thesis. The reader may skip to Section 1.3.2 for the essential information to understand and motivate this search for the stop quark.

1.1.1. The Standard Model. Historically, advances in physical theory have often been driven by the desire to unite seemingly unrelated phenomenon, which was often accomplished by understanding that nature obeys a symmetry we were not previously aware of. Perhaps one of the best known examples of this is the realization of the symmetry between electricity and magnetism. From the mathematical descriptions of electricity and magnetism, it was seen that these two seemingly unrelated physical effects were actually different aspects of the same phenomenon, and thus could be unified. This unification caused a better understanding of the nature of light, and caused the validity of Galilean relativity to be questioned. This unification at least partially led to the development of special relativity, which is a theory that not only unifies space and time, but also identifies the Lorentz invariance of physical law. An equation from special relativity that illustrates both of these concepts is:

$$ds^2 = dx_1^2 + dx_2^2 + dx_3^2 - c^2dt^2 = dx_1'^2 + dx_2'^2 + dx_3'^2 - c^2dt'^2 \tag{1.1}$$

Where the primed ($'$) variable indicates that the components are relative to a different inertial reference frame. This equation states that the generalized notion of distance (s) is invariant in all inertial reference frames through the combination of space and time. When this equation is combined with the fact that the speed of light is constant for all inertial observers, it gives rise to many interesting phenomena such as time dilation and length contraction. Any physical theory that obeys 1.1 is said to be Lorentz invariant, or to contain Lorentz symmetry [1].

Furthermore, if a physical system (or rather the *Lagrangian* of a system) contains a symmetry, then Noether's theorem [2] says that there is a conserved quantity related to that symmetry. A common example of this is if a Lagrangian of a system is invariant under a spatial transformation, then linear momentum will be conserved, while if the Lagrangian is invariant under rotations then angular momentum will be conserved; the conservation of energy comes from a system's Lagrangian being invariant to a translation in time. The symmetries of a Lagrangian can be classified in the framework of Group Theory, such that the generators of transformations of a symmetry form a symmetry group. For example, systems obeying 1.1 obey the Lorentz group, a subgroup of the Poincare' group [3].

The idea of a system being invariant under a symmetry is not limited to kinematic or spatial quantities though. It also applies to internal symmetries of a theory as well, with these being called gauge symmetries, which have no direct physical interpretation. An example of a theory possessing an internal symmetry is quantum electrodynamics (QED) obeying the U(1) local symmetry, which will be worked through below. The U(1) group is commonly referred to as the circle group since it represents the unit circle in the complex plain, and the fact that it is a *local* symmetry indicates each point in space-time, x, can have a different phase, $\alpha(x)$. In order for QED to obey the U(1) local symmetry, the theory must be invariant under a phase rotation through an angle $\alpha(x)$, that can vary arbitrarily from point-to-point. What this invariance is, is the subject of the next section. We will not go into the details of group theory here, but a good introduction to the subject may be found in many particle physics text books such as [4].

1.1.2. QED's invariance to U(1). To see how QED's theory is invariant to the local U(1) gauge transformation, we start with the Dirac Lagrangian, which describes a free, spin 1/2 particle with mass m, and is consistent with both special relativity and quantum mechanics:

$$\mathcal{L}_{Dirac} = \bar{\psi}\left(x\right)\left(\imath\not{\partial} - m\right)\psi\left(x\right), \ \not{\partial} \equiv \partial_\mu\gamma^\mu \tag{1.2}$$

Where the γ^μ are the 4×4 Dirac matrices [3], and ψ (the fermions "wave function") is the four-element column matrix with dimensions $[\text{mass}]^{3/2}$.

To obey the U(1) local symmetry, the Lagrangian has to be invariant under the transformation:

$$\psi\left(x\right) \rightarrow e^{\imath\alpha(x)}\psi\left(x\right) \tag{1.3}$$

The $-m\bar{\psi}\left(x\right)\psi\left(x\right)$ term of 1.2 is naturally invariant to this transformation, but the term involving a derivative is more problematic; there is no simple transformation of the $\partial_\mu\psi\left(x\right)$ term. This can be seen by taking the derivative of $\psi\left(x\right)$ in the n^μ direction:

$$n^\mu\partial_\mu\psi\left(x\right) = \lim_{\epsilon\rightarrow 0}\frac{1}{\epsilon}\left[\psi\left(x+\epsilon n\right) - \psi\left(x\right)\right] \tag{1.4}$$

Which since $\alpha\left(x\right)$ can vary arbitrarily from point-to-point (but $\alpha\left(x\right)$ is assumed to be a continuous function) leaves the limit not well defined. The easiest way to solve this problem is to create a factor $U\left(x,y\right)$ [1] that compensates for phase transformations from point x to point y. $U\left(x,y\right)$ must transform as:

$$U\left(x,y\right) \rightarrow e^{i\alpha(y)}U\left(x,y\right)e^{-\imath\alpha(x)} \tag{1.5}$$

We can set $U\left(y,y\right) = 1$, and if we require $U\left(x,y\right)$ to be pure phase, i.e. $U\left(x,y\right) = e^{i\phi(y,x)}$, then $\psi\left(y\right)$ and $U\left(y,x\right)\psi\left(x\right)$ now have the same transformation law, allowing us to define

---

[1] $U\left(x,y\right)$ is analogous to an *affine connection* used in differential geometry to allow taking directional derivatives in a non-Euclidean geometry.

a meaningful covariant derivative

$$n^{\mu}D_{\mu}\psi(x) = \lim_{\epsilon\to 0}\frac{1}{\epsilon}\left[\psi(x+\epsilon n) - U(x+\epsilon n, x)\psi(x)\right] \tag{1.6}$$

We expect the phase of $U(x,y)$ to be a continuous function of x and y however, allowing us to expand $U(x,y)$ in the separation of the two points:

$$U(x+\epsilon n, x) = 1 - \imath e\epsilon n^{\mu}A_{\mu}(x) + O(\epsilon^2) \tag{1.7}$$

where e is an arbitrarily extracted constant, and ϵn^{μ} is the coefficient of a new vector field $A_{\mu}(x)$. In general, a new field will be introduced for each generator of the underlying local symmetry the gauge theory is based on.

The covariant derivative[2] then takes the form:

$$D_{\mu} = \partial_{\mu} + \imath e A_{\mu} \tag{1.8}$$

Equation 1.8, is typically referred to as the *minimal substitution rule* and is often used *ab initio* in field theory text books.

From equations 1.7 and 1.5 it can be shown that $A_{\mu}(x)$ transforms under the local gauge transformation as:

$$A_{\mu}(x) \to A_{\mu}(x) - \frac{1}{e}\partial_{\mu}\alpha(x) \tag{1.9}$$

The vector field $A_{\mu}(x)$ is a consequence of local gauge invariance, for without it, we would not be able to write a Lagrangian involving derivatives. It can be seen that the idea of local gauge invariance leads to the definition of the covariant derivative, and also to the transformation law for the $A_{\mu}(x)$ vector field.

Replacing the derivative in equation 1.2 with the covariant derivative yields:

$$\mathcal{L} = \bar{\psi}(x)\left(\imath\gamma^{u}D_{\mu} - m\right)\psi(x) = \bar{\psi}(x)\left(\imath\gamma^{u}\partial_{\mu} - m\right)\psi(x) - e\bar{\psi}(x)\gamma^{\mu}A_{\mu}\psi(x) = \mathcal{L}_0 + \mathcal{L}_I \tag{1.10}$$

where the new term $\mathcal{L}_I$ describes the coupling between the fermion field and $A_{\mu}(x)$ field. $A_{\mu}(x)$ can be interpreted as the photon, and its coupling to the fermion is proportional to the electric charge of the fermion. So it is seen that requiring the Dirac Lagrangian 1.2 to

---

[2] As the name suggests, the covariant derivative here is analogous to geometrical covariant derivative.

be invariant under local U(1) gauge transformations naturally gives rise to the the photon field, and its interaction with charged fermion fields [3]!

Additionally we can (and should) add a kinetic term for the photon field in equation 1.10, of which the simplest term that will not destroy the gauge invariance of equation 1.10, and still affect the action, is the field strength tensor from electrodynamics [5]:

$$(\partial_\mu A_\nu - \partial_\nu A_\mu)(\partial^\mu A^\nu - \partial^\nu A^\mu) \equiv F_{\mu\nu}F^{\mu\nu} \tag{1.11}$$

Thus, giving us the entire Lagrangian for QED

$$\mathcal{L}_{QED} = \bar{\psi}(x)(\imath \not{D} - m)\psi(x) - \frac{1}{4}F_{\mu\nu}F^{\mu\nu} \tag{1.12}$$

The invariance of QED to the U(1) local symmetry illustrates how requiring the Dirac Lagrangian to be invariant under a local gauge rotation gives rise to physically meaningful consequences realized in nature, such as the existence of the photon field and the fermion's interaction with it. The idea of the Lagrangian's invariance to an internal symmetry gives rise to one of the most successful physical theories, quantum electrodynamics (QED), predicting among many other things, the anomalous magnetic dipole moment of the electron, consistent with experiment to a precision of better than one part in a trillion [6].

1.2. The Standard Model

While only representing a portion of the physics of the standard model (SM), it is fair to say the remainder of the standard model is unapologetically modeled after the theory of QED. The other two phenomena (or forces) that the standard model deals with, the weak and strong forces, are described theoretically by the internal symmetries of their respective portions of the SM Lagrangian. The strong force (QCD), responsible for binding nucleons together, is described by an SU(3) gauge theory, while the electromagnetic and weak forces are united into a SU(2)⊗U(1) gauge theory framework, where ⊗ represents the direct product.

1.2.1. Quantum Chromodynamics. The strong force of the standard model is described mathematically by quantum chromodynamics (QCD), whose name comes from the fact that particles participating in this interaction (gluons and quarks) carry "color" charge, roughly analogous to the electric charge of QED, but instead containing three aspects (often referred to as the three primary "colors"), rather than the one of QED. Only quarks and gluons carry color charge, thus they are the only fundamental particles that participate in the strong force.

Each type of quark contains a triplet of fields corresponding to the three primary colors (the fundamental representation (3)). While much like in QED, the 8 generators of SU(3) require the covariant derivative of QCD to have 8 gauge fields corresponding to the force carriers of the strong force. These are the gluons, which each carry a mixture of a color and an anti-color. The fact that gluons contain color charge means they may interact with themselves, unlike photons in QED. This greatly enrichens and complicates QCD.

From Noether's theorem it is seen that color charge is a conserved quantity, while experimentally it is found all observable particles must be color neutral. Color neutrality may be obtained by a color charge being canceled out by its respective anti-color charge (quarks contain color, anti-quarks anti-color, gluons contain both), or three different color charges may form a neutral color state. Quantum chromodynamics derives its name from the analogous relationship between color charges and the primary colors: red, blue, and green. In keeping with their namesake, the color charges are often labeled red, green, and blue.

There have been found to be three generations of quarks, with each generation of quarks having an "up" type quark with electric charge +2/3e, and a "down" type quark having charge −1/3e. Each generation of quarks is an exact copy of the other generations, with the exception of having different masses.

1.2.2. Electroweak. As previously mentioned the electromagnetic and weak sectors of the SM have been united in a SU(2)⊗U(1) framework, allowing for a consistent and elegant theoretical description. The four generators of SU(2)⊗U(1) give rise to the gauge bosons: W^+, W^-, Z^0, and massless photon. The masses of the $W^\pm$ and Z^0 bosons naively break the gauge symmetry and yield the theory non-renormalizable (the theory would contain non-physical infinities). The solution to this comes in the form of "spontaneous symmetry breaking" described in section 1.2.4, but for the moment we will proceed with a partial description of the "massless" theory.

Experimentally it is found that the $W^{\pm}$ only couples to fermions with left helicity, leading to different representations of the left and right handed components of the fermion fields, where the left and right handed components of the fields are given by $\psi_{L/R} = \frac{1}{2}\left(1 \pm \gamma_5\right)\psi$, and represented via

$$L_i = \begin{pmatrix} \nu_i \\ \ell_i \end{pmatrix}_L, \bar{\ell}_R; \quad Q_i = \begin{pmatrix} u_i \\ d_i \end{pmatrix}_L, u_R\ d_R \tag{1.13}$$

Where i is for each of the three generations of leptons (L_i), and quarks (Q_i).

The weak and electromagnetic forces are described in the SU(2)$_L$⊗U(1)$_Y$ framework, where subscript L of the SU(2)$_L$ indicates that only the left handed leptons participate in the weak interaction, and the subscript Y of U(1) indicated "weak hypercharge" is explained below. In this framework it is easiest to choose to represent the generators of SU(2) with $T_a \equiv \tau_a$ where the τ_a are the three Pauli spin matrices, such that the covariant derivative for the theory becomes $D_\mu = \partial_\mu - igA^a_\mu T^a - ig'YB_\mu$ where A^a_μ is the boson fields necessitated by SU(2), and B_μ is the field necessitated by SU(1), and Y the generator for SU(1). In terms of mass eigenstates of fields the covariant derivative is

$$D_\mu = \partial_\mu - \imath\frac{g}{\sqrt{2}}\left(W^+_\mu T^+ + W^-_\mu T^-\right) - \imath\frac{1}{\sqrt{g^2+g'^2}}Z_\mu\left(g^2T^3 + g'^2Y\right) - \imath\frac{gg'}{\sqrt{g^2+g'^2}}A_\mu\left(T^3+Y\right) \tag{1.14}$$

where $T^{\pm} \equiv \left(T^1 \pm \imath T^2\right)$.

Since this form is a bit of a mess to look at, we can identify the coefficient of the electromagnetic term as the charge of an electron e[7]:

$$e = \frac{gg'}{\sqrt{g^2+g'^2}} \tag{1.15}$$

Where for historical reasons g is often quoted in terms of G_F:

$$\frac{g}{2\sqrt{2}} = \left(\frac{M_w^2 G_F}{\sqrt{2}}\right)^{1/2} \tag{1.16}$$

However, we can introduce a further simplification through the *weak mixing angle*, θ_w, that appears in the change of basis from (A^3, B) to (Z, A):

$$\begin{pmatrix} Z \\ A \end{pmatrix} = \begin{pmatrix} \cos\theta_w & -\sin\theta_w \\ \sin\theta_w & \cos\theta_w \end{pmatrix} \begin{pmatrix} A^3 \\ B \end{pmatrix} \tag{1.17}$$

Then with the definition

$$g^2 T^3 - g'^2 Y = \left(g^2 + g'^2\right) T^3 - g'^2 Q \tag{1.18}$$

the covariant derivative becomes

$$D_\mu = \partial_\mu - \imath \frac{g}{\sqrt{2}} \left(W_\mu^+ T^+ + W_\mu^- T^-\right) - \imath \frac{g}{\cos\theta_w} Z_\mu \left(T^3 - \sin^2\theta_w Q\right) - \imath e A_\mu Q \tag{1.19}$$

and experimentally $\sin^2\theta_W = 0.23$ **??**.

Since the electric charge operator of QED does not commute with T_a, we define

$$Y \equiv 2\left(Q - T_3\right) \tag{1.20}$$

where Q is the electric charge, whose operator does commute with the T_a. The three conserved quantities of T_a are the components of "weak isospin", while Y is called the "weak hypercharge", and gives the connection between the weak and electromagnetic forces in the SU$(2)_L \otimes$U$(1)_Y$ framework.

1.2.3. Strong and Electroweak Unification. The generators of SU(3) (QCD) naturally commute with the generators of SU$(2)_L \otimes$U$(1)_Y$, meaning when the QCD and electroweak Lagrangians are combined, there is no analogous quantity to 1.20 between QCD and the electroweak portions of the SM. Thus the Lagrangian of the standard model is invariant to the internal symmetries of SU(3)$\otimes$SU$(2)_L \otimes$U$(1)_Y$.

Interestingly, the electroweak SU$(2)_L \otimes$U$(1)_Y$ is by itself, an invalid theory, due to "triangle anomalies" arising from the fact that the gauge bosons have different couplings to the left- and right-handed fermions. An example of this is a triangle diagram involving a U(1) and two SU(2) diagrams, as in figure 1.1. Diagrams of this type individually represent a nonconservation of chiral current. This nonconservation is nonexistent at the classical Lagrangian level, and only happens when the theory is quantized, through these dangerous triangle diagrams. QCD and QED are automatically immune from this concern, due to the left- and right-handed fermions having symmetric couplings (the diagram with a fermion line running one direction will be canceled out by the diagram with the fermion line running the other direction). In order for this triangle diagram to not destroy the theory, the sum of the possible diagrams must cancel, which is miraculously what happens if there is the same number of lepton generations as quark generations, provided each quark comes in three different flavors (colors). Thus, the electroweak theory requires the existence of QCD[8, 9, 10]!

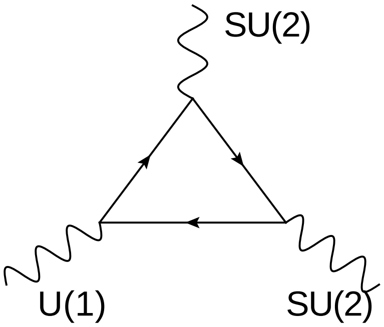

FIGURE 1.1. Diagram representing a potential nonconservation of a chiral current, which occurs when the classical Lagrangian is quantized, leading to a breaking of the global chiral symmetry. For a single species of fermion, this diagrams violates gauge invariance. In order for this anomaly, to not invalidate the theory, the sum of all possible diagrams like this must cancel, which happens if there is the same number of lepton and quark generations.

1.2.4. The Higgs Mechanism. In section 1.2.2 it was mentioned that a m^2A^2 mass term in the boson Lagrangian would violate gauge invariance. This can be resolved through “Spontaneous Symmetry breaking,” the process of introducing additional scalar fields that couple to matter and gauge boson to give them mass, and also create a preferential direction in the internal symmetries of the theory [3].

To introduce this concept, we will start with a single scalar field ϕ, which has the Lagrangian:

$$\mathcal{L} = \frac{1}{2}\left(D_\mu \phi\right)^2 - V\left(\phi\right) \tag{1.21}$$

where D_μ takes the same form of 1.8: $D_\mu = \partial_\mu - \imath g A_\mu$.

If we choose $V(\phi)$ of 1.21 to be $V(\phi) = \mu^2\phi^2 + \lambda\phi^4$, then the Lagrangian of this scalar field will remain invariant to the SU(2)⊗U(1) symmetries, while still allowing the theory to

Particle	spin	Generation	Electric Q (e)	Color Q	mass (MeV)	antipart.
u	1/2	first	+2/3	yes	1.5-3.3	$\overline{\mathrm{u}}$
d	1/2	first	−1/3	yes	3.5-6.0	$\overline{\mathrm{d}}$
s	1/2	second	−1/3	yes	70-130	$\overline{\mathrm{s}}$
c	1/2	second	+2/3	yes	1270^{+70}_{-110}	$\overline{\mathrm{c}}$
b	1/2	third	−1/3	yes	4200^{+170}_{-70}	$\overline{\mathrm{b}}$
t	1/2	third	+2/3	yes	171200 ± 2100	$\overline{\mathrm{t}}$
e^-	1/2	first	−1	no	0.511	e^+
μ^-	1/2	second	−1	no	105.66	μ^+
τ^-	1/2	third	−1	no	1776.8± 0.17	τ^+
ν_e	1/2	first	0	no	< 0.002	$\overline{\nu}_\mathrm{e}$
ν_μ	1/2	second	0	no	< 0.002	$\overline{\nu}_\mu$
ν_τ	1/2	third	0	no	< 0.002	$\overline{\nu}_\tau$
γ	1	n/a	0	no	0	γ
gluon	1	n/a	0	yes	0	$\overline{\text{gluon}}$
W^+	1	n/a	+1	no	80398 ± 25	W^-
Z	1	n/a	0	no	91187 ± 2.1	Z
Higgs	0	n/a	0	no	>114400, CL=95%	Higgs

TABLE 1.1. A summary of the particles of the standard model, as of 2008 [11]. Mass refers to a particle's bare mass, and The 'Electric Q' and 'Color Q' columns refer to electric and color charge respectively.

be renormalizable. However, the signs of μ^2 and λ will affect the behavior of the potential. If both $\mu^2 > 0$ and $\lambda > 0$ than there will be one global minimum, the vacuum state. Small fluctuations around this vacuum state correspond to a mass of μ^2 for the ϕ field. If however, $\mu^2 < 0$ then we are left with a situation where there is now no unique global minimum, ans instead we have two minimums with values $\phi_{min} = \pm\sqrt{\frac{-\mu^2}{\lambda}}$, where the vacuum expectation value of the ϕ field is now non-zero. This is the idea behind "Spontaneous Symmetry breaking."

Another interesting feature of this Lagrangian (and really the motivation for introducing it in the first place) is that when we plug in the definition of the covariant derivative into the $(D_\mu\phi)^2$ term of 1.21 we get $(\partial_\mu\phi)^2 - \imath g 2 A_\mu \phi \partial_{mu} \phi + gA^2\phi^2$ where the $gA^2\phi^2$ term takes the form of a mass term of the boson field A!

Continuing with this scalar field, we can redefine the field, so that we may expand around its minimum, ν: $\tilde{\phi} \equiv \phi - \nu$, so as to make predictions. In this case, the Lagrangian becomes:

$$\mathcal{L} = \frac{1}{2}\left(D_\mu\tilde{\phi}\right)^2 - \left(\sqrt{-2\mu^2}\right)^2\tilde{\phi}^2 - 4\lambda\sqrt{\frac{-\mu^2}{\lambda}}\tilde{\phi}^3 - \lambda\tilde{\phi}^4 \tag{1.22}$$

where we can now see the scalar field obtains a mass of $\sqrt{-2\mu^2}$, and now has a $\tilde{\phi}^3$ term making the Lagrangian no longer symmetric.

The above example illustrated how the gauge bosons can acquire mass through the introduction of a new scalar field, while still allowing the Lagrangian to obey the internal symmetries. It is a bit more complex for the standard model though, due to the existence of two massive gauge bosons, and a massless mediator. We can introduce a complex scalar doublet field that is invariant to both SU(2) and U(1) (i.e $\Phi \to e^{\imath\alpha^a\tau^a}e^{\imath\beta/2}$, where here $\tau^a = \sigma^a/2$):

$$\Phi = \begin{pmatrix} \phi^+ \\ \phi^0 \end{pmatrix}, \tag{1.23}$$

where the fields ϕ^+ and ϕ^0 are defined as:

$$\phi^+ = \frac{\phi_1 + \imath\phi_2}{\sqrt{2}} \tag{1.24}$$

$$\phi^0 = \frac{\phi_3 + \imath\phi_4}{\sqrt{2}} \tag{1.25}$$

Whose Lagrangian takes the form

$$\mathcal{L} = \left(D_\mu\phi\right)^\dagger\left(D_\mu\phi\right)^\dagger - \mu^2\phi^\dagger\phi + \lambda\left(\phi^\dagger\phi\right)^2 \tag{1.26}$$

and the covariant derivative

$$D_\mu = \partial_\mu + \imath g T^i W^i_\mu + \frac{\imath}{2}g' Y B_\mu \tag{1.27}$$

where T is the SU(2) generators, Y the U(1) generator, g and g' are the electroweak couplings given by $e = g\sin\theta_w = g'\cos\theta_w$, and experimentally $\nu = \left(\sqrt{2}G_F\right)^{1/2} \approx 246$ GeV. It can be explicitly checked that this Lagrangian is invariant to the SU(2) and SU(1) symmetries ($\phi(x) \rightarrow \phi'(x) = e^{\imath\alpha^a(x)t^a}\phi(x)$, t^a the three Pauli spin matricies, and $\phi(x) \rightarrow \phi'(x) = e^{\imath\alpha(x)}\phi(x)$). Again, 1.26 has a non-zero vacuum expectation value (VEV) when $\lambda > 0$ and $\mu^2 < 0$, so the minimum of the potential is not at zero, but at $\frac{-\mu^2}{2\lambda} \equiv \frac{\nu^2}{2}$. Through a gauge transformation (the Lagrangian *is* invariant to this) we can choose the definition of the $\phi_i(x)$ fields, such that $\langle\phi_1(x)\rangle = \langle\phi_2(x)\rangle = 0$ and $\langle\phi_3(x)\rangle = \nu$, so that the fields of 1.23, become:

$$\Phi = \frac{1}{\sqrt{2}}\begin{pmatrix} 0 \\ \nu + H(x) \end{pmatrix}, \quad \langle\Phi\rangle = \frac{1}{\sqrt{2}}\begin{pmatrix} 0 \\ \nu \end{pmatrix}, \tag{1.28}$$

which plugging into 1.26, and explicitly evaluating matrix products using $\tau^a = \sigma^a/2$ gives

$$\Delta\mathcal{L} = \frac{1}{2}\frac{\nu^2}{4}\left[g^2\left(A^1_\mu\right)^2 + g^2\left(A^2_\mu\right) + \left(-gA^3_\mu + g'B_\mu\right)\right] \tag{1.29}$$

From which we can identify the three massive gauge bosons:

$W^\pm_\mu = \frac{1}{\sqrt{2}}\left(A^1_\mu \mp \imath A^2_\mu\right)$, with mass $m_W = g\frac{\nu}{2} = \frac{e}{\sin\theta_w}\frac{\nu}{2}$

$Z_\mu = \frac{1}{\sqrt{g^2+g'^2}}\left(gA^3_\mu - g'B_\mu\right)$, with mass $m_Z = \sqrt{g^2+g'^2}\frac{\nu^2}{2} = \frac{m_W}{\cos\theta_w}$

With the fourth vector field remaining massless, and orthogonal to Z_μ

$A_\mu = \frac{1}{\sqrt{g^2+g'^2}}\left(g'A^3_\mu + gB_\mu\right)$, with mass $M_A = 0$

which we previously associated with the photon field in equation 1.15.

In 1.28 we were able to represent perturbations around the vacuum state the field $H(x)$ with mass $m_H = \nu\sqrt{2\lambda} = \left(\frac{\sqrt{2}}{G_F}\right)^{1/2}\sqrt{\lambda}$, but we have not yet accounted for the degrees of freedom (DOF) associated with the other scalar fields we introduced, or accounted for the fact that we broke the gauge symmetry in the ground state by choosing a particular gauge in 1.28. Fortunately, t' Hooft and Veltman [12] have proven that theories with spontaneously broken symmetries can still be renormalized, and as for the DOF, Goldstone's theorem states that whenever a continuous symmetry is spontaneously broken, there is one scalar particle, a Goldstone boson for each generator of the symmetry that is broken, and that for theories with gauge symmetry, the Goldstone bosons are "eaten" by the gauge bosons to give the gauge bosons their mass and become the required longitudinal polarization of the massive gauge bosons: $W^{\pm}$, and Z. While the masses of fermions, e, μ, and τ, in the SM are also given by the existence of the Higgs field and are generated by terms of the form $\mathcal{L}_{mass} = \frac{m_\ell}{\nu} H \bar{\psi}_\ell \psi_\ell$, where ℓ is any of the three lepton generations, while the neutrinos remain massless[3] , quark masses are given by similar terms.

1.2.5. Additional Remarks on the Standard Model. This introduction to the standard model has been incredibly terse, and left out many rich areas of study, instead describing (however superficially) the basis of the theory on gauge symmetry principles. The reason for the superficialness is that this is an experimental thesis, and the reason for the focus on the gauge theory aspect, is to provide motivation for the super symmetry extension to the standard model, of which the search for is the focus of this thesis. The focus of this section is to fill in a small amount of remaining details of the SM and field theories in general, that are useful for this document.

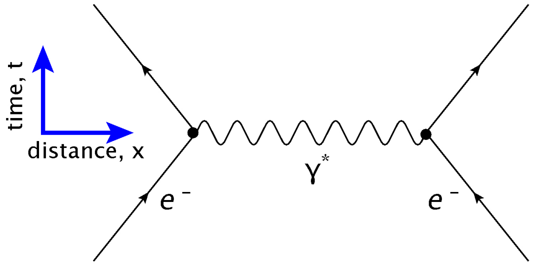

Figure 1.2. A Feynman diagram representing repulsion of two positrons, at lowest order in perturbation theory. Note that the 'y' axis can be thought of as time, while 'x' axis as distance; at times this convention may be reversed. This diagram may be interpreted as two electrons exchanging a photon, resulting in a repulsion between them.

1.2.5.1. *Feynman Diagrams.* As in Figures 1.1 and 1.2, a particularly good, and popular way of representing physical processes in field theories in general, is through the use of Feynman diagrams. The beauty of Feynman diagrams is that in addition to providing a visual representation of the process, the diagram also corresponds to a mathematical equation representing a probability amplitude (a complex number) for that process to occur. A particular order of perturbation theory is represented by drawing all of the topologically

---

[3] It has been found that neutrinos do in fact have a small mass, and the SM can be made to accommodate this, but it is generally regarded as an aesthetically unpleasing patch, and we can safely ignore these small masses [13]

distinct Feynman diagrams not violating any conserved quantities, with a given number of vertices. Each vertex introduces an additional vertex coupling factor: for example the QED coupling factor is $\alpha_{QED} = \frac{e^2}{4\pi\epsilon_0\hbar c}$. Rules for drawing and computing diagrams may be found in [4, 3].

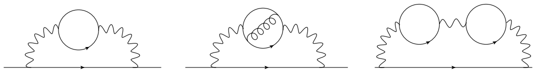

FIGURE 1.3. Some example interactions of the electron with itself, causing corrections to α_{QED}.

1.2.6. Coupling Constants. In section 1.2.5.1 it was mentioned that each vertex of a Feynman diagram represents a coupling between fields, which is associated with a numerical factor for the strength of this interaction. For low energy QED this numerical factor is $\alpha_{QED} = \frac{e^2}{4\pi\epsilon_0\hbar c} \approx 1/137.036$[4], which is readily identified as the Fine-structure constant from classical Electricity and Magnetism (E&M)[5]. There is however a difference between the classical coupling constant of E&M, and that of QED: QED's coupling "constant" is not a constant, but rather is dependent on the energy of the interaction; this is also true of other field theory couplings. The value of the coupling for a given energy (or rather distance) scale may be computed through the use of the ***renormalization group (RG)*** equations. The ***(RG)*** is related to the *scale invariance* (or mathematically *conformal invariance*) of a system, whereby the system appears the same at all scales. Perhaps the best illustration of this principle is provided by an electron:

When we "look" at an electron from a large distance (e.g. a classical distance), we do not see the bare electron, but rather we see a "dressed" electron. If we zoom in to a closer distance (or rather higher energies), we see that the electric charge will actually be slightly different than at large distances. This is caused by the electron's interactions with itself.

1.2.6.1. *Quark Mixing, Observation, and Decays.* A detail that was previously omitted is that because only left handed leptons appear in 1.13 , the lepton flavor eigenstate is the same as the lepton mass eigenstate. This means the number of leptons of each flavor (e, μ, or τ) is absolutely conserved[6], however for quarks it is not the case that the flavor and

---

[4] It may not be an accident that α_{QED} takes on this specific value, if it were to be changed by merely 4% stellar fusion would not produce carbon, an essential ingredient for life as we know it [14].

[5] which if nothing else provides some reassurance that in the low energy approximation QED is able to reproduce the results of classical E&M

[6] this is in the massless neutrino approximation

mass eigenstates coincide [11]. If we look at the charged current term of the electroweak Lagrangian, using the physical (mass) eigenstates of the particles, it looks like

$$\mathcal{L}_{CC} = \frac{g}{2}\left(\bar{u}\ \bar{c}; \bar{t}\right)\gamma^{\mu}\frac{1-\gamma_5}{2}V_{CKM}\begin{pmatrix} d \\ s \\ b \end{pmatrix} W_{\mu}^{+} + h.c., \tag{1.30}$$

where V_{CKM} is the unitary 3x3 CKM (Cabibbo-Kobayashi-Maskawa) matrix, and the mass-eigenstate of the quarks are denoted by their respective symbol (u, d, s, etc.). V_{CKM} can be written exactly in terms of three angles ϕ_{ij}, and one phase δ_{13}:

$$V_{CKM} = \begin{pmatrix} c_{12}c_{13} & s_{12}c_{13} & s_{13}e^{-\imath\delta_{13}} \\ -s_{12}c_{23} - c_{12}s_{23}s_{13}e^{\imath\delta_{13}} & c_{12}c_{23} - s_{12}s_{23}s_{13}e^{\imath\delta_{13}} & s_{23}c_{13} \\ s_{12}s_{23} - c_{12}c_{23}s_{13}e^{\imath\delta_{13}} & -c_{12}s_{23} - s_{12}c_{23}s_{13}e^{\imath\delta_{13}} & c_{23}c_{13} \end{pmatrix} \tag{1.31}$$

$$= \begin{pmatrix} V_{ud} & V_{us} & V_{ub} \\ V_{cd} & V_{cs} & V_{cb} \\ V_{td} & V_{ts} & V_{tb} \end{pmatrix}$$

Where $c_{ij} = \cos\theta_{ij}$, and $s_{ij} = \sin\theta_{ij}$ (i, $j = 1$, 2, 3), and we can identify the Cabibbo angle as θ_{12} by the relation $\sin\theta_{12} \approx 0.22$.

We can interpret the elements of the CKM matrix V_{ij}, as being proportional to the probability of quark i transitioning into quark j. In terms of the bra-ket notation, we can represent the weak eigenstates $\mid q'\rangle$ in terms of the mass eigenstates $\mid q\rangle$ by:

$$\begin{bmatrix} \mid d'\rangle \\ \mid s'\rangle \\ \mid b'\rangle \end{bmatrix} = \begin{bmatrix} V_{ud} & V_{us} & V_{ub} \\ V_{cd} & V_{cs} & V_{cb} \\ V_{td} & V_{ts} & V_{tb} \end{bmatrix} \begin{bmatrix} \mid d\rangle \\ \mid s\rangle \\ \mid b\rangle \end{bmatrix} \tag{1.32}$$

Where current fits to experimental data give the magnitude of V_{ij} as:

$$|V| = \begin{pmatrix} 0.97419 \pm 0.00022 & 0.2257 \pm 0.0010 & 0.00359 \pm 0.00016 \\ 0.2256 \pm 0.0010 & 0.97334 \pm 0.00023 & 0.0415^{+0.0010}_{-0.0011} \\ 0.00874^{+0.00026}_{-0.00037} & 0.0407 \pm 0.0010 & 0.999133^{+0.000044}_{-0.000043} \end{pmatrix} \tag{1.33}$$

Allowing us to recognize that top quarks will almost always decay to bottom quarks, strange to charm, down to up. We can schematically represent the bottom quark decay as $V_{cb}\left(b \rightarrow cW^{-^{*}}\right) + V_{ub}\left(b \rightarrow uW^{-^{*}}\right)$ [15] showing us that b-quarks most often decay to charm quarks, while down quarks always decay to up quarks, due to this being the only kinetically available weak decay.

1.2.7. Strengths and Weakness of the Standard Model. To date, no appreciable deviations have been observed from the SM[7], and many successful predictions have been made. For instance, the existence of the W and Z bosons, gluons, charm and top quarks were all predicted before experimental observation, with their measured properties in good agreement with predictions. For instance, the W boson was predicted to have a mass of 80.3900 ± 0.0180 GeV, and measured to have a mass of 80.398 ± 0.025 GeV, with a similarly accurate prediction for the Z mass, and many other impressive predictions[7].

Even though the SM is consistent with everything we have observed so far, many criticize it, for many reasons, including: it does not account for gravity, the higgs boson has yet to be observed, it requires 18 numerical constants (with another 7 or 8 to explain neutrino masses) must be determined from experiment, the hierarchy problem (e.g. why the Planck scale is so different from the weak scale), and it does not account for dark matter or dark energy.

1.3. Extending the Standard Model with SuperSymmetry

Perhaps the best motivation for extending the SM would be "Whatever is not forbidden is mandatory,"[8] and there is actually another symmetry that can be imposed without spoiling the SM Lagrangian. The SM Lagrangian can be extended to include a supersymmetric symmetry, one that transforms under the spinor representation, such that a supersymmetric transformation turns a bosonic state into a fermionic state, and vice versa.

Possibly a more sane reason for introducing supersymmetry, other than "there is no reason not to" is to solve the so-called Hierarchy problem. The mass of the Higgs boson receives quantum corrections from all particles that couple (directly or indirectly) to it. The problem is that these corrections can be enormous due to diagrams such as Figure 1.4. A

---

[7] Besides for the finding neutrinos have mass, which the SM can be made to accommodate

[8] This statement is generally attributed to either Murray Gell-Mann or to Richard Feynman, with some favor going to the latter. Either way it was probably inspired from W. H. Auden's poem "Talking to Myself".

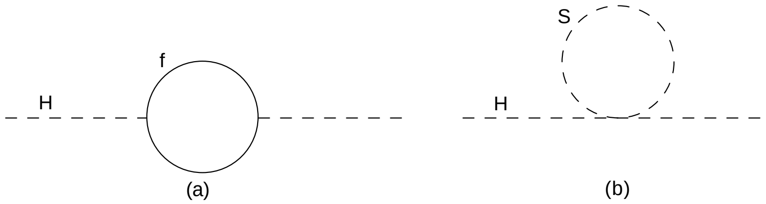

FIGURE 1.4. Diagrams representing the one loop corrections to the Higgs squared mass parameter m_H^2 for (a) a fermion f, (b) a scalar S.

fermion f that couples to the Higgs field via a term $-\lambda_f H \psi_{\bar{f}} \psi_f$ in the Lagrangian, provides a correction to the Higgs mass of:

$$\Delta m_H^2 = -\frac{|\lambda_f|^2}{8\pi^2}\Lambda_{UV}^2 + \cdots \tag{1.34}$$ [9]

Where here Λ_{UV} is an ultraviolet momentum cutoff that can be interpreted as the energy scale to which the physics model is considered valid, with M_{Planck}[10] is often used since this is about the energy scale that gravity is expected to become important. This then says the *correction* to the higgs mass is about 30 orders of magnitude larger than the required value of $m_H^2 \sim -(100\text{ GeV})^2$[11]. This implies that the theory is incredible sensitive to not only Λ_{UV} but also to m_f, where the heavier fermions contribute more to the Higgs mass[12]. Although fermion and gauge boson masses do not suffer from such dramatic quantum corrections since their mass corrections do not have terms proportional to Λ_{UV}^2, they are still affected by this unpleasant behavior since these particles do obtain their masses via the Higgs boson. The fact that M_{Planck} and the weak scale vary so drastically requires an unnatural amount of fine tuning, and is often a source of harsh criticism of the SM.

As before, when particle physicists run into a problem, or are lacking an explanation, they turn to symmetry. The symmetry that can solve the Hierarchy problem can be found by noticing that a complex scalar particle who couples to the Higgs boson via a term

---

[9] The ellipses represent terms proportional to m_f^2 and at most logarithmic in Λ_{UV}

[10] $M_{Planck} = \sqrt{\frac{\hbar c}{G}} \approx 1.2209 \times 10^{19}\ \text{GeV}/c^2$

[11] $m_H^2 \sim -(100\text{ GeV})^2$ is required to reconcile experimental data

[12] Other regularization schemes can be used where Λ_{UV} is not invoked, but these schemes have other non-desirable properties

$-\lambda_S |H|^2 |\psi_S|^2$ (as in Figure 1.4(b)) gives a mass squared correction to the Higgs of:

$$\Delta m_H^2 = \frac{\lambda_S}{16\pi^2} \left[\Lambda_{UV}^2 - 2m_S^2 \ln\left(\Lambda_{UV}/m_S\right) \cdots\right] \tag{1.35}$$

If there is a symmetry such that for every fermion there is two complex scalar particles (and similarly for gauge bosons) with $\lambda_S = |\lambda_f|^2$[13], then the Λ_{UV}^2 terms in equations 1.34 and 1.35 will cancel[14], thus solving the Hierarchy problem! This is exactly what extending the SM with *supersymmetry* does.

We can schematically represent the symmetry operator of SUSY as:

$$Q \mid Boson\rangle = \mid Fermion\rangle, \qquad Q \mid Fermion\rangle = \mid Boson\rangle \tag{1.36}$$

Where Q, satisfies the following anti-commutation and commutation relations

$$\{Q, Q^\dagger\} = P^\mu, \tag{1.37}$$

$$\{Q, Q\} = \{Q^\dagger, Q^\dagger\} = 0, \tag{1.38}$$

$$[P^\mu, Q] = [P^\mu, Q^\dagger] = 0, \tag{1.39}$$

P^μ is the four-momentum generator of spacetime translations, and spinor indices of Q have been suppressed. Also, the supersymmetry generators commute with the gauge transformations.

We can extend the SM to a supersymmetric theory (here we describe the so called minimal supersymmetric standard model (MSSM)) by creating a new super-partner of the existing particles (generically these particle are called *sparticles*, short for *supersymmetric particles*) with spin differing by 1/2 unit, and all other quantum numbers equal. However, to avoid a gauge anomaly similar to Fig. 1.1, we must expand the higgs sector to have two higgs particles with weak hypercharge $Y = \pm 1/2$, and the related super-partners of these particles. Altogether we get 4 spin-0 higgs: H_u^+, H_u^0, H_d^0, H_d^-; and 4 spin 1/2 higgs:

---

[13] $\lambda_S = |\lambda_f|^2$ implies $m_S = m_f$, dimensionally you might expect this since a fermion field ψ has units of $[\text{mass}]^{3/2}$, while a scalar field ϕ has units [mass]

[14] These terms will cancel for all orders of diagrams under a *supersymmetry*

$\tilde{H}_u^+$, $\tilde{H}_u^0$, $\tilde{H}_d^0$, $\tilde{H}_d^-$, where the subscripts u and d are used because only the $Y = 1/2$ Higgs particles can give mass to +2/3e charged up-type quarks, while the $Y = -1/2$ Higgs particle only gives mass to -1/3e charged particles.

A useful parameter to the phenominology of SUSY is the ratio of the vacuum expectation values for the H_u^0 and H_d^0 fields.

$$\tan\beta \equiv \nu_u/\nu_d, \quad \nu_u = \langle H_u^0 \rangle \;\; \nu_d = \langle H_d^0 \rangle \tag{1.40}$$

Where these VEVs are related to the coupling constants of section 1.2.2 g and g' by:

$$\nu_u^2 + \nu_d^2 = \nu^2 = 2m_Z^2/\left(g^2 + g'^2\right) \approx (174\ \text{GeV})^2 \tag{1.41}$$

SM fermions get a spin-0 partner who by convention get their SM partners name prepended with an 's', so generically *squarks*, *sleptons*, and *sfermions*, where the prepended 's' is short for *scalar*. The *sfermions* are symbolically represented by their SM particles symbol, with a tilde (˜) on top; for example $t \to \tilde{t}$, $\mu \to \tilde{\mu}$, etc. Actually since the left and right handed pieces of the quarks and leptons have different gauge transformation properties in the SM, each one gets its own super partner (a "left" and "right" partner $\tilde{f}_L$, and $\tilde{f}_R$), who mix to form mass eigenstates (this is a lot like the mixing of quarks in Section 1.2.6.1[15]), such that there becomes two mass eigenstates of the supersymmetric *sfermions*, $\tilde{f}_1$ and $\tilde{f}_2$ with $\tilde{f}_2$ being the heavier of the two[16]. The mixing between $\tilde{f}_L$, and $\tilde{f}_R$ is dependent upon a number of factors: one of which is the SM fermions mass, which has the implication that the first two generations of quarks and leptons typically do not mix much, while mixing in the third generation can be substantial.

The electrically neutral SM gauge bosons obtain spin 1/2 *gaugino* superpartners: γ (*photino*, $\tilde{\gamma}$), Z (*zino*, $\tilde{Z}^0$), and neutral higgs (*higgsino* $\tilde{H}^0$) which mix together to form four mass eigenstates called neutralinos $\tilde{\chi}_i^0, \;\; i = 1, 2, 3, 4$. The gluon's superpartner is the gluino ($\tilde{g}$) and the $W^{\pm}$ bosons mix with the charged higgsinos to form the mass eigenstate charginos ($\tilde{\chi}_i^{\pm}\ i = 1, 2$).

The most immediate objection to extending the SM to include SUSY is that in order for the supersymmetry to be exact, we would expect the supersymmetric particles to have

---

[15] Or rather particles that share the same quantum numbers mix together to form mass eigenstates

[16] Actually if the supersymmetry is unbroken, we expect the super-partners to have the same mass; this will be discussed shortly

Name	spin	Gauge Eigenstates	Mass Eigenstates
Higgs bosons	0	$H_u^0\ H_d^0\ H_u^+\ H_u^-$	$h^0\ H^0\ A^0\ H^\pm$
squarks	0	$\tilde{u}_L\ \tilde{u}_R\ \tilde{d}_L\ \tilde{d}_R$ $\tilde{s}_L\ \tilde{s}_R\ \tilde{c}_L\ \tilde{c}_R$ $\tilde{t}_L\ \tilde{t}_R\ \tilde{b}_L\ \tilde{b}_R$	(same) (same) $\tilde{t}_1\ \tilde{t}_2\ \tilde{b}_1\ \tilde{b}_2$
sleptons	0	$\tilde{e}_L\ \tilde{e}_R\ \tilde{\nu}_e$ $\tilde{\mu}_L\ \tilde{\mu}_R\ \tilde{\mu}_\mu$ $\tilde{\tau}_L\ \tilde{\tau}_R\ \tilde{\nu}_\tau$	(same) (same) $\tilde{\tau}_1\ \tilde{\tau}_2\ \tilde{\nu}_\tau$
neutralinos	1/2	$\tilde{B}^0\ \tilde{W}^0\ \tilde{H}_u^0\ \tilde{H}_d^0$	$\tilde{\chi}_1^0\ \tilde{\chi}_2^0\ \tilde{\chi}_3^0\ \tilde{\chi}_4^0$
charginos	1/2	$\tilde{W}^\pm\ \tilde{H}_u^+\ \tilde{H}_d^-$	$\tilde{\chi}_1^\pm\ \tilde{\chi}_2^\pm$
gluino	1/2	$\tilde{g}$	(same)
goldstino (gravitino)	1/2	$\tilde{G}$	(same)

TABLE 1.2. Particles gained when extending the standard model to the minimal supersymmetric standard model. Here sfermion mixing is assumed to be negligible for the first two families. All these particles have yet to be verified experimentally. Adapted from [16]

the same masses as their SM counterparts; clearly this can not be the case or we would have already seen the sparticles. So in order to reconcile SUSY theory with experiment, supersymmetry must be a spontaneously broken symmetry[17]. Typically the symmetry is broken in terms of a "soft" SUSY breaking that decouples the origin of the sypersymmetry breaking from the phenominological consequences, often times via a "hidden sector" that communicates with the visible MSSM sector through a some kind of a flavor-blind or gauge mediated interaction. It turns out that it really is not that important how sypersymmetry is broken, since we can essentially parametrize our ignorance by introducing terms into the effective lagrangian of SUSY that explicitly breaks the symmetry[18] which then gives rise to the sparticles potentially mixing with each other to form mass eigenstates[19], as noted above. For a summary of particles added by extending the SM to the MSSM and how they "mix" see Table 1.2.

1.3.1. Why SUSY?. Even though extending the SM to the MSSM in the general case requires there to be an additional 32 particle masses (not including the gravitino) to

---

[17] Or stated another way, the models Lagrangian is invariant under sypersymmetry, but the vacuum state is not

[18] On a practical level this is the easiest way to do it, but theorists have rigorously proved that the theory remains consistent when SUSY breaking terms are explicitly added to the Lagrangian (there are a number of different models, for doing this) see [16] or [17]

[19] This should sound very similar to the quarks in section 1.2.6.1

be measured by experiment, the situation is not so bleak. Depending on the soft SUSY breaking mechanism, the mass spectrum of SUSY particles may be completely determined by only a handful of parameters that need to be measured from experiment. In minimal supergravity models, the only currently unmeasured free parameters are M_0^2, $m_{1/2}$, A_0, μ, and b. As illustrated in Fig. 1.5, the SUSY particle masses may be determined by the running of the ***(RG)*** evolving of the soft terms down to the electroweak scale. gauge-mediated supersymmetry breaking models are similarly described by a small number of parameters, typically: Λ the scale, M_{medd} the messenger mass scale, N_5 the number of copies of minimal messengers, $\langle F \rangle$ the goldstino decay constant, and the Higgs mass parameters μ and b. Although these two models are by no means the only possible models, they are good examples that produced highly predictive models from a small number of unmeasured parameters.

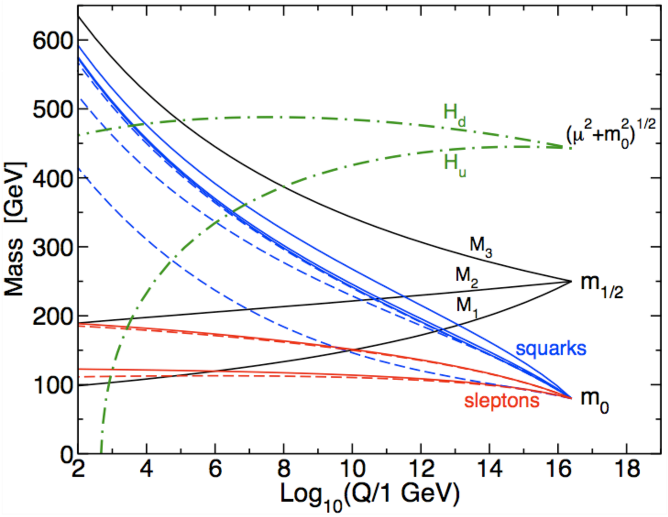

FIGURE 1.5. ***(RG)*** evolution of SUSY masses in a minimal supergravity model, showing the mass spectrum of SUSY particles may be determined by a small number of free parameter. The $\mu^2 + m_{H_u}^2$ parameter running negative provides electroweak symmetry breaking.

1.3.2. Phenomenology of the Stop Quark. Since a focus of this thesis is on a search for the top quarks supersymmetric partner the stop quark, we will look more in depth at possible SUSY scenarios involving the stop quark.

The stop quark could potentially be one of the first SUSY particles detected since the mass splitting between the first and second generations of stop quarks can potentially be very large, due to the heaviness of its SM partner the top quark. This can can be seen by the following equation for each of the superpartners mass eigenstates, in terms of the mixtures of the weak eigenstates:

$$m^2_{\tilde{t}_{2,1}} = \frac{1}{2}\left(m^2_{\tilde{t}_L} + m^2_{\tilde{t}_R} \pm \sqrt{\left(m^2_{\tilde{t}_L} - m^2_{\tilde{t}_R} \right)^2 + 4m_t^2 \left(A_t - \mu \cot\beta\right)^2} \right) \tag{1.42}$$

which given the large value of the top quark mass, means it is possible $\tilde{t}_1$ may be significantly lighter than the other squarks, and potentially of a comparable mass or lighter than the top quark. The possibility of a light stop quark means it may be the first squark to be experimentally observed, potentially at the Tevatron accelerator.

The dominant production mechanisms of the stop quark at the Tevatron accelerator are through pair production of a stop and anti-stop quark through the processes shown in figure 1.6. Although the production modes of $\tilde{t}_1\bar{\tilde{t}}_1$ are similar to that of $t\bar{t}$, the production rate of stop quarks is approximately an order of magnitude lower than top quarks of a similar mass. The main reason for this is stop quarks are scalar particles, while gluons are spin 1, meaning the $\tilde{t}_1$ and $\bar{\tilde{t}}_1$ must have some relative angular momentum to each other, which suppresses the final state phase space available to the system by a factor $\sim \frac{1}{p_T^2}$ relative to a $t\bar{t}$ system. The relatively low production cross section of stop quarks makes stop a challenging signature to search for

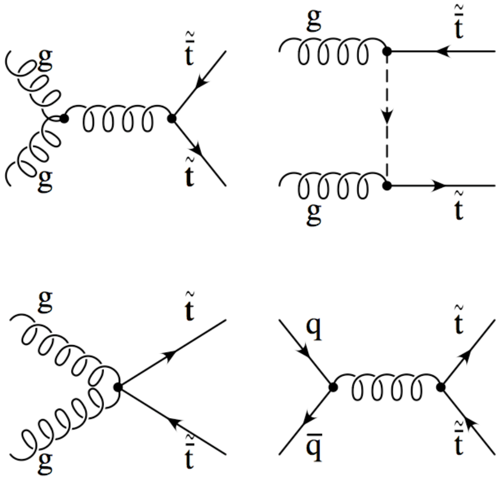

FIGURE 1.6. The dominant production mechanisms of stop quarks at the Tevatron accelerator.

1.3.2.1. *Stop Quark Decays.* How stop quarks decay is dependent on not just the mass of the stop quark itself, but also the mass hierarchy of the other SUSY particles. For instance, if the decay $\tilde{t}_1 \rightarrow t\tilde{g}$ is kinematicaly allowed, it will be the dominant decay mode. The next preferred decay is $\tilde{t}_1 \rightarrow t\tilde{\chi}_1^0$ for the right handed squarks and $\tilde{t}_1 \rightarrow t\tilde{\chi}_2^0$ or $\tilde{t}_1 \rightarrow b\tilde{\chi}_1^{\pm}$ for the left handed squarks. However, these decays can easily be kinematically forbidden, allowing the following decays:

$$\tilde{t}_1 \rightarrow c\tilde{\chi}_{1,2}^0 \tag{1.43}$$

$$\tilde{t}_1 \rightarrow b\,\chi_i^+ \tag{1.44}$$

$$\tilde{t}_1 \rightarrow W^+\,b\,\tilde{\chi}_i^0 \tag{1.45}$$

$$\tilde{t}_1 \rightarrow H^+\,b\,\tilde{\chi}_i^0 \tag{1.46}$$

$$\tilde{t}_1 \rightarrow b\,\tilde{\ell}^+\,\nu_\ell \tag{1.47}$$

$$\tilde{t}_1 \rightarrow b\,\tilde{\nu}_\ell\,\ell^+ \tag{1.48}$$

If none of the previous decay modes are open, then the stop quark may decay via the flavor-suppressed decay $\tilde{t}_1 \rightarrow c\tilde{\chi}_1^0$, or four body decay $\tilde{t}_1 \rightarrow bff'\tilde{\chi}_1^0$. These two decays may take a significant amount of time to proceed however, allowing the quarks to hadronize into composite particles [18]. For reasons presented in section 1.3.3, this thesis focuses on the decay in equation 1.44, more specifically $\tilde{t}_1 \rightarrow b\,\chi_1^+$.

1.3.3. Motivations to Look for $\tilde{t}_1 \rightarrow \tilde{\chi}_1^{\pm}b \rightarrow \tilde{\chi}_1^0\ell\nu b$. Although there are many possible decays of the stop quark, the decay searched for in this thesis can be motivated from both theoretical and experimental perspectives, making the decay $\tilde{t}_1 \rightarrow \tilde{\chi}_1^{\pm}b \rightarrow \tilde{\chi}_1^0\ell\nu b$ an especially well motived channel to consider in the search for SUSY; experimental based motivations can be found in section 4.2; while below some of the more theoretical based motivations:

- It chooses the $\tilde{\chi}_1^0$ to be lightest supersymmetric particle (LSP) as favored by the astrophysical data [11]. If one assumes R-parity, all supersymmetric particles will decay to have at least one $\tilde{\chi}_1^0$ in the final state. The mass of the neutralino must be larger than 46 GeV/c^2 from LEP searches for the LSP in the general MSSM scenario. [19, 20, 11].
- The stop quark may be similar in mass to, or lighter than the top quark. This makes it experimentally within reach to observe at the Tevatron. Also, the condition $m_{\tilde{t}_1} \lesssim m_t$ is demanded in the supersymmetric electroweak baryogenesis scenarios [21], which provide an explanation for the origin of the baryon asymmetry in the Universe.
- The $\tilde{t}_1 \to \tilde{\chi}_1^{\pm} b$ decay will be the dominant decay mode of the stop quark, with a branching ratio $\mathcal{R} \approx 100\%$ when $M_{\tilde{\chi}_1^{\pm}} < M_t - M_b$. Experimentally, we know if the $\tilde{\chi}_1^{\pm}$ exists, it must have a mass greater than between 94 and 103.5 GeV/c^2 depending on assumptions within the MSSM [22, 11]
- Choosing the chargino to decay as $\tilde{\chi}_1^{\pm} \to \tilde{\chi}_1^0 \ell \nu$, is based on the assumption that all other squarks, sleptons, and sneutrinoes are more massive than the stop quark, a reasonable assumption given equation 1.42. It also allows a potentially larger branching ratio to the dilepton final state than $t\bar{t}$ events, which helps mitigate the small $\tilde{t}_1\bar{\tilde{t}}_1$ production cross section.

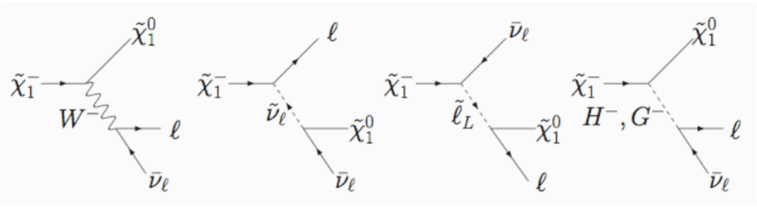

Figure 1.7. Schematics of possible decays of the chargino through off-shell particles when $M_{\tilde{\chi}_1^{\pm}} - M_{\tilde{\chi}_1^0} < M_{W^{\pm}}$.

1.3.3.1. *Previously Existing Stop Quark Limits.* Due to the the large phase space of the MSSM parameters affecting the final state event signature of stop quark events, setting

It could be stated that the minimal assumptions made in looking for stop in this final state event signature are:

(1) $\tilde{\chi}_1^0$ is the LSP, and $\tilde{q}, \tilde{\ell}, \tilde{\nu}$ are heavy
(2) $m_{\tilde{t}_1} \lesssim m_t$
(3) $m_{\tilde{\chi}_1^+} < m_{\tilde{t}_1} - m_b$

Furthermore the branching ratio of stop events decaying into the desired dilepton final state may be enhanced beyond the $t\bar{t}$ dilepton branching ratio of 0.11 if $M_{\tilde{\chi}_1^\pm} - M_{\tilde{\chi}_1^0} < M_{W^\pm}$. If $M_{\tilde{\chi}_1^\pm} - M_{\tilde{\chi}_1^0} > M_{W^\pm}$ then the chargino decay will proceed nearly exclusively via $\tilde{\chi}_1^\pm \to \tilde{\chi}_1^0 W^\pm$ and $\tilde{t}_1\bar{\tilde{t}}_1$ will give the lepton plus jets, all hadronic, and dilepton final states at the same frequency as $t\bar{t}$ events. If $M_{\tilde{\chi}_1^\pm} - M_{\tilde{\chi}_1^0} < M_{W^\pm}$ then there may be an enhancement to the dilepton decay channel, through the decays

$$\tilde{\chi}_1^\pm \to \tilde{\chi}_1^0 + W^{\pm(*)} \to \tilde{\chi}_1^0 + \ell + \nu \tag{1.49}$$

$$\tilde{\chi}_1^\pm \to \tilde{\chi}_1^0 + H^{\pm *} \to \tilde{\chi}_1^0 + \ell + \nu \tag{1.50}$$

$$\tilde{\chi}_1^\pm \to \ell + \tilde{\nu}_\ell \to \tilde{\chi}_1^0 + \ell + \nu \tag{1.51}$$

$$\tilde{\chi}_1^\pm \to \nu + \tilde{\ell}_L \to \tilde{\chi}_1^0 + \ell + \nu \tag{1.52}$$

$$\tilde{\chi}_1^\pm \to \tilde{\chi}_1^0 + G^{\pm *} \to \tilde{\chi}_1^0 + \ell + \nu \tag{1.53}$$

as depicted in figure 1.7.

limits on the mass of stop quarks is challenging. Limits for a particular scenarios considered likely to be realized in nature are listed below.

(1) $\tilde{t}_1 \to c\tilde{\chi}_1^0$: assuming $M_{\tilde{t}_1} - M_{\tilde{\chi}_1^0} > 10$ GeV/c^2, $M_{\tilde{t}_1} > 95.7$ GeV/c^2.
(2) $\tilde{t}_1 \to b\ell\tilde{\nu}_1$: assuming $M_{\tilde{t}_1} - M_{\tilde{\nu}_1} > 10$ GeV/c^2, $M_{\tilde{t}_1} > 92.6$ GeV/c^2.
(3) $\tilde{t}_1 \to b\tilde{\chi}_1^0 W^*$: assuming $M_{\tilde{t}_1} - M_{\tilde{\chi}_1^0} > 8$ GeV/c^2, $M_{\tilde{t}_1} > 78$ GeV/c^2.
(4) $\tilde{t}_1 \to b\ell\nu\tilde{\chi}_1^0$: assuming $M_{\tilde{\chi}_1^0} = 50$ GeV/c^2, $M_{\tilde{t}_1} > 80$ GeV/c^2.
(5) $\tilde{t}_1 \to \tau b$: An R-parity violating decay excluded for $M_{\tilde{t}_1} < 151$ GeV/c^2 assuming $\mathcal{B}\left(\tilde{t}_1 \to \tau b\right) = 1$ [23]

with a complete listing of searches available in Ref. [11].

Previous to the search that is the subject of this thesis, the only limits on the stop quark mass applicable to the $\tilde{t}_1 \to \tilde{\chi}_1^\pm b$ scenario is a general MSSM scalar top quark limit from the LEP collider of $M_{\tilde{t}_1} > 95.7$ GeV/c^2[11]. If one takes into account that the decay $\tilde{t}_1 \to \tilde{\chi}_1^\pm$ should be kinematically possible, then one could use the requirement $M_{\tilde{t}_1} > M_{\tilde{\chi}_1^\pm} + M_b$ putting the limit somewhere in the range of $99 \leq M_{\tilde{t}_1} \leq 108.5$ GeV/c^2. Although there had been searches at the Tevatron for larger stop masses [24, 25] in this decay mode, they failed to set any limits, primarily due to the challenge of discriminating $\tilde{t}_1\bar{\tilde{t}}_1$ events from $t\bar{t}$ events. Therefore, in addition to the theoretical arguments to search for this scenario, experimentally it remained *terra incognita*.

CHAPTER 2

Experimental Apparatus

The study of fundamental particles with masses near that of a gold nuclei requires the use of large scale particle colliders such as the Tevatron accelerator, located at the Fermi National Accelerator Laboratory (Fermilab). At the time the research for this paper was being performed, the Tevatron accelerator was the only accelerator energetic enough to produce either the top quark or it's supersymetric partner the stop quark, in the mass range probed in this thesis. The data used in this analysis was collected between March 2002 and March 2007 by the Collider Detector at Fermilab (CDF), a multi-purpose experiment which records the proton-antiproton collisions of the Tevatron accelerator. This chapter describes the accelerator, as well as the CDF detector and associated triggering systems, with an emphasis on components used in this analysis.

2.1. The Tevatron Accelerator

The Tevatron accelerator is the last in a series of accelerators shown schematically in Fig. 2.1, which makes the collision of protons and antiprotons possible [26].

2.1.1. Pre-accelerator. The protons and anti-protons which eventually collide in the center of the CDF or D0 detectors start out as atoms in a tank of very pure compressed hydrogen gas; housed in the electrically charged dome of a Crockcoft-Walton device. The hydrogen gas is passed between two electrodes which create a spark, ionizing the hydrogen into electrons and H^+ ions, which then collide with a cesium cathode. This occasionally creates a H^- ion due to cesium's low work function. The H^- ions are then subjected to a -750 kV potential from the Crockcoft-Walton to the grounded wall, thus producing an H^- beam with an energy of 750 keV, which is then focused by magnets down a transfer line to the linear accelerator (Linac).

2.1.2. Linac. The groups of H^- ions from the Crockcoft-Walton are subjected to a radio frequency (RF) electric field matched to the size and timing of the bunches, accelerating them along two sections of a 150 meter string of copper cavities. The first section of cavities is composed of 5 *drift tubes* that accelerate the ion beams to 117 MeV. The Drift tubes shield the ions from the 201 MHz RF field when it points opposite to the direction of motion, thus allowing the ions to only "feel" the electric field when it will increase their speed. The second section of the Linac is composed of 7 chambers of side coupled cavity Linac modules, that accelerate particles based on the same principle as the first section, but operate at 805 MHz to bring the beam to an energy of 400 MeV. This RF method of acceleration causes the particles to become grouped together into *bunches*. The Linac is able to accelerate the bunches at a rate of 15 Hz. As the ions leave the Linac they pass through a thin strip of foil which strips the two electrons from the hydrogen nucleus, creating a proton beam which then passes to the Booster.

2.1.3. Booster. The booster is a 75-m-radius synchrotron accelerator that accelerates the protons to 8 GeV. The acceleration is accomplished with 19 RF cavities interspersed along the 96 conventional magnets that bend the beam into a circular orbit. The booster operates at the same 15 Hz duty cycle as the Linac, but is able to hold multiple batches of particles (commonly 11 or 12) from the Linac to increase beam intensities. A set of fast kicker magnets extract the beam from the Booster, directing the protons either to the Mini Booster Neutrino Experiment, or to a transfer line that leads to the Main Injector.

2.1.4. Main Injector. The Main Injector (MI) is a circular synchrotron with a diameter of 1 km, containing 18 accelerating cavities. The MI is capable of accelerating 8 GeV protons from the Booster to either 120 GeV for sending the beam to MI neutrino experiment (NuMI) and stacking/creating antiprotons, or to 150 GeV to inject beam into the Tevatron. The MI can accept either protons from the Booster, or antiprotons from the Antiproton Source.

The MI contains contains 344 dipole bending magnets and 208 focusing quadrupole magnets, which are all water-cooled electromagnets. The MI can accelerate beams up to every 2.2 seconds, and typically operates in mixed-mode where it sends one bunch to the antiproton source and the next four to NuMI.

2.1.5. Antiproton Source. Protons from the MI are sent down a transfer line at 120 GeV of energy to a fixed nickel alloy target, where among many other particles, antiprotons are created from the resulting collisions. Antiprotons are selected by an electromagnetic selector and focused down a transfer line to the Debuncher. It takes approximately 10^5 incident protons to collect a single antiproton, which will have an average energy of 8 GeV.

2.1.6. Debuncher. The Debuncher is a rounded triangular-shaped synchrotron with a mean radius of 90 meters; it is designed to efficiently capture the newly created high momentum spread antiprotons. The Debuncher employs beam cooling systems to reduce the momentum spread of antiprotons in both the longitudinal and transverse directions, making the beam more manageable. The Debuncher maintains the beam at a constant energy of 8 GeV with no bunch structure until the next batch of protons is sent to the antiproton target, at which point the antiprotons are sent to the Accumulator.

2.1.7. Accumulator. The Accumulator is housed in the same tunnel as the Debuncher, and is designed to store the antiproton beam with minimal losses for several days. The RF systems of the Accumulator manipulate the antiprotons to minimize the momentum spread of the particles. The transverse momentum of particles is also decreased in a similar way to the Debuncher, via *stochastic cooling*, where the momentum spread of a group of particles is measured on one side of the ring, so corrector magnets on the opposite side can be used to reduce the momentum spread of those particles.

The antiprotons must be re-bunched before extraction from the Accumulator. Bunching is accomplished by adiabatic activation of RF stations, which causes a portion of the beam to become bunched. Once re-bunched, the beam is then sent to the Main Injector, where it is decelerated to 8 GeV and placed in the Recycler.

2.1.8. Recycler. The recycler is a permanent magnet synchrotron located in the same tunnel as the Main Injector. The Recycler was originally intended to recycle the antiprotons left over in the Tevatron at the end of a store, but due to technical problems early in Run II, this use for the Recycler was abandoned. Now the Recycler is used to collect antiprotons at 8 GeV until the Tevatron is ready for injection. While in the Recycler, the antiprotons are further cooled by a process called *electron cooling*. Electron cooling consists of accelerating a beam of electrons to the same energy as the antiprotons and runnning it alongside the antiprotons. The transverse momentum of the antiprotons is transfered to the much lighter electrons, which makes the beam much smaller, resulting in higher luminosities in the Tevatron. Antiprotons are transfered from the Recycler to the Main Injector where they are accelerated to 150 GeV and injected into the Tevatron.

2.1.9. Tevatron. The Tevatron is a circular accelerator with a radius of 1 km. It contains eight accelerating cavities, 774 superconducting dipole bending magnets, and 240 quadrapole focusing magnets. The superconducting magnets are cooled with liquid helium to 4.2 K, allowing the niobium-titanium alloy to become superconducting and create a maximum field of 4.2 T.

The protons and antiprotons circulate in opposite directions within the same beam pipe, being held apart by electrostatic separators. The Tevatron holds 36 bunches, each of protons and antiprotons. Each proton bunch contains approximately 10^{13} protons, while the antiproton bunches only contain about one eighth of that amount. The protons are loaded one bunch at a time into the Tevatron at an initial energy of 150 GeV from the Main Injector. The antiprotons are injected four bunches at a time from the Recycler, through the Main Injector. Once all bunches of particles are loaded, the Tevatron uses 53.1 MHz RF cavities (giving 1113 wavelength along the circumference) to accelerate the beams to 980 GeV over the course of about 90 seconds. Once at collision energies, the polarity of some of the electrostatic separators are reversed, causing the beams to interact at the B0 (the CDF detector location) and D0 (the D0 detector location) interaction regions. The low β quadrapole magnets on either side of each interaction region squeeze the beams to a diameter of about two microns, allowing on average one to ten interactions to take place per bunch crossing.

2.2. The CDF Detector

The CDF detector is a barrel shaped forward-backward and cylindrically symmetric general purpose detector. It is capable of identifying and measuring properties of the hundreds of secondary particles produced in each collision, allowing for precise investigation of the primary physics interaction. The detector is comprised of several layers, designed to maximally facilitate measuring particle properties. The innermost layer is the silicon

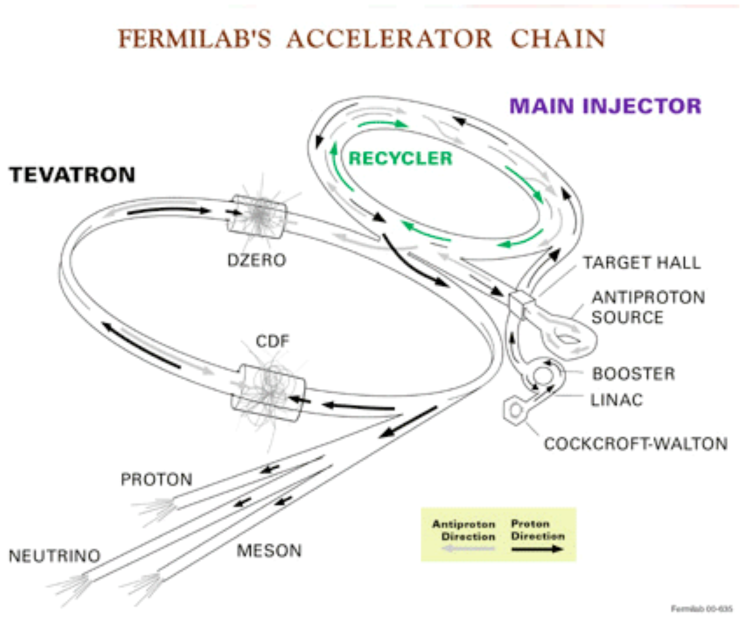

Figure 2.1. Schematic view of the Fermilab accelerator.

tracking detector which is enclosed in the central outer tracker, both of which are immersed in a 1.4 T magnetic field created by the superconducting solenoidal magnet. The tracking system is surrounded by the electromagnetic calorimeters, which are in turn surrounded by the hadronic calorimeters. Finally, the outermost layer is the muon detection systems. The detector is roughly comprised of a central barrel portion with separate endcaps on either side, giving nearly a 4π solid angle coverage of the interaction region. A more detailed description labeled subcomponents is shown in Figures 2.2 and 2.3. A complete description of the detector can be found in reference [27].

2.2.1. Coordinate System. In order to describe measurements in the detector, CDF uses a right-handed coordinate system with the positive z-axis pointing in the direction of the proton beam. As can be seen in figure 2.4, ϕ is measured relative to the vector pointing away from the center of the Tevatron, while the polar angle θ is measured relative to the z axis. Since typical interactions will be boosted in the z direction, due to the interacting partons in the proton/antiprotons not carrying equal momentum, it is more natural to instead of using θ, to use psuedo-rapidity defined by:

$$\eta = -ln\left(\tan\frac{\theta}{2}\right) \tag{2.1}$$

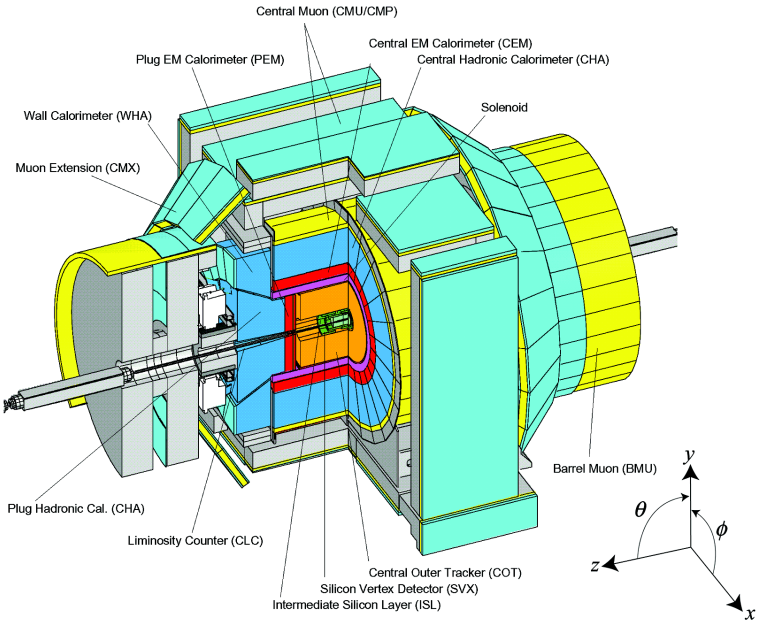

FIGURE 2.2. Overview of the CDF detector systems.

which is closely related to the Lorentz invariant *rapidity* of a particle: $y = \frac{1}{2} ln\left(\frac{E+p_z}{E-p_z}\right)$. The psuedo-rapidity of a particle becomes a good approximation of the rapidity when a particles energy is much larger than its mass, which is nearly always true at Tevatron energies. In addition to the psuedo-rapidity being invariant to the reference frame (a boost in z direction does not affect it), the density of final state particles is approximately uniform in units of psuedo-rapidity. In this thesis, when η is used to refer to a detector component, it is measured from the nominal interaction point. When referring to measured physics objects (such as a jet, lepton, or track), η is measured from the primary interaction region of that event, which may be as far as 60 cm from the nominal interaction point.

2.2.2. Luminosity Monitoring. An important part of the detector that has not been mentioned is the Cherenkov Luminosity Counter (CLC) [28], used to measure the interaction rate, or rather instantaneous luminosity, $\mathcal{L}$, of the particle beams. Instantaneous luminosity is defined by:

$$\mathcal{L} = f \frac{n_p n_{\bar{p}}}{4\pi \sigma_p \sigma_{\bar{p}}} \tag{2.2}$$

where n_p ($n_{\bar{p}}$) is the number of protons (antiprotons) in the bunches, f is the frequency of bunch crossings, and the Gaussian transverse particle densities are parametrized by σ_p and

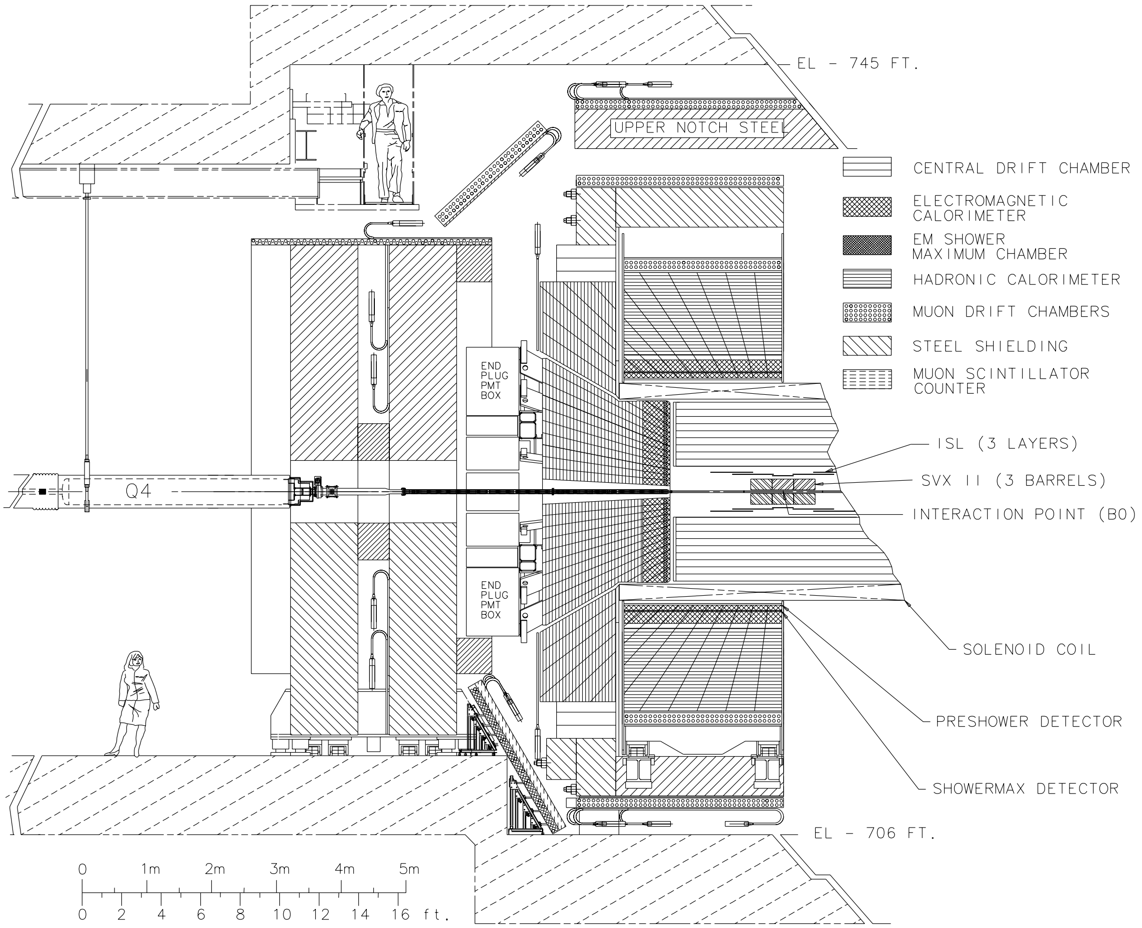

Figure 2.3. Elevated schematic view of the CDF detector.

$\sigma_{\bar{p}}$. Instantaneous luminosity is typically measured in units of $cm^{-2}s^{-1}$, with typical values at the Tevatron in the range of 50×10^{31} to 350×10^{31} $cm^{-2}s^{-1}$.

The parameters of 2.2 can not be measured well enough to accurately monitor the luminosity of the Tevatron however, so instead the CLC measures the total inclusive cross section in order to deduce the luminosity. The CLC consists of two modules located in the small 3° conical hole at high η of the forward calorimeter. Each module is constructed of aluminized mylar filled with isobutane gas. As charged particles pass through the module they emit Cherenkov light, which is detected by a fast Photo Multiplier Tube (PMT). The timing of the counters is better than 100 ps, allowing for coincidence measurements between each of the modules. The modules are designed to minimize the effects of secondary particle

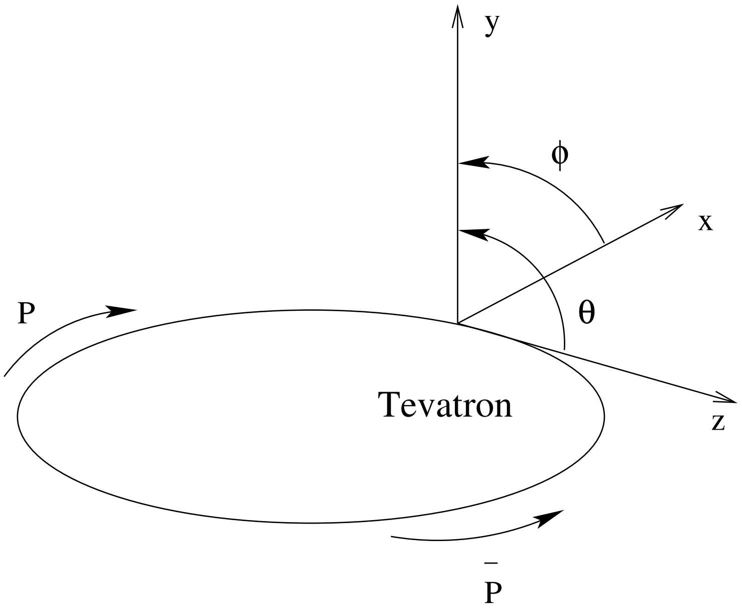

Figure 2.4. Coordinates system of the CDF experiment.

interactions as well as beam halo particles. The instantaneous luminosity is then given by:

$$\mathcal{L} = f \frac{\langle N_H \rangle}{\sigma_{in} \epsilon \langle N_H^1 \rangle} \tag{2.3}$$

where f is the bunch crossing frequency, σ_{in} is the total inelastic cross section, ϵ denotes selection inefficiencies, $\langle N_H \rangle$ is the average number of hits recorded per second, and $\langle N_H^1 \rangle$ is the number of expected hits in the CLC for a single $p\bar{p}$ collision.

The integrated luminosity, defined by:

$$L = \int \mathcal{L}\,(t)\,dt \tag{2.4}$$

is important for the normalization of simulated events in order to match the number of events expected in data. The cross section of a process multiplied by the integrated luminosity gives the expected number of events of that process to have occurred in data. Integrated luminosity is typically measured in inverse *barns* (denoted by b), where a barn is numerically equal to 10^{-24} cm^2. This thesis is based on $L = 2.8\,\text{fb}^{-1}$ of integrated luminosity. The uncertainty on L comes from a 4% acceptance uncertainty of the CLC, and a 4% uncertainty on the measured $p\bar{p}$ cross section, giving a total uncertainty of 6%.

2.2.3. Tracking. The integrated tracking system of CDF shown in figure 2.5 consists of a silicon inner tracker and an outer open cell drift chamber, both of which are embedded in a 1.4 T magnetic field to allow measuring the charge and transverse momentum of particles to an accuracy of $\sigma\left(p_T\right) \approx 0.0015 p_T^2 \left[\mathrm{GeV}/c\right]^{-1}$, with a track impact parameter (defined in section 3.1.4.3) resolution of 30 microns.

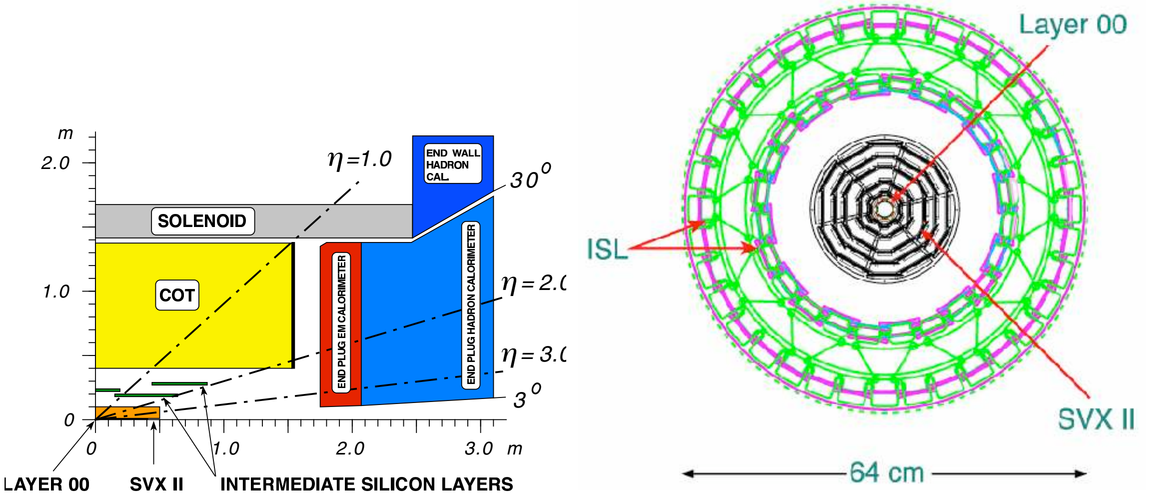

FIGURE 2.5. Pseudo rapidity coverage provided by tracking systems (left) and a cross sectional view of the silicon detector system (right).

2.2.3.1. *Silicon Detectors.* The silicon inner tracker is composed of three separate detectors: the inner most detector is the Layer00 detector (L00), attached to the beampipe itself; next there is the Silicon Vertex Detector (SVX II); and finally the Intermediate Silicon Layer (ISL).

The silicon system is made up of overlapping silicon microstrip detectors, arranged in pairs called ladders, with integrated electronic readout chips and cooling channels. Except for L00, the strips are double-sided with each side containing a silicon crystal etched with $p - n$ junctions. The $p - n$ junctions are reversed biased so that when a charged particle traverses the crystal ionization occurs. The freed electrons are then captured in the junction, causing a pulse of current, which is then read out with the integrated electronics readout chips. On one side of the chip the junctions are arranged to provide position information in the azimuthal plane, while on the other side of the chip the junctions are at either 90° or 1.25° to give z position information.

The Layer00 detector is a single sided radiation hard silicon layer attached to the beampipe at a diameter of 2.2 cm, which extends ±78.4 mm from the nominal interaction region in the z direction.

The SVX II detector is a 5 layer double sided detector surrounding the L00 detector. It has an inner radius of 2.4 cm, and an outer radius of 10.7 cm. The three barrels composing the detector (see figure 2.5) extend ±45 cm in the z direction, covering approximately 2.5σ of the interaction region. The stereo side of layers 0, 1, and 3 are at 90° to the z axis, while layers 2 and 4 are at -1.2° and 1.2° respectively. The stereo nature of the detector allows reconstruction of a 3D helix for each track.

The ISL consists of three layers at radii of 20, 22, and 28 cm. The layers at 20 and 28 cm cover $1 < |\eta| < 2$, while the layer at 22 cm covers $|\eta| < 1$. Since the COT only covers $|\eta| < 1$, the two outer layers are important in extending the tracking coverage to higher η.

2.2.3.2. *Central Outer Tracker.* Completely surrounding the silicon detector, but still immersed in the 1.4 T magnetic field, the COT is an open cell drift chamber which uses a mixture of 60% argon and 40% ethane gas to produce ionized electrons when a charged particle transverses the detector. The COT consists of 8 superlayers of cells placed at radii between 40 and 132 cm from the beam pipe. Each superlayer is divided into cells by gold covered Mylar field sheets, with each cell containing 29 wires in a linear arrangement. Twenty five of the wires are 51 μm diameter gold-plated copper-beryllium wires which alternate between potential and sense wires (charged to either 2000 or 3000 V respectively), with two wires at each end acting to ground the potential. Since the COT is in a magnetic field, electrons accelerated towards the sense wires by the electrostatic force will also experience a Lorentz force. To keep the path linear and azimuthal, the cells are tilted at 37° so the force from the magnetic field is canceled by the radial component of the electric field. A schematic of 3 cells of superlayer 2 can be seen in figure 2.6, and a photograph of the COT wires in figure 2.7.

The differently ionized particles are attracted to the wires of different electric potential; where the charge is collected and subsequently read out at the end of the chamber. From the difference in time between the arriving pulses and the known drift times of the ions in the argon-ethane gas, a spacial resolution of about 180 microns is achieved. The superlayers alternate between stereo and axial configurations, with the innermost layer being stereo.

The cells in an axial superlayer run parallel to the beam pipe and provide ϕ information, while the stereo superlayers have a 2° offset from parallel which provides information on the z position.

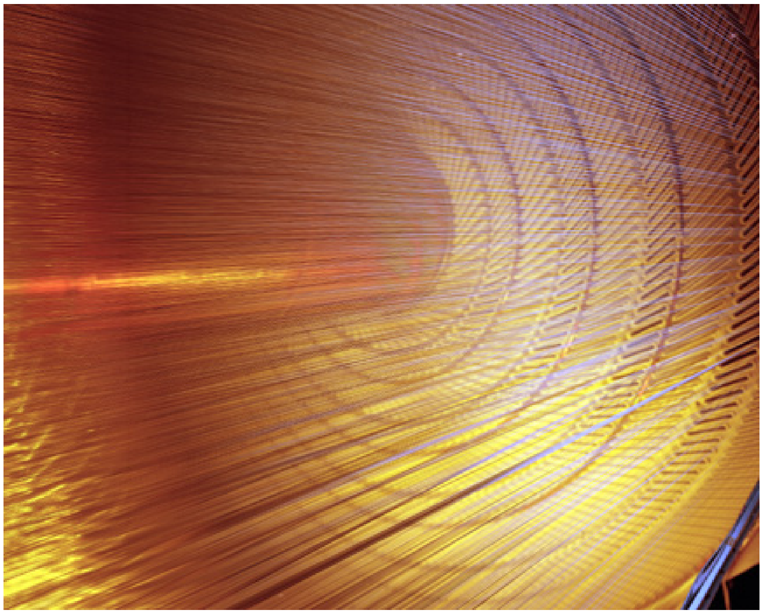

FIGURE 2.6. A picture of the COT wires.

2.2.4. Calorimeters. Surrounding the tracking chambers of the CDF detector are calorimeters which measure the energy of particles. All of the calorimeters are based upon sandwiching scintillating material between layers of dense metal plates. When an electron or photon enters the calorimeter, it interacts with the heavy metal material generating a shower of electrons, photons, and positrons. Hadrons (either neutral or electrically charged) entering the calorimeter create a shower of hadrons and photons in the dense material. The secondary particles excite the atoms of the scintillator, which then radiate photons when they transition to the ground state. The photons are collected with acrylic light guides and directed to photomultiplier tubes, whose output can be integrated to give a measure of the energy absorbed by the calorimeter. The type of showering material determines sensitivity to either electromagnetic or hadronic particles; with high-Z material ($Z \equiv$number of protons in the atomic nucleus) being better for electromagnetic particles, and high-A materials ($A \equiv$number of protons plus neutrons in the atomic nucleus) better for hadronic showers. A summary of the calorimeter's properties can be found in table 2.1.

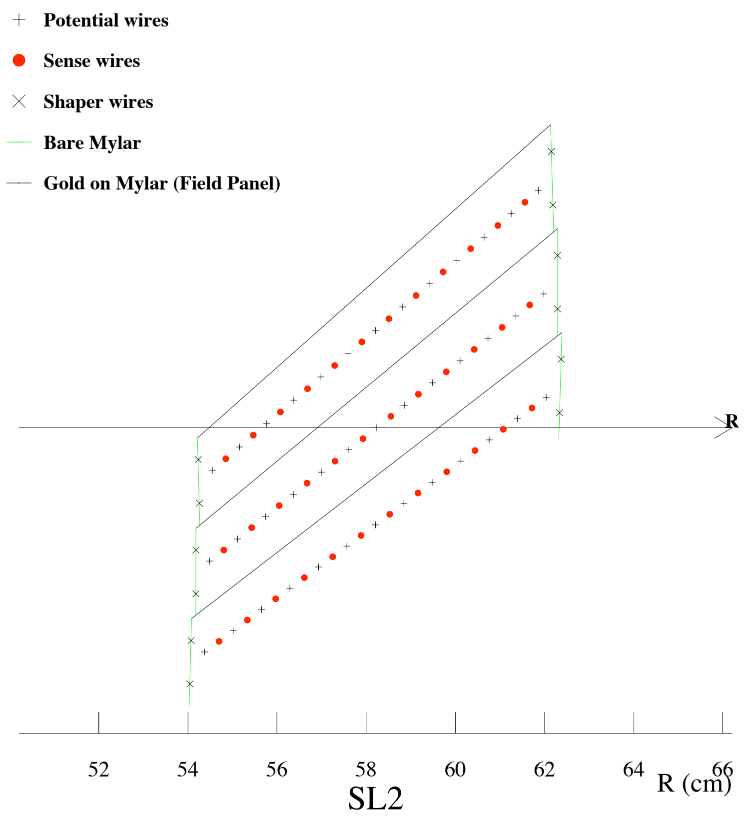

FIGURE 2.7. Three cells from superlayer 2 of the COT.

Sub Detector	CEM	CHA	WHA	PEM	PHA
η Coverage	$\|\eta\| < 1.1$	$\|\eta\| < 0.9$	$0.7 < \|\eta\| < 3.6$	$1.1 < \|\eta\| 3.6$	$1.1 < \|\eta\| 3.6$
η Segmentation	0.11	0.11	0.1	0.2	0.25
ϕ Segmentation	15°	15°	15°	30°	30°
Layers	31	32	15	23	23
Material	Lead	Steel	Steel	Lead	Iron
Radiation Length	$18\chi_0$	$4.7\lambda_0$	$4.5\lambda_0$	$21\chi_0$	$7\lambda_0$
Energy Resolution	$1.7\% \pm \frac{13.5\%}{\sqrt{E}}$	$\frac{80\%}{\sqrt{E}}$	$\frac{80\%}{\sqrt{E}}$	$1\% \pm \frac{16\%}{\sqrt{E}}$	$5\% \pm \frac{80\%}{\sqrt{E}}$

TABLE 2.1. Summary of CDF calorimeters.

2.2.4.1. *Electromagetic Calorimeter.* The electromagnetic calorimeter surrounds the superconducting solenoid, and primarily measures the energy deposited by electrons and photons. The central electromagnetic calorimeter (CEM) covers the $|\eta| < 1.1$ region, while the plug calorimeters (PEM) cover $1.3 < |\eta| < 3.6$. CDF uses *sampling calorimeters* made from alternating layers of 4.5 mm lead plate and 4.0 mm of plastic scintillator.

The CEM calorimeter contains 31 layers of lead and scintillator, giving a total radiation length of $18\chi_0$. The calorimeter is segmented into projective towers with each tower covering a space of 15° in ϕ, and 0.1 units of η, which helps to provide coarse position measurement. At the location of shower maximum ($6\chi_0$) is a Ar/CO_2 proportional strip detector, made from orthogonal strips and wires, with the wires running parallel to the beam axis. The shower maximum detector (CES) provides improved shower location information, as well as shower shape information to help aid in initial particle identification. Similarly, there is also another proportional chamber, the central preradiator, that measures the shower development of particles entering the calorimeter. A schematic representation of a wedge in ϕ, and a shower max chamber of the CEM calorimeter can be seen in figure 2.8. The energy resolution of the CEM calorimeter is $1.7\% \pm \frac{13.5\%}{\sqrt{E}}$, where E is measured in GeV.

The PEM calorimeters are located in the plug regions of either side of the detector and are constructed of towers covering 30° in ϕ and 0.2 units of η. The 23 layers of lead and scintillator provides a radiation depth of $21\chi_0$. Like the CEM calorimeter, the PEM contains a shower maximum detector (PES), which is located in the fifth sampling slot. The energy resolution of the PEM calorimeter is $1\% \pm \frac{16\%}{\sqrt{E}}$.

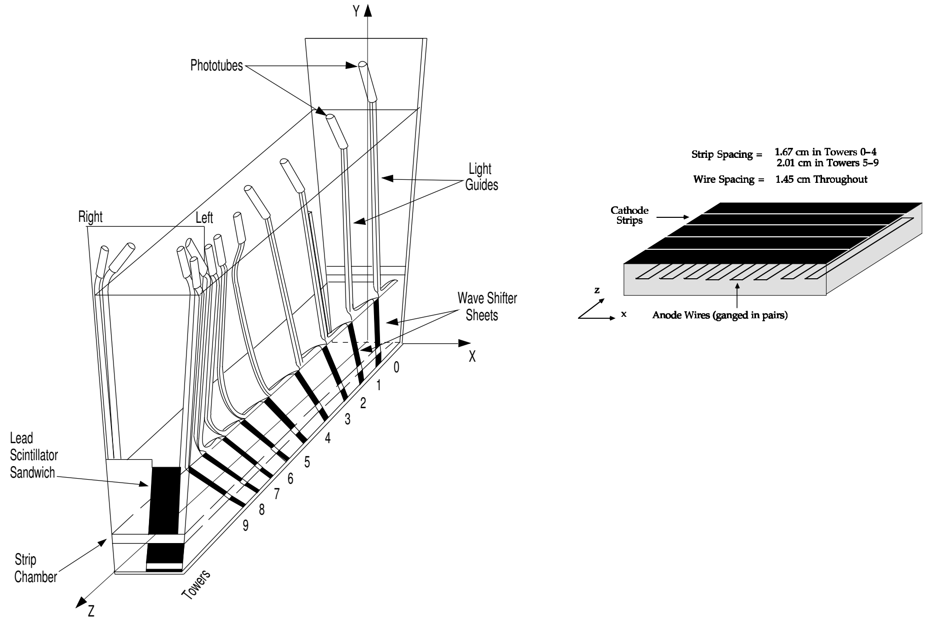

FIGURE 2.8. A schematic representation of a wedge of the central calorimeter (left), and a central shower max chamber (right).

2.2.4.2. *Hadronic Calorimeter.* The hadronic calorimeters are located outside of the elecromagnetic calorimeters and are segmented in similar ways. Outside of the CEM calorimeter is the central hadronic calorimeter (CHA), which is composed of 32 layers of 2.5 cm steel plates, and 1.0 cm scintillators covering $|\eta| < 0.9$. To help fill the gap between the CHA and the end plug, the endwall hadron calorimeter (WHA) covers $0.7 < |\eta| < 1.1$, with 15 layers of 5.0 cm steel and 1.0 cm scintillator. These two calorimeters provide about $4.5\Lambda_0$ absorption lengths with an energy resolution of $\frac{80\%}{\sqrt{E}}$. Located outside of the PEM calorimeter is the plug hadron calorimeter (PHA) which has 23 layers of 2.0 inch iron and 6.0 mm scintillator, giving an absorption length of about $7.0\Lambda_0$, giving a resolution of $5\% \pm \frac{80\%}{\sqrt{E}}$.

2.2.5. Muon Systems. Muons leave little energy in the calorimeters due to the $\frac{1}{m^2}$ suppression of the electro-magnetic bremsstrahlung [5], and being relatively long lived, they typically escape the detector. Because of this, the CDF muon detectors are located outside the other components of the detector. The muon chambers at CDF consist of 4 layers of single-wire drift chambers that detect the passing of charged particles through them, as illustrated in figure 2.9. If three layers register a hit, it is considered a muon *stub*, which then may be traced back to a track in the tracking chamber to determine momentum.

To keep cosmic ray muons from entering the analyzed data sample, scintillators are paired with the drift chambers to determine timing information so coincidence with a bunch crossing can be required.

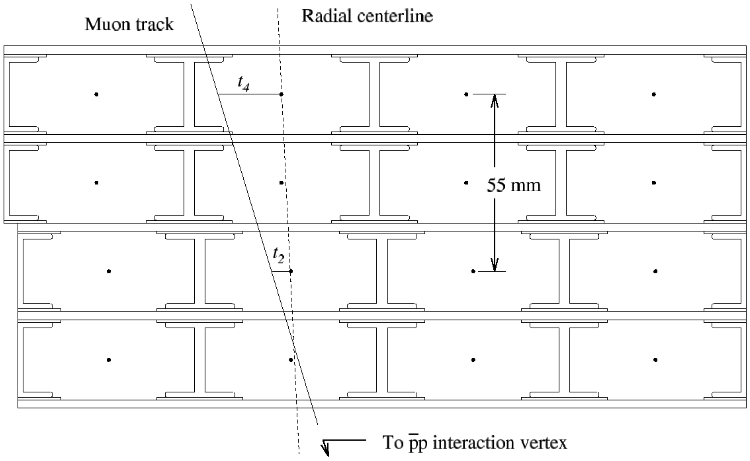

FIGURE 2.9. View of a muon chamber showing the path of a particle transversing it.

The central muon detector (CMU) is located directly outside of the CHA calorimeter and coverse $|\eta| < 0.6$. A particular weakness of the CMU detector is its relative lack of shielding, allowing some non-muon particles to make it to the detector, causing a fake muon signal. The central muon upgrade (CMP) detector is located outside of the return yoke of the solenoid magnet, which acts as a shield for non-muon particles ensuring a clean muon signal. The CMP detector may be combined with the CMU detector to provide a very pure muon identification.

The central muon extension (CMX) extends muon coverage from $0.6 < |\eta| < 1.0$, and is composed of several separate pieces to compensate for the collision hall not originally being designed to accommodate this detector. The arches are on the sides, the keystone sits on top of the detector, and the miniskirt extends underneath the detector, providing full angular coverage.

The barrel muon detector (BMU) covers the region of $1.0 < |\eta| < 1.5$, and is named because the drift chambers are attached to the large cylindrical pieces of steel at the ends of the detector designed to protect the electronics in the collision hall from radiation.

2.2.6. Trigger and Data Acquisition. With $p\bar{p}$ collisions occurring every 396 ns, it is impracticable to read out all 750k channels of information from the detector for each collision (about 20 TB/s), so CDF uses a deadtime-less online trigger system to record only the 100 most interesting events each second. To accomplish this feat, the trigger system is composed of three levels, each successively reducing the rate of passing events while increasing the granularity used to perform the decision. A flowchart of the trigger system can be seen in figure 2.10.

2.2.6.1. *Level 1.* Level 1 of the trigger system reduces the event rate from 1.7 MHz to about 50 kHz through the use of dedicated custom designed hardware and relatively crude information from the detector. A decision on whether an event will pass this level of the trigger must be made within 5 μs of a collision and is based on information of clusters of energy in the calorimeters from jets or photons the presence of electrons or muons from tracks extrapolated to calorimeter clusters or muon stubs, the sum of calorimeter energy, or an imbalance in the transverse component of calorimeter energy. The tracks are reconstructed using information from the COT using the Extremely Fast Tracker (XFT) system, to give both phi position and p_T information.

2.2.6.2. *Level 2.* Level 2 of the trigger system further reduces the event rate to approximately 700 Hz by adding additional information from the detector subcomponents.

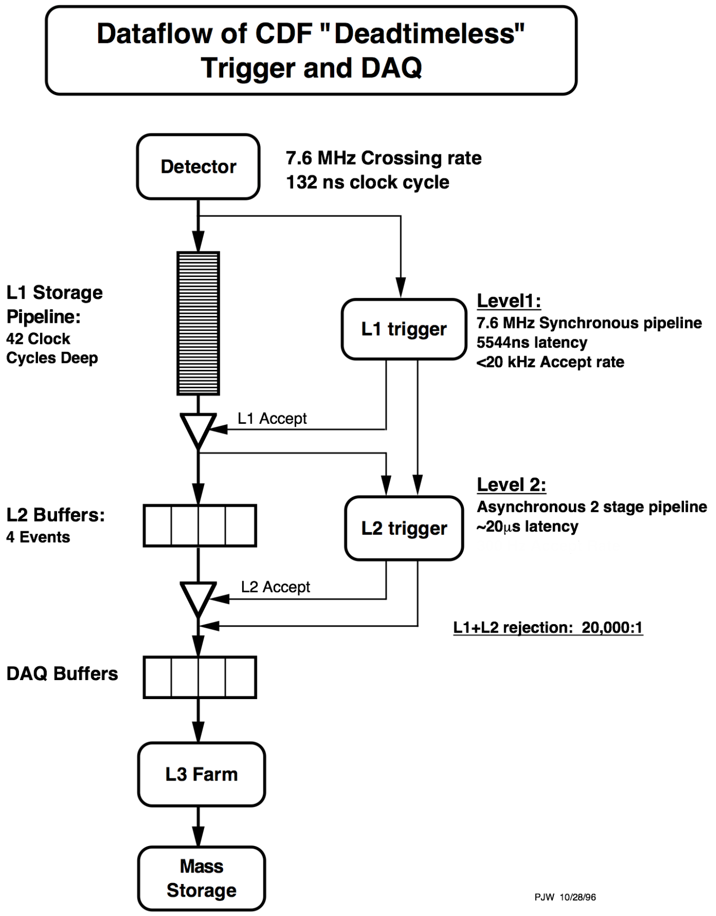

FIGURE 2.10. Schematic flowchart of the CDF trigger system.

Information from the silicon detector may be used to look at the impact parameter of tracks to look for potential b-taggs of jets. Electron and photon definitions are further refined, and clustering of calorimeters can occur to reconstruct jets. The XFT system is also able to use the stereo information of the COT to give z information of tracks. The final level 2 decision is made on a single pc computer running the linux operating system. The level 2 system is asynchronous, meaning unlike level 1, a decision does not need to be made by a given time after a collision.

2.2.6.3. *Level 3.* Level 3 of the trigger system is comprised of a computer farm of several hundred computers, where complete detector information from an event is sent to a single processor to allow full reconstruction of the event to make a decision. The acceptance rate at level 3 is about 100 Hz; with events passing this level of the trigger being temporarily written to a hard disk, then copied over to a more cost effective tape for permanent storage. Permanently recorded events are processed with offline reconstruction algorithms and calibrated for time dependent detector effects in preparation for being analyzed by physicists.

CHAPTER 3

Event Simulation And Reconstruction

In order to effectively analyze the observed data sample from the CDF experiment, two important things must happen: the electronic readouts of the detector must be translated into physically meaningful forms, and reliable simulations of the physics processes and the detector must be created in order to interpret the observed results.

To the first end, higher level detector objects must be created from the electronic readouts in order to identify both the *type* of particles in the final state, and to measure their properties such as: direction, energy, and electric charge. To the second end, just knowing which final state particles are in an event doesn't allow you to determine which physics processes gave rise to them; to determine the underlying physics processes the recorded events must be compared against simulations where the underlying physics processes are known, thus allowing at least a probabilistic determination of the underlying physics process.

3.1. Event Reconstruction

In the CDF detector, the calorimeters record the location and magnitude of energy deposited by particles, while the tracking portions of the detector only record if and when a charged particle passes through a given region. To utilize this information, two basic reconstruction techniques are used: clustering of energy deposits of adjacent cells in the calorimeters is performed, while individual hits in the tracking portions of the detector are combined into tracks. These two reconstruction techniques are then used together to form high level objects, which then are identified as candidate electrons, muons, taus, photons, hadronic jets, or individual hadrons.

3.1.1. Tracking. Tracking for CDF is performed primarily with the COT, with additional accuracy added by using information from the the silicon detector, measured beam position, and the calorimeter for forward tracks. The track finding algorithms used in this paper consist of Outside-In (OI), Inside-Out (IO), and Phoenix algorithms.

Outside-In tracking begins with hits in the axial superlayers of the COT being associated together using both position and timing information to form short track segments within each superlayer. Initially, hits in a superlayer may be shared by more than one track segment. After creation of the track segments is finished however, the segment with more total hits exclusively retains the previously shared hits. Track segments from the axial COT layers are then linked together starting with segments in the outermost superlayer and extrapolation these to the segment in the next inner axial superlayer which gives the best fit. This is repeated until the innermost layer is reached. Once the axial segments are linked together, a fit is performed to determine the track's orientation in the $r - \phi$ plane, creating a 2D track. This segment-finding algorithm is then performed for the stereo superlayers, with the resulting segments considered for linking to the 2D tracks in order to add z information. If a 2D track still doesn't have any stereo segments after stereo linking, individual stereo layer hits are then matched to the 2D track to obtain z information, providing there are enough stereo hits. The tracks are re-fit again to obtain full 3D position information, with a momentum resolution of $\sigma\left(p_T\right) = \frac{0.15\%}{p_T^2}$, where p_T is in units of GeV/c. These COT tracks can then be further improved by adding the high-resolution tracking information from the silicon detector, and additionally by using the beam spot position which is about 30 μm across. Reconstruction of the tracks in the COT using high p_T ($\geq$ 10 GeV/c) tracks from electrons is over 98% efficient [**29**, **30**, **31**].

OI tracks are generally required to have hits in at least four of the COT superlayers, however this becomes impossible for forward tracks due to the geometry of the COT. Instead, the IO track algorithm starts with tracks from the silicon detector which have hits in at least three layers. It then extends these tracks into the COT, adding COT hits not already part of other tracks.

Phoenix tracking is only used in this paper for forward, high p_T electrons, and is only performed after the event vertex has already been defined (see section 3.1.2) using other tracks from the COT. Phoenix tracking starts with an electromagnetic cluster in the forward (PEM) calorimeter. It uses the shower max detector to determine the potential track's final location, and the calorimeter's clustered energy to determine its momentum. Two roads are then constructed between this point and the event vertex; one for positively charged particles, one for negative particles, using the assumed transverse momenta of the particle to determine the trajectories. Hits in the silicon detector along these roads are then associated with the track. The momentum resolution of these tracks are highly correlated to the energy resolution of the PEM calorimeter, meaning they are not as precise as COT based tracks. The Phoenix tracking efficiency is found using $Z \rightarrow ee$ events to be 0.89 ± 0.01[32].

3.1.2. Vertexing. Although the x and y positions of the hard scattering interaction between the partons (partons refers to the valence quarks, the “sea” of virtual particles, or the gluons) in the proton and antiproton are fairly well known from the location of the beams, the z position can vary significantly. Measuring the z position of the primary interaction is a crucial measurement since the transverse and longitudinal components of measured energies rely on this position in order to be calculated. This z-position is referred to as the *primary vertex*, and is where most high p_T physics objects in the event are assumed to originate. Before finding the primary vertex of the event, all z vertexes of the event are first reconstructed using the ZVertexFinder algorithm [33]. The ZVertexFinder uses tracks that pass a set of minimum quality requirements to form a set of vertices in the z dimension, where the z location of each vertex is found using a weighted average of the tracks z_0 and its errors. Each of these vertices roughly represents the z location of either the primary interaction point or another soft interaction in the event.

To determine the primary vertex of the hard interaction, the PrimeVertexFinder [34] algorithm takes as input a set of tracks passing minimum quality requirements, and a seed vertex from ZVertexFinder. The PrimeVertexFinder algorithm first fits for a 3D vertex location, then uses this location to prune the collection of tracks associated with the vertex by removing any track contributing a χ^2 greater than 10 to the fit. Using the pruned set of tracks, a new 3D location is fit for, and the pruning is once again performed. This process is repeated until a stable location is found. Typical accuracy of the vertex position is $\sigma_z \approx 30 \mu m$, and $\sigma_{\perp, z=0 \text{ cm}} \approx 29$ μm with this increasing to $\sigma_{\perp, z=40 \text{ cm}} \approx 50$ μm for vertices not near the $z = 0$ cm position. The vertex which has the highest sum p_T of tracks associated with it becomes the primary vertex of the event. This paper only considers events where the reconstructed primary vertex is a maximum of ± 60 cm from the middle of the detector.

3.1.3. Calorimeter Clustering. Energy deposition from final state particles is typically not contained within a single calorimeter tower, thus towers must be *clustered* together to fully measure the particle's energy and position. This paper uses two different clustering techniques: one for EM objects like electrons and photons, and one for jets, the collection of particles created when a quark or gluon hadronizes.

3.1.3.1. *Electromagnetic Clustering.* After tower-to-tower corrections are applied to the CEM and PEM calorimeters, the highest E_T tower is considered as a seed tower for clustering if it has an E_T greater than 2 GeV/c^2. For the CEM detector, neighboring towers in η are added to the seed tower if they contain greater than 100 MeV of energy in total from the EM and hadronic portions of the calorimeter. This leaves 1, 2, or 3 towers in the cluster, with each of these towers being removed from the list of seed towers. In the PEM, all 8 towers bordering the seed tower are considered for addition to the cluster, with the highest E_T tower from these 8 being assigned as the seed tower's daughter. The clustering algorithm then searches possible 2x2 combinations that include the seed and the daughter, and selects the one with highest E_T for potential addition to the cluster. If the additional 2 towers have greater than 100 MeV, they are added to the cluster, most often producing clusters of 2x2 towers. For both the CEM and PEM calorimeters, the typical size of a cluster is 0.2 in η by 0.15° in ϕ. The position of the cluster is more accurately determined by clustering in the shower max detector, the centroid of which gives a position resolution of 1 mm. The energy resolution is $1.7\% + \frac{13.5\%}{\sqrt{e}}$ in the CEM and $1\% + \frac{16\%}{\sqrt{E}}$ in the PEM [35].

3.1.3.2. *Jet Clustering.* Although several jet clustering algorithms are available, this paper only uses a seeded, cone-based algorithm. Towers with greater than 1 GeV/c^2 of energy are considered seed towers, with the clustering algorithm considering seed towers in order of decreasing E_T. Towers within a cone of $\sqrt{(\eta_i - \eta_C)^2 + (\phi_i - \phi_C)^2} \leq 0.4$ are added to the seed tower, then an E_T-weighted centroid is calculated to be the geometric center of the cluster. This procedure is then repeated using the new geometric center until a stable configuration is found. The resulting cluster is then a jet, with the jet's energy being determined by both the electromagnetic and hadronic calorimeters, since hadronization creates both electromagnetically and hadronically interacting particles. Jet clusters that share more than 50% of overlapping towers are combined into a single jet, and other overlapping towers are assigned to the jet with the closer centroid. This algorithm produces jets with an energy resolution of approximately $\frac{68\%}{\sqrt{E}}$ [35].

3.1.4. Particle Identification. Upon completion of track finding and energy clustering, these entities can then be associated with particles that created them, such as electrons, muons, and hadronic jets; leaving the imbalance of transverse energy in the event to potentially be attributed to neutrinoes.

3.1.4.1. *Lepton Identification.* Electrons are identified by the presence of a track pointing to an electromagnetic calorimeter cluster, with some additional quality requirements, listed in table 3.1. CEM and PHX electrons are calibrated for both position and time dependant effects using the mass peak of $Z \rightarrow ee$ events, with CEM gaining further calibrations from using the fact $E/p = 1$ for electrons. Muons are identified by a track pointing to a stub in a muon detector, with calorimeter energy consistent with a minimum ionizing particle, as well as some further quality requirements, listed in table 3.2.

3.1.4.2. *Jets.* Jets must be corrected for a number of physical effects. In order to effectively tell the energy of the original parton (either a quark or gluon), these effects and modeling of systematic uncertainties are described below [35]:

Pseudorapidity-Dependence: The non-uniformity of the detector in η, due to differences in clustering performance between central and plug regions as well as cracks in the calorimeter, must all be accounted for. This correction is performed using dijet events, and is calculated separately for the observed data sample and Monte Carlo. This correction can be seen in Fig. 3.1. Systematic uncertainties for this correction are derived from varying the maximum allowed p_T for the third jet and the maximum missing transverse energy allowed, ranging from 1% in the central region to 7.5% for high η, low p_T jets.

Multiple-Interactions: The number of interactions in each beam crossing follows a Poisson distribution, with a mean dependent on the instantaneous luminosity. Each soft interaction causes extra energy to be deposited in the calorimeter not associated with the hard interaction. Thus the number of reconstructed vertices is used to parametrize this effect, and a minimum bias observed data sample (triggered by the CLC) is used to calculate the correction. Systematic uncertainties are

(Non-I) CEM	PHX
$E_T \geq 20$ GeV	$E_T \geq 20$ GeV
E/p ≤ 2 (unless $p_T \geq 50$ GeV/c)	
$E_{had}/E_{em} \leq 0.055 + 0.00045E$	$E_{had}/E_{em} \leq 0.05$
$L_{shr} \leq 0.2$	$\chi^2_{PEM} \leq 10$
Track $p_T \geq 10$ GeV/c	Phoenix Track
Track $\lvert z_0 \rvert \leq 60$ cm	Phoenix $\lvert z_0 \rvert \leq 60$ cm
Axial SLs with 5 hits/SL ≥ 3	Si Hits ≥ 3
Stereo SLs with 5 hits/SL ≥ 2	
Fiducial to CES	$1.2 \leq \lvert \eta_{PES\_2D} \rvert \leq 2.8$
$\lvert \Delta z_{CES} \rvert < 3$ cm	PES 5×9 U ≥ 0.65
-3 cm $\leq Q \times \Delta x_{CES} \leq 1.5$ cm	PES 5×9 U ≥ 0.65
$\chi^2_{CES} \leq 10$	$\Delta R_{PES,PEM} \leq 3$ cm
Photon Conversion Veto	
Iso($\Delta R = 0.4/E_T$) ≤ 0.1 (unless NI)	Iso($\Delta R = 0.4/E_T$) ≤ 0.1

TABLE 3.1. Electron Identification Criteria for CEM and PHX electrons used in this paper: NI denotes a non-isolated electron, SL denotes COT superlayer, L_{shr} is short for "lateral energy sharing," and quantifies the difference between the pseudorapidity distribution of the energy in the calorimeter and what is expected for an electromagnetic shower, Δx_{CES} is distance between extrapolated track on CES position in direction perpendicular to the beamline and radial vector, χ^2_{CES} and PES quantities are measures of how much the particle shower looks like an electron in the shower max detectors (as compared to test beam profiles), or for how close the shower max location matches track location.

derived from using different observed data samples (lepton triggered and inclusive jet) to calculate the correction, giving approximately a 15% uncertainty for this correction.

Absolute Jet Energy Scale: The calorimeter response must be corrected from the measured energy to the absolute energy of the parton creating the jet. This correction is performed using dijet Monte Carlo events and is parametrized via a double Gaussian in difference of jet energies, $\Delta p_T = p_T^{particle} - p_T^{jet}$, and transverse momentum of the jet. Systematic uncertainties for this correction are assessed by comparing the observed data sample and Monte Carlo EM calorimeter response for $W \to e\eta$ and $J/\Psi \to ee$ events, giving a 3.5% uncertainty, and the fact $Z \to ee$ calibration events show simulation is less accurate near the edges of calorimeter towers, a 10% effect for these events. Difference in Monte Carlo showering algorithms give an additional 1% systematic. The correction is shown in Fig. 3.2.

<table>
<tr><th>(NI) (CMUP / CMU / CMP)</th><th>(NI)CMX</th><th>CMIO</th></tr>
<tr><td colspan="3">$p_T \geq 20$ GeV/c
Axial SLs with 5 hits/SL ≥ 3
Stereo SLs with 5 hits/SL ≥ 2
Track $|z_0| \leq 60$ cm
$d_0 <$ (w/Si Hits 0.02, w/o 0.2) cm
$E_{em} < 2$ GeV+ max(0,0.0115*(p-100))
$E_{had} < 6$ GeV+ max(0,0.028*(p-100))
Iso($\Delta R = 0.4/E_T$) ≤ 0.1 (unless NI)</td></tr>
<tr><td>$|\Delta x_{CMU}| < 7$ cm (for CMUP,CMU)</td><td>$|\Delta x_{CMX}| < 6$ cm</td><td>$E_{em} + E_{had} \geq 0.1$</td></tr>
<tr><td>$|\Delta x_{CMP}| < 5$ cm (for CMUP,CMP)</td><td>$\rho_{COT} > 140$ cm</td><td>Fiducial to CES</td></tr>
<tr><td>Fiducial $x_{CMUP,CMU,CMP} < 0$ cm</td><td>Fiducial $x_{CMX} < 0$ cm</td><td>Non-fudical</td></tr>
<tr><td>Fiducial $z_{CMUP,CMU} < -3$ cm</td><td>Fiducial $z_{CMX} < -3$ cm</td><td>Non-fudical</td></tr>
<tr><td>Fiducial $z_{CMP} < 0$ cm</td><td></td><td>Non-fiducial</td></tr>
</table>

TABLE 3.2. Muon Identification Criteria for CMUP, CMU, CMP, CMX and CMIO muons used in this paper. NI denotes a non-isolated muon, SL denotes COT superlayer, Δx quantities refer to distance from the extrapolated track position, and the stub in the muon detector in the direction perpendicular to the beamline and radial vector.

Out-of-Cone and Underlying Event: The amount of energy which ends up outside of the 0.4 jet cone, as well as the *underlying event*, interaction between the remaining partons in the proton and antiproton, are not modeled perfectly in Monte Carlo; thus the observed data sample and Monte Carlo are compared to assess a correction and systematic uncertainty. For the out-of-cone uncertainty, an annulus with radius between $0.4 < \Delta R < 1.3$ around the jet in photon + jet events is compared between the observed data sample and Monte Carlo, in order to derive this p_T dependent systematic. Since higher p_T jets are narrower, they suffer less uncertainty, but low p_T jets receive up to a 4% uncertainty. The *underlying event* effects are estimated from looking at tracks in a region sensitive to radiation: 60° to 120° from the jet, and by estimating the effective differences between the observed data sample and Monte Carlo, as well as the difference between Monte Carlo showering methods. This systematic source gives up to a 10% uncertainty for low p_T jets and lower uncertainty for higher p_T jets.

Splash Out Energy: The cone of $\Delta R = 1.3$ still does not always contain the entire energy of the original parton. In Monte Carlo events, an average of 0.5 GeV of "splash-out" energy falls outside of this region, and since measuring such small amounts of energy in the observed data sample is difficult, half this value (0.25 GeV) is taken as a systematic uncertainty.

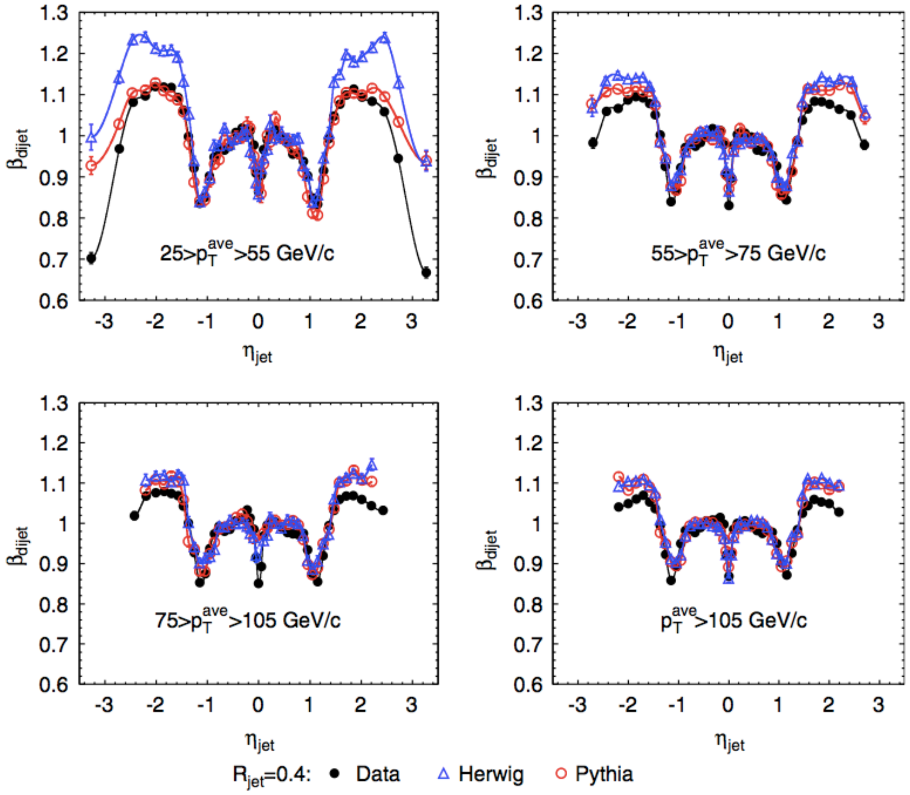

FIGURE 3.1. The η dependent corrections for jets as determined by dijet events, where $\beta_{dijet} = p_T^{probe}/p_T^{trigger}$, the probe jet corresponds to the plotted η_{jet}, and the trigger jet is in the region $0.2 <| \eta_{jet}\eta < 0.4$.

3.1.4.3. *b-jet Tagging.* An important property of jets is their ability to be *b-tagged* to signal the presence of a heavy flavor quark. For this paper, *b-tagging* becomes significant in order to greatly reduce backgrounds since signal contains b-quarks jets, while many background physics processes do not. The idea behind b-tagging is that since b-hadrons can only decay through the weak interaction (a virtual $W^{\pm}$ boson), they have a relatively long lifetime, which given their significant Lorentz boost in the lab frame, means the half-life decay time for a $|\vec{p}| \approx 65$ GeV/c b-hadron with mass 5.36 GeV/c^2 and mean life time 495 μm is $x_{1/2} \approx 0.42$ cm. This gives b-quarks resulting from top quark decays a mean distance traveled of 0.37 cm. For comparison, the beampipe radius is 1.25 cm.

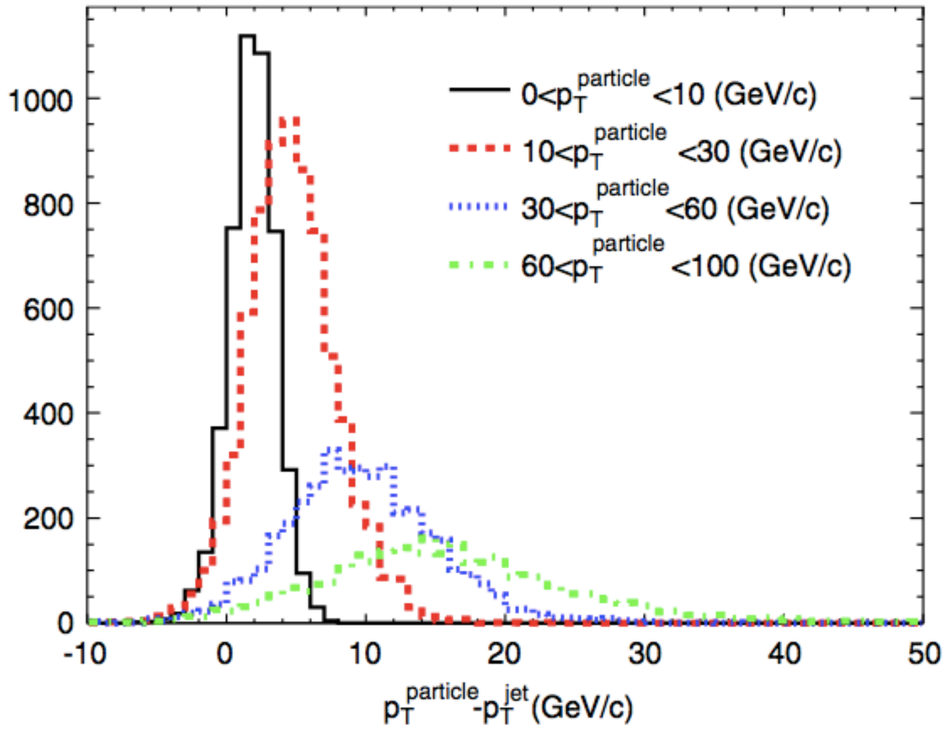

Figure 3.2. The transverse momentum difference between the measured energy and the true parton energy of the particle in dijet Monte Carlo events. Corrections for η-dependant and multiple interaction effects have already been applied. The reconstructed jet must match the originating particle with $\Delta R < 0.1$.

To take advantage of the relatively long lifetime of the mesons formed by b-quarks, this paper uses the SECVTX b-tagging algorithm which identifies jets containing heavy flavor using displaced secondary vertices. The SECVTX algorithm makes use of the high resolution tracking of the silicon detector in order to tag about 40% of high p_T b-jets as seen in Fig. 3.4, while only falsely tagging less than 1% of light flavor jets as seen in Fig. 3.6. As can be seen in Fig. 3.3, some important quantities for this algorithm are:

- L_{xy} The distance between the primary and secondary vertex.
- d_0. The impact parameter of a track; this is the distance in the $r-\phi$ plane between the track's reconstructed vertex and the beamline A large value of this quantity indicates a displaced track.
- Δz_0. The difference in z between the tracks origin, and the primary vertex. This is another indicator of a displaced track.
- d_0 significance. The impact parameter divided by its uncertainty

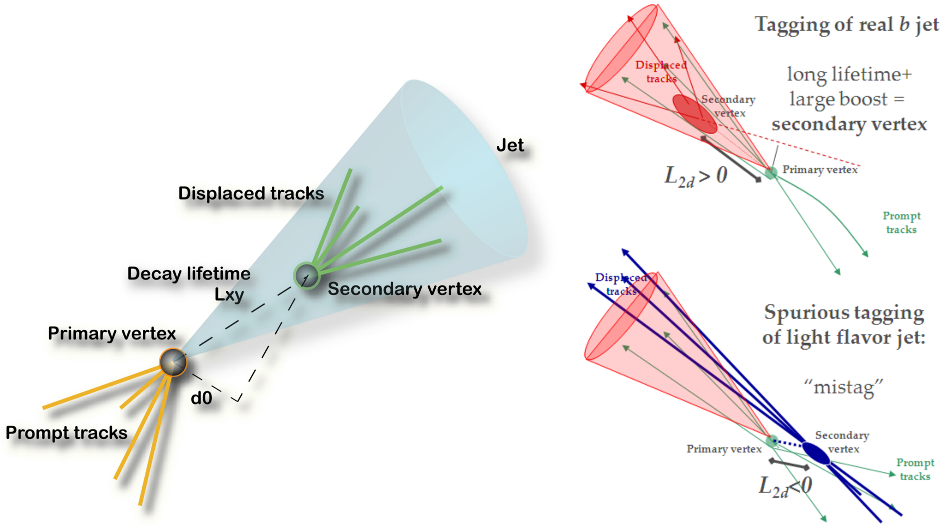

FIGURE 3.3. An illustration showing a convenient coordinate system (L_{xy}, d_0) to classify b-meson secondary vertex (SECVTX) tagging at CDF (left), and an illustration of the difference between negative L_{xy} (bottom right) and positive L_{xy} (top right) events. Events with negative L_{xy} are most likely light-flavor jets, and form the basis to determine the light-flavor contamination in positive L_{xy} events.

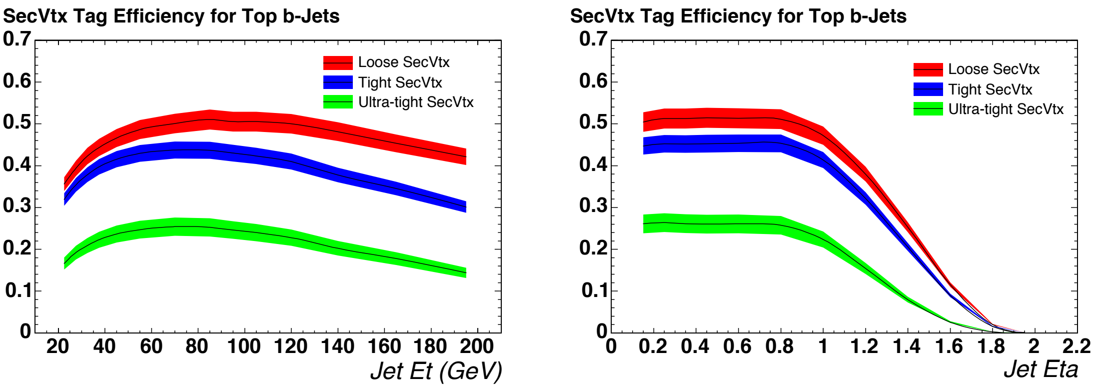

FIGURE 3.4. The efficiency of b-tagging a jet created by a bottom-quark in the decays of top-quark events, as a function of jet E_T (left), and η (right). This paper only considers Tight SecVtx tags (blue).

The SECVTX algorithm uses a 2 pass approach in an attempt to find secondary vertices. First it tries to create vertices from a higher number of potentially lower quality tracks inside the jet, then if that is unsuccessful, it attempts to find vertices with fewer tracks, which are higher quality. The details are outlined below:

(1) Create list of Pass 1 tracks by making a list of all tracks with p_T>0.5 GeV/c, and impact parameter significance $|\frac{d_0}{\sigma_{d_0}}| > 2.5$.

(2) Remove candidate K^0 tracks from the list of pass 1 tracks.

(3) Tracks are sorted based on quality and d_0 significance.

(4) Apply Pass 1 Vertex Finding:

Form seed vertices by pairing tracks starting from the higher ranked tracks.

Attach additional tracks to the seed vertices if their d_0 significance with respect to the seed vertex is smaller than 3.0.

If at least one additional track is attached to the seed vertex, then the vertex is retained and the tracks are constrained to a common vertex.

Iteratively remove tracks from vertices if their $\chi^2 > 50$, refitting vertex position between each iteration.

(5) Pass 1 vertices must then pass the following cuts:

Removal of poorly reconstructed tracks and potential material interactions from light-flavors, via an upper cut on $c\tau$.

≥ 3 tracks.

vertex decay length significance greater than 3.

(6) Pass 2 track selection: performed if no pass 1 vertices are found

Tracks must have p_T>1.0 GeV/c with impact parameter significance $|\frac{d_0}{\sigma_{d_0}}| > 3.0$.

(7) Pass 2 Vertex Finding: All tracks are constrained to a common vertex, with the tracks contributing large χ^2 removed as in Pass 1.

(8) Pass 2 vertices must pass the following cuts:

At least 2 tracks in the vertex after an upper $c\tau$ cut.

Decay length significance $|\frac{d_0}{\sigma_{d_0}}| > 3.0$.

This algorithm stops at the first vertex found. Secondary vertices with a negative L_{xy}, an unphysical secondary vertex which is in the opposite direction of the jet, are artifacts of the tracking resolution and referred to as negative tags. Negative tags form a basis to estimate how often jets with positive L_{xy} are not actually heavy flavor jets. Light flavor jets tagged with a positive L_{xy} are referred to as *mistags*.

An estimate of the number of mistagged jets (light flavor jets with positive SECVTX tags) in the event sample is given by the number of jets with negative tags multiplied by an asymmetry factor. The asymmetry factor compensates for the apparent fact that light flavor jets are more likely to obtain positive tags than negative tags. This asymmetry factor is obtained by a fit of $sign(L_{xy}) \times mass_{vrtx}$, and illustrated in Fig. 3.5. The correction ranges in value from 1.33 ± 0.11 for jets with E_T between 10 and 22 GeV/c^2, to 1.53 ± 0.06 for jets with an $E_T > 60$ GeV/c^2, and is denoted $\alpha\beta$.

The number of events after final event selection for the analysis in this paper is so few, that there will not be enough negative tags to provide a reliable estimate of mistags. Instead, the probability of a jet containing a negative tag is parametrized in 6 variables: jet E_T, number of tracks in the jet, the pseudo rapidity of the jet, number of primary vertices in the event, the sum E_T in the event, and the z position of the primary vertex of the event. The six variable parametrization of mistags is referred to as the *mistag matrix*, where each entry in the matrix is the probability that a jet with the given value of the 6 variables, will contain a negative tag, as determined using large jet triggered data samples. The mistag rate as a function of jet E_T and η can be seen in Fig. 3.6. To determine the number of mistagged jets in the final b-tag event selection, we use the following formula:

$$N_{mistag} = \sum_{events} \left[1 - \prod_{jets\,i} \left(1 - \alpha\beta p_{mistag}^{jet\,i} \right) \right]$$

where $p_{mistag}^{jet\,i}$ is the probability of the i^{th} jet in an event being mistagged, which is determined from the mistag matrix, $\alpha\beta$ is the asymmetry correction, and the sum is performed over events before any b-tagging requirements. Additionally, if the mistag matrix is applied to Monte Carlo, an additional scale factor will need to be applied to account for differences between simulation and the observed data sample; how this scale factor is derived is outlined in section 4.5.4, but is very close to 1.0.

3.1.4.4. *Missing Transverse Energy.* Since neutrinos rarely deposit energy in the detector, we must infer their presence from an imbalance of transverse momentum in the event. Since we cannot measure the transverse momentum of neutral particles directly, we nearly equivalently measure the imbalance of transverse energy of the event in order to infer the neutrinos' transverse momentum. The missing transverse energy calculation starts as the negative transverse vector sum of all calorimeter towers energy within the region $|\eta| < 3.6$ with more than 100 MeV of energy, and not included in the clustering of jets or electrons. To this quantity is added the negative transverse energy vector of each of the *corrected* jets,

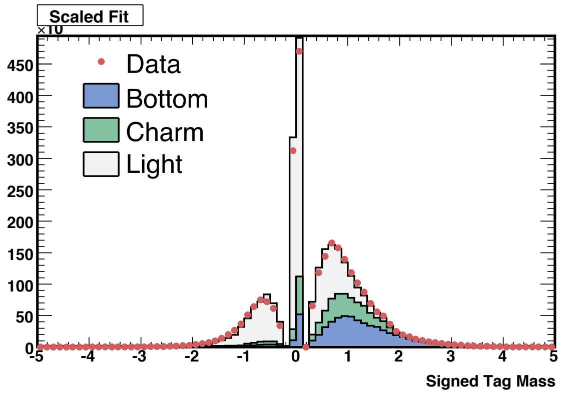

FIGURE 3.5. The signed secondary vertex mass of SECVTX tagged jets with E_T between 22 and 40 GeV/c^2. The Signed Tag Mass is defined as the sign of L_{xy} times the invariant mass of the tracks making up the secondary vertex.

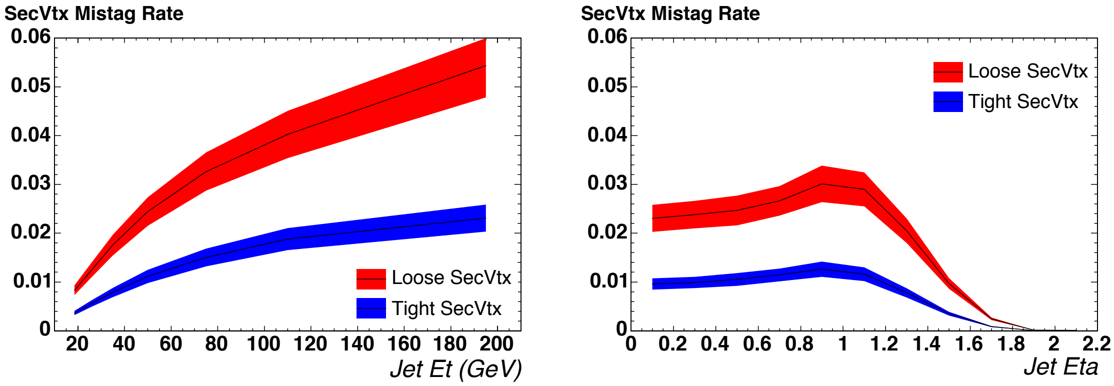

FIGURE 3.6. The rate at which a light flavor jet is *mistagged* (a false positive b-tag), as a function of jet E_T (left), and jet η (right). This paper only considers *Tight SecVtx* (shown in blue) b-tags, resulting in less than 1% of light flavor jets receiving a b-tag.

electrons, and muons, where the muons' energy is derived using the measured momentum. The scalar value of this 2D vector quantity is denoted as $\not\!\!E_T$. A particular difficulty of the missing transverse energy is that it relies upon essentially all parts of the detector, so it is subject to any mis-measurements or systematic uncertainties of the entire detector.

3.2. Monte Carlo Simulation

In order to interpret the results of the observed data sample, an accurate simulation of both the hard physics process present in the observed data sample and the interaction of the final state particles with the detector are required. This simulation is done through generation of *Monte Carlo* events (named after a city famous for its gambling). These are events that are randomly generated in order to simulate potential events in the observed data sample. The generation of these events is a multi-step process which proceeds roughly as: initial state parton generation, final state parton generation, showering, radiation, hadronization of the final state partons, and finally simulation of the detector's response to these particles.

3.2.1. Initial State Parton Generation. The partons which interact in the proton and anti-proton can carry almost all of the (anti-)proton's momentum, almost none of it, or anywhere in between, which explains why the sum of the z momentums of final state particles is typically not zero. How much momentum is carried by the initial state partons can be determined probabilistically from the *parton distribution functions* (PDFs), which are functions of the type and flavor of the parton, and Q^2 (the momentum transfer of the interaction). An example set of PDFs can be seen in Fig. 3.7. Event generation begins with picking initial state partons probabilistically according to the PDFs (or alternatively weighting events with given initial parton momentums by the PDF values). Accordingly, how the PDFs are computed will make a difference in predicted event kinematics and computed cross section. There are many different ways PDFs can be computed. A few of the differences include: to which order they are computed (e.g. leading order, next-to-leading-order, etc), α_s value and evolution used, experimental input used, schemes for handing heavy flavor quarks, etc. This paper uses PDFs produced by the Coordinated Theoretical-Experimental Project on QCD (CTEQ) originally released in 1999 and updated in 2002 [36] in order to generate the Monte Carlo simulations.

3.2.2. Event Generation. Once the initial state partons have been generated, the hard scattering process must then be simulated. Events used in this paper are based on Leading Order (LO) matrix elements (or equivalently tree-level Feynman diagrams), often times with radiation and other effects accounted for in the hadronization state. All Monte Carlo events used for this paper are "unweighted," meaning each event has a weight of 1, such that a large amount of simulated events will give the expected kinematics according to the differential cross section. To state this differently, events are generated according to the

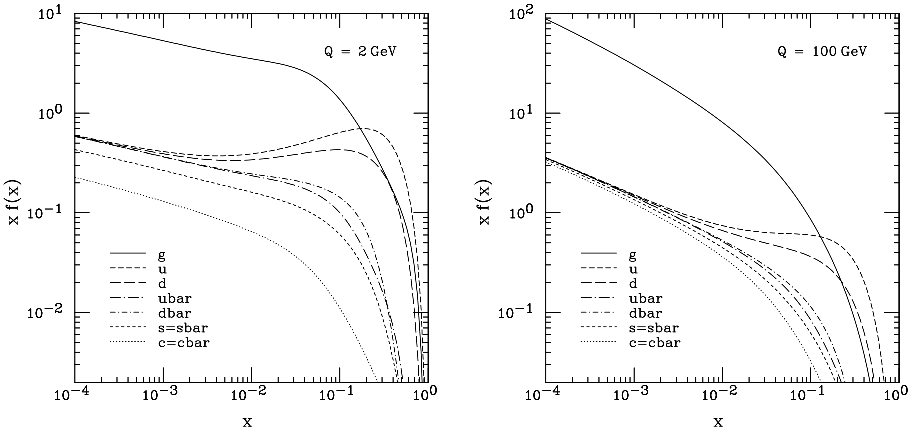

FIGURE 3.7. The CTEQ6M next-to-leading-order PDF parametrization for protons as a function of momentum fraction, x, at momentum transfer, Q, of 2 GeV (left) and 100 GeV (right) [37].

probability that an event would have a given final parton state [38]. Below, the different Monte Carlo event generators are explained in further detail.

3.2.2.1. *PYTHIA.* The PYTHIA [39] program is used to generate events as well as perform showering and hadronization of the final state particles. It uses simple Feynman diagrams and often makes significant simplifications, such as ignoring spin correlations and color effects, as well as using parton shower approximations to account for the effects of initial and final state radiation (e.g. extra jets in the event). For many processes it does not use the full first order matrix element to generate the event. For instance, $t\bar{t}$ events are modeled as a $2 \rightarrow 2$ process with the top masses being smeared by a Breit-Wigner, while the top quarks are decayed ignoring their polarizations, with a similar process being repeated for the $W^{\pm}$ bosons. However, often polarization or color effects can be safely ignored, or external routines can be called to compensate, and in these cases PYTHIA performs quite well. For this paper $t\bar{t}$, diboson, and signal processes are simulated using the PYTHIA v6.216 event generator.

3.2.2.2. *ALPGEN.* Electroweak bosons, specifically $W^{\pm}$ and Z/γ^{*}, can radiate potentially large amounts of gluons, and thus are harder to model using PYTHIA's radiation approximations. Instead, in these instances ALPGEN [40] is used to simulate the hard interaction, since it calculates the matrix elements that include gluon radiation. The difficulty of this approach can be seen by the fact that the number of Feynman diagrams grows as the factorial of the number of radiations. It is also of note that ALPGEN preserves color information for the showering algorithm. The use of the proper matrix elements, which implicitly include spin correlations, and does not neglect color effects, is believed to produce more realistic modeling for these processes which include large amounts of radiation. The down side of ALPGEN is that it does not model the Breit-Wigner mass peaks of the top quark or $W^{\pm}$ bosons. Events generated with ALPGEN are passed to PYTHIA v6.325 for showering. The ALPGEN v2.13 event generator is used to model Z/γ^{*} plus jets, and where Monte Carlo is used for $W^{\pm}$ plus jets, it is used too.

3.2.3. Parton Showering. Parton showering consists of adding initial- and final-state radiation as well as effects from beam remnants and multiple scatterings to a given matrix element, and is always performed by PYTHIA in this paper, regardless of event generator used. The method used to simulate initial- and final-state radiation is generally a close approximation when along the directions of the mother partons, but wide-angle emission between two jets suffers due to interference terms becoming more important. The radiation consists of emissions of gluons from the mother partons (either the initial- or final-state partons) which will split into pairs of daughter particles, with initial state radiation starting from small Q^2 and increasing as the hard scatter approaches, while final state radiation starts at larger Q^2 and decreases away from the hard scattering. It is of note that the exact mechanism for creating the radiation is somewhat arbitrary, with even what is labeled initial- and final-state radiation being arbitrary from the experimental point of view. The radiation mechanisms are tuned to match experimental data samples.

The showering generation is based on randomly choosing which particles will split into pairs of daughter particles, based on the probability of them doing so. This process is repeated with the products until all particles reach a predefined energy threshold. This approximation scheme for generation of additional jets in the event is useful since it generates an arbitrary number of jets, without having to recalculate the matrix element, which would be impractical for large multiplicities. The downside to this scheme is that it lacks color flow information as well as effects from interference terms [39]. For most electroweak processes this approximation works well given that they typically only have one gluon in the lowest order radiation diagrams. For processes with many gluons however, a more proper treatment from ALPGEN is desired.

3.2.4. Hadronization. Hadronization describes the process of colored partons being transformed into colorless hadrons. Due to QCD perturbation theory breaking down at long distances (or equivalently low energies), this phenomenon is not understood from first principles, but rather modeled phenomenologically. PYTHIA uses a relativistic massless string model, which can be thought of as a string of color between a quark (q) and antiquark ($\bar{q}$). As the q and $\bar{q}$ travel away from each other, the energy stored by this color string increases at approximately 1 GeV/fm, and once enough energy is stored in this string, it may break into a new $q'\bar{q}'$ pair, leaving two color singlet systems, $q\bar{q}'$ and $q'\bar{q}$. Typically $q'\bar{q}'$ are light quarks, with the production of flavor being approximately $u : d : s : c \approx 1 : 1 : 0.3 : 10^{-11}$, meaning charm and heavier quarks are not produced through soft fragmentation, but only in pertabative parton-showing of $g \to q\bar{q}$.

Since most particles resulting from hadronization are unstable, PYTHIA decays them according to experimental branching ratios and lifetimes, ignoring spin information. Since spin effects for tau leptons and b-mesons are important, external packages are used for these decays. Tau lepton decays are performed by the TAUOLA [41] package, which incorporates the spin information, resonances of intermediate particles, and the final-state neutrinos. The QQ [42] package developed at the CLEO experiments is used to properly decay b-meson.

3.2.5. Detector Simulation. Once the hard process, underlying event, multiple interaction, parton showering, hadronization, and unstable particle decays have been performed, it is necessary to simulate how the detector will respond to the resulting long lived particles. CDF uses a full simulation, which not only includes all subcomponents of the detector, but resolution effects, inherent inefficiencies, and consequences of passive materials such as electronics, cables, and support structures. This simulation results in a data structure identical to that of actual observed data sample, which allows the use of the exact same reconstruction algorithms for simulations as well as the observed data sample.

To model the tracking volume of the detector, CDF uses the GEANT [43] program. GEANT uses a mathematical model of the detector in combination with charge deposition models to model charge deposition by both the primary particle, as well as the showering to secondary and higher order particles. Due to the computationally intensive nature of

GEANT, it is only used to model the response of the tracking portions of the detector (silicon and COT).

Once a particle (and its potentially many showered particles) produces its first inelastic collision in the calorimeter, the CDF simulation switches to a response parametrized using test beam data samples. The program GFLASH [44] provides this parametrized response, which is both rapid and accurate, thus completing the detector simulation.

3.2.6. Additional Simulation Corrections. Although the simulation of the physics and detector response at CDF is quite impressive, due to the intricacies of the identification variables for leptons, complexity of b-tagging, and requirements to trigger the recording of events, there remain some additional corrections to simulation which must be done at the analysis level.

3.2.6.1. *Lepton Scale Factors.* The probability of electrons and muons to pass the lepton identification requirements listed in tables 3.1 and 3.2, is found to be slightly higher in Monte Carlo than in the observed data sample. To account for this, flat scale factors are used, meaning Monte Carlo events receive additional weights (see section 4.4 for Monte Carlo weighting) dependent on the types of leptons identified in it. The efficiency to reconstruct a lepton in the observed data sample is lower than in Monte Carlo, so these scale factors are less than 1, and have the effect of reducing the *predicted* number of events in the real data sample.

The identification scale factor is determined by the ratio of identification efficiencies in the observed data sample verses Monte Carlo. The identification efficiency is essentially the number of fully identified leptons (the “tight” leptons) divided by the number of very loose candidate leptons (“probe” leptons), with backgrounds for both types of leptons being corrected for. These efficiencies are determined using $Z \to \ell\ell$ events in an invariant mass range near that of the pole mass of the Z boson, where there is very little (and easily corrected for) backgrounds. The events must contain at least one lepton which can be a CEM electron or either a CMUP or CMX muon, which must pass the trigger requirements and all the identification requirements in table 3.1 or 3.2. This is referred to as the “trigger” lepton. The probe lepton is a candidate electron or muon object (a valid track with $p_T > 20$ GeV/c, fiducial to either the relevant muon detector or EM calorimeter, depending on scale factor desired) which is not the trigger lepton. Probe leptons form a superset of the tight leptons. The probe and trigger leptons must form an invariant mass near that of the Z boson pole mass, and both must be candidate electrons, or both must be candidate muons.

The lepton scale factor depends on the lepton type (CEM, PHX, CMP, CMU, CMUP, CMIO), whether or not lepton isolation is required, and the date data are recorded, and varies between 0.9 and 0.98. It is found that the increased rate of identification in Monte Carlo does not significantly affect or depend on kinematics of the event, thus making it valid to apply the flat scale factor to Monte Carlo events. This scale factor is denoted ρ_{lep}^{ID} in this paper.

3.2.6.2. *Lepton Fake Rates.* Athough the identification requirements of leptons remove the vast majority of jets from being identified as leptons, the QCD production cross section is enormous compared to the physics processes containing real leptons. Consequently some QCD jets get reconstructed as leptons. The detector simulation cannot reasonably be expected to reproduce this effect however, given the extreme dependency on the exact details of the detector and interactions of this process. Therefore, jets being reconstructed as, or rather *faking*, leptons are modeled using the observed data sample. In the *dilepton* analysis channel, the majority of events with fake leptons are W+Jet events, where not only is the real lepton from the $W^{\pm}$ reconstructed, but also one of the jets is reconstructed as a lepton as well, which is called a *fake* lepton.

To model fake leptons, a *fakeable* lepton is defined for each lepton category, with the requirements listed in tables 3.3 and 3.4, which essentially consist of requiring the fakeable lepton to fail at least one of a specific set of the lepton identification requirements. Additionally, fakeable muons must not correspond to a reconstructed electromagnetic object (photon or very loosely identified electron), and also must be fiducial to the CES, in order to avoid electrons which are mis-measured due to non-fiduciality. *Fake-rates* are then determined for each lepton type, as a function of the lepton p_T. Fake-rates give the relative probability with which a jet would be identified as a lepton. For instance, a fake rate of 0.2 says that for every 5 jets which are identified as *fakeable* leptons, there will be 1 jet which will be fully identified as a lepton. Fake rates are determined using a large jet triggered data sample, where real lepton contamination is negligible. Fake rates are simply the number of fully identified leptons in the observed jet triggered data sample, divided by the number of fakeable leptons in this same data sample, in a given p_T range. Fake rates are then defined by:

$$f_i = N_{lep,i}/N_{fakeable,i}$$

and computed per each i-th lepton p_T bin: $[20-30]$, $[30-40]$, $[40-60]$, $[60-100]$, $[100-200]$, and ≥ 200 GeV/c. In calculation of fake rates, only one fakeable is allowed per event, photon conversions and cosmic muons are removed, and events must have a $\not{E}_T$<25 GeV (to supress W+Jet events). The nominal fake rates are derived from a jet sample where the trigger requires an event to have a jet with raw $E_T > 50$ GeV.

In order to evaluate and model the fake lepton background in the dilepton channel, the observed data events with one fully reconstructed lepton, and at least one fakeable lepton are used, where the fakeable leptons are then treated in an identical manner as if there were a reconstructed lepton. If the fakeable lepton corresponds to a reconstructed jet, that jet is removed from the analysis. If an event with a fakeable lepton passes the kinematic event selection, that event then enters the analysis as part of the fake lepton background, with a weight equal to that fake lepton's fake rate. The invariant mass of leptons in a highly fake-lepton enriched region of parameter space is shown in Fig. 3.8, where it can be seen that fakeable objects form a good description of both the rate and kinematics of events where a jet fakes a lepton.

In the rare case of an event having more than one fakeable lepton, the event will enter the fake background once for each fake lepton, with each fakeable lepton being used with its respective fake rate probability in turn. Also, due to the fact that lepton identification is not 100% efficient, a fraction of non-identified real leptons can still satisfy fakeable selection criteria, however this is suppressed by $(1 - \epsilon_{lep,ID})$, and is much smaller than the assigned fake rate systematic (see section 6.6), so it is ignored.

3.2.6.3. *b-quark Tagging Scale Factors.* The complexity of the b-tagging algorithm (section 3.1.4.3) and extreme dependence on the exact details of the tracking detector means that the b-tagging algorithm does not function exactly the same in the observed data sample and Monte Carlo. It is found that Monte Carlo over-estimates tagging efficiency by about 5%, with apparently no jet kinematic dependence, and with no effect on event kinematics. This overestimation of b-tagging efficiency can be compensated for with a flat scale factor,

Fakeable (NI)CEM	Fakeable PHX
$E_T \geq 20$ GeV	$E_T \geq 20$ GeV
Photon Conversion Veto	Match to Phoenix Track
Iso$(\Delta R = 0.4/E_T) \leq 0.1$ (unless NI)	Iso$(\Delta R = 0.4/E_T) \leq 0.1$
$E_{had}/E_{em} \leq 0.125$	$E_{had}/E_{em} \leq 0.125$
+ at least one anti-cut:	
$E_{had}/E_{em} \geq 0.055 + 0.00045E$	$E_{had}/E_{em} \geq 0.05$
$\chi^2_{CES} \geq 10$	
$L_{shr} \geq 0.2$	$\chi^2_{PEM} \geq 10$
$\|\Delta z_{CES}\| \geq 3$ cm	PES 5×9 U ≤ 0.65
-3 cm $\geq Q \times \Delta x_{CES}$, $Q \times \Delta x_{CES} \geq 1.5$ cm	PES 5×9 U ≤ 0.65

TABLE 3.3. Fakeable electron selection criteria. See table 3.1 for variable definitions.

similar to the lepton identification scale factors (section 3.2.6.1). The b-tag scale factor is determined through two similar methods: one using electrons, and one muons.

(NI) (CMUP / CMU / CMP)	(NI)CMX	CMIO
$p_T \geq 20$ GeV$/c$		
Ax SLs with 5 hits/SL ≥ 3		
St SLs with 5 hits/SL ≥ 2		
Track $\|z_0\| \leq 60$ cm		
$d_0 <$ (w/Si Hits 0.02, w/o 0.2) cm		
Iso$(\Delta R = 0.4/E_T) \leq 0.1$ (unless NI)		
$E/p < 1$		
No match to CDF Em Object		
Fiducial to CES		
Fiducial $x_{CMUP,CMU,CMP} < 0$ cm	Fiducial $x_{CMX} < 0$ cm	Non-Fiducial
Fiducial $z_{CMUP,CMU} < -3$ cm	Fiducial $z_{CMX} < -3$ cm	Non-Fiducial
Fiducial $z_{CMP} < 0$ cm		Non-fiducial
+ at least one anti-cut:		
$E_{em} > 2$ GeV+ max(0,0.0115*(p-100))		
$E_{had} > 6$ GeV+ max(0,0.028*(p-100))		
No Stub	No Stub	
$\|\Delta x_{CMU}\| > 7$ cm (for CMUP,CMU)	$\|\Delta x_{CMX}\| > 6$ cm	$E_{em} + E_{had} \leq 0.1$
$\|\Delta x_{CMP}\| > 5$ cm (for CMUP,CMP)		

TABLE 3.4. Fakeable muon selection criteria. Fakeable muons must also not correspond to an electromagnetic object (photon or very loosely identified electron), and also must be fiducial to the CES. See table 3.2 for variable definitions.

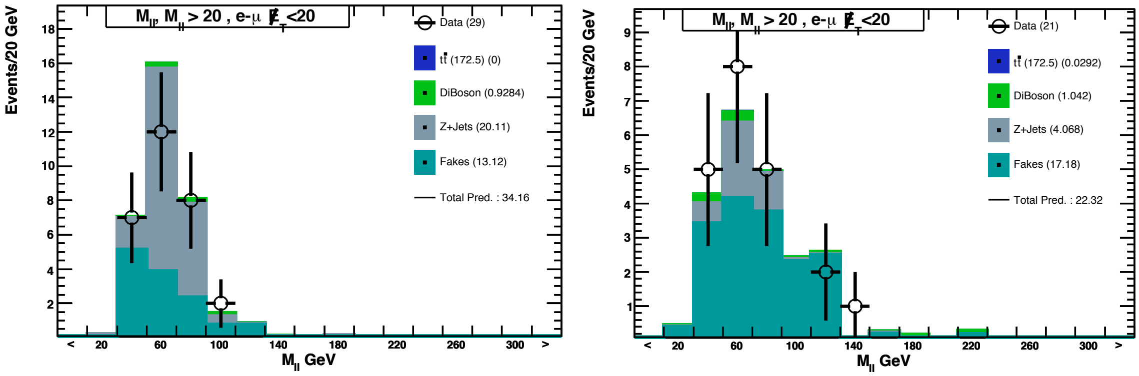

FIGURE 3.8. The invariant mass of same-sign electron-muon events with $\not{E}_T <$ 20 GeV, in the 0-jet (left) and 1-jet (right) bins. This is a region of phase space which is highly enriched in events where a QCD jet fakes a lepton. As can be seen, the fakeable lepton modeling of this background accurately predicts both the rate and kinematics. The Z+Jets events are primarily $Z/\gamma^* \rightarrow \tau\bar{\tau}$ events.

The electron method uses events with two jets having more than 15 GeV of transverse energy, with one of them, the *away* jet, being tagged by the SECVTX algorithm, and the other one, the *electron* jet, containing an electron with at least 9 GeV/c of transverse momentum. Given that the away jet is tagged and b-jets usually come in pairs, the electron in the electron jet most likely comes from a semi-leptonic decay of a b-quark. The fraction of the electron jets which are b-tagged, after being corrected for mistags, is the efficiency of the SECVTX algorithm. The mistag of the electron jet is compensated for mistagged light quarks by extrapolating electron conversions from light flavor mistagged jets to the electron jets. The muon method is similar to the electron method, but requires an 8 GeV/c muon inside the *muon* jet. The rate of mistagged jets is determined via a fit to the transverse momentum of the muon, using templates derived from Monte Carlo. Once this is done, the b-tagging efficiency can be evaluated.

Each method independently provides tagging efficiencies in the observed data sample for b-tagging, which when divided by the Monte Carlo b-tagging efficiency, gives the b-tagging scale factor. Both methods give consistent results, and are combined to give an overall scale factor of 0.95 ± 0.04. This same scale factor is also used for the tagging rate of charm quarks, but since Monte Carlo and the observed data sample charm events cannot be compared as easily, the uncertainty is doubled for these events.

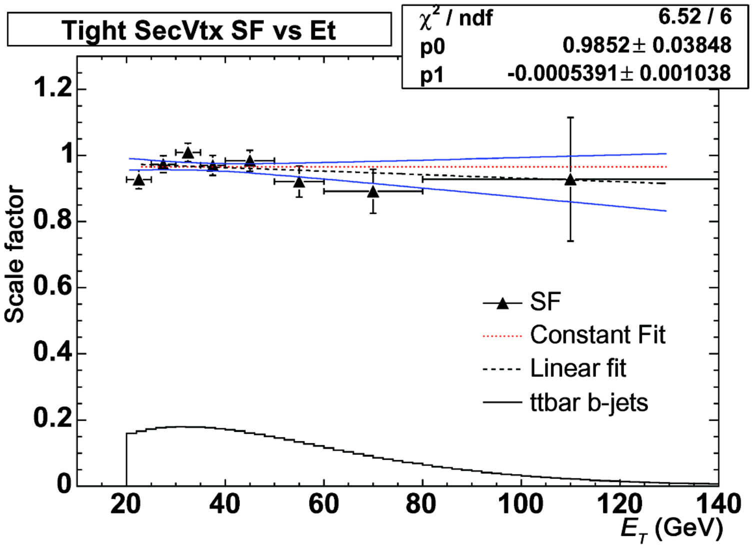

FIGURE 3.9. The SECVTX b-tag scale factor between the observed data sample and Monte Carlo, as a function of jet E_T. The scale factor is consistent with a straight line.

3.2.6.4. *Triggering.* In this paper, the triggering system is not simulated at all, meaning the inefficiencies of triggering on events must be measured, then propagated to the Monte Carlo events. As discussed in section 2.2.6, CDF uses a three stage triggering system which has inherent inefficiencies. This paper uses three different triggers, ELECTRON_CENTRAL_18 for CEM electrons, MUON_CMUP18, for CMUP muons, and MUON_CMX18_DPS, with the trigger requirements listed in tables 3.5, 3.6, 3.7 respectively. Rather than simulating triggers, which would have to take into account deadtimes, inefficiencies, instantaneous luminosities, etc, the trigger efficiency is measured in the observed data sample and applied to the Monte Carlo events in the form of a weight. The ELECTRON_CENTRAL_18 trigger efficiency is measured using events recorded from a different trigger, which requires a CEM electron and large $\not\!\!E_T$ (to form a relatively pure sample of $W^\pm$ bosons). The efficiency of the trigger is then just the fraction of these events which also fires the ELECTRON_CENTRAL_18 trigger. The efficiency averages $96.5 \pm 0.4\%$. The CMUP and CMX trigger efficiencies are determined using $Z \to \mu\mu$ events near the Z pole mass, where one of the muons in the event must have fired the trigger, and the other muon is used to determine the trigger efficiency, which is $91.6 \pm 0.5\%$ and $95.7 \pm 0.6\%$ for CMUP and CMX triggers respectively. The triggering efficiency for (NI)CMU, (NI)CMP, PHX, and CMIO leptons is assigned to be identically zero. For a portion of the observed data sample used, the CMX trigger was *prescaled* (not all events firing the trigger were kept), in order to keep the data rate at a level which could be recorded to disk. This is accounted for not by efficiency, but by the effective luminosity for this trigger. The trigger efficiency is denoted $\epsilon^{lep}_{trigger}$ in this paper, where *lep* denotes which trigger the efficiency is for.

Trigger Level	**Variable**	**Requirement**
Level 1	E_T	> 8 GeV
	E_{had}/E_{EM}	< 0.125
	p_T	> 8.34 GeV/c
	$N_{COT\ hits}$	≥ 4
Level 2	E_T	18 GeV
	$\|\eta\|$	< 1.317
Level 3	L_{shr}	< 0.4
	$\|\Delta Z\|$	< 2.0 cm
	E_{had}/E_{EM}	< 0.125
	p_T	> 9 GeV/c

Table 3.5. Trigger requirements for the ELECTRON_CENTRAL_18 trigger, at each of the three levels of the CDF trigger system. Level 1 E_T refers a single calorimeter tower, while for level 2 its the tower from level 1 combined with other nearby towers. L_{shr} is short for "lateral energy sharing," and quantifies the difference the pseudorapidity distribution of the energy in the calorimeter and what is expected for an electromagnetic shower. $|\Delta Z|$ is the difference in z between the extrapolated track and calorimeter cluster. p_T refers to the track, $|\eta|$ to the pseudorapidity of the EM cluster.

Trigger Level	**Variable**	**Requirement**
Level 1	$p_{T,CMU}$	> 6 GeV
	CMU	At least one stub
	p_T	> 4.09 GeV/c
Level 2	E	Minimum ionizing energy
	p_T	> 14.77 GeV/c
Level 3	$\|\Delta x_{CMU}\|$	< 10 cm
	$\|\Delta x_{CMP}\|$	< 20 cm
	p_T	> 18 GeV/c

Table 3.6. Trigger requirements for the MUON_CMUP18, at each of the three levels of the CDF trigger system. $p_{T,CMU}$ is the transverse moment of the stub in the CMU, E is the total energy in the calorimeter along extrapolated track path, p_T is the transverse momentum of the track, $|\Delta x|$ is the distance between the muon stub and extrapolated track perpendicular to both the beamline and the radial vector.

Trigger Level	**Variable**	**Requirement**
Level 1	$p_{T,CMX}$	> 6 GeV
	CXS	Pass timing requirment
	p_T	> 4.09 GeV/c
	$N_{COT\ hits}$	≥ 4
Level 2	p_T	> 14.77 GeV/c
Level 3	$\lvert\Delta x_{CMX}\rvert$	< 10 cm
	p_T	> 18 GeV/c

Table 3.7. Trigger requirements for the MUON_CMX18_DPS, at each of the three levels of the CDF trigger system. $p_{T,CMX}$ is the transverse moment of the stub in the CMX, p_T is the transverse momentum of the track, $|\Delta x_{CMX}|$ is the distance between the muon stub and extrapolated track perpendicular to both the beamline and the radial vector. For a portion of data taking a jet with raw E_T >10 GeV was additionally required in order to keep trigger rates low at high luminosities.

CHAPTER 4

Event Signature Overview

In the first part of this chapter a recap of the theoretical reasoning, as well as the experimental motivations for searching for the supersymetric partner of the stop quark in the chosen final state is provided. Next a justification and explanation of the slightly a-typical analysis method of the search is provided. This is then followed by a description of the experimental manifestation of signal and the Standard Model backgrounds; as well as a description of how they are estimated for a given set of event selection cuts, and how the backgrounds may be reduced relative to the signal.

4.1. Analysis Method Motivation

This search for the supersymetric partner of the top quark takes place under assumptions stated in section 1.3.3, which can be summarized as:

(1) $\tilde{\chi}_1^0$ is the LSP, and $\tilde{q}, \tilde{\ell}, \tilde{\nu}$ are heavy
(2) $m_{\tilde{t}_1} \lesssim m_t$
(3) $m_{\tilde{\chi}_1^\pm} < m_{\tilde{t}_1} - m_b$

resulting in the stop quarks decaying to the same final states as $t\bar{t}$ events, with the addition of two massive undetected neutralinos, giving three distinct final states:

- **Lepton + Jets:** $\tilde{t}_1\bar{\tilde{t}}_1 \to \tilde{\chi}_1^+\tilde{\chi}_1^- b\bar{b} \to \tilde{\chi}_1^0\tilde{\chi}_1^0 \ell\nu q\bar{q} b\bar{b}$

  One lepton with four jets and large missing transverse energy. Two jets are from the b-quarks, and 2 from the $\tilde{\chi}_1^\pm$ decay products. The missing transverse energy is from the neutrino, and two neutralinos.

- **Dilepton:** $\tilde{t}_1\bar{\tilde{t}}_1 \to \tilde{\chi}_1^+\tilde{\chi}_1^- b\bar{b} \to \tilde{\chi}_1^0\tilde{\chi}_1^0 \ell\bar{\ell}\nu\bar{\nu} b\bar{b}$

  Two opposite-charged leptons, two b-jets, and large missing transverse energy from the two neutrinos and two neutralinos. This decay is schematically represented in Fig. 4.2.

- **All Hadronic:** $\tilde{t}_1\bar{\tilde{t}}_1 \to \tilde{\chi}_1^+\tilde{\chi}_1^- b\bar{b} \to \tilde{\chi}_1^0\tilde{\chi}_1^0 q\bar{q}q'\bar{q}' b\bar{b}$

> Six jets with missing transverse energy from the 2 neutralinos. Two jets are from the b-quarks, and the four other jets from $\tilde{\chi}_1^{\pm}$ decay products.

If $M_{\tilde{\chi}_1^{\pm}} - M_{\tilde{\chi}_1^0} > M_{W^{\pm}}$, then the $\tilde{\chi}_1^{\pm}$ will decay as $\tilde{\chi}_1^{\pm} \to W^{\pm}\tilde{\chi}_1^0$, meaning the $W^{\pm}$ bosons will determine the branching ratio to each of the final states; causing the branching ratios of stop events to be the same as for top events. However, if $M_{\tilde{\chi}_1^{\pm}} - M_{\tilde{\chi}_1^0} < M_{W^{\pm}}$, then, among others, the following decays (depicted in Fig. 4.1) will open up:

$$\tilde{\chi}_1^{\pm} \to \tilde{\chi}_1^0 + W^{\pm(*)} \to \tilde{\chi}_1^0 + \ell + \nu \tag{4.1}$$

$$\tilde{\chi}_1^{\pm} \to \tilde{\chi}_1^0 + H^{\pm *} \to \tilde{\chi}_1^0 + \ell + \nu \tag{4.2}$$

$$\tilde{\chi}_1^{\pm} \to \ell + \tilde{\nu}_{\ell} \to \tilde{\chi}_1^0 + \ell + \nu \tag{4.3}$$

$$\tilde{\chi}_1^{\pm} \to \nu + \tilde{\ell}_L \to \tilde{\chi}_1^0 + \ell + \nu \tag{4.4}$$

$$\tilde{\chi}_1^{\pm} \to \tilde{\chi}_1^0 + G^{\pm *} \to \tilde{\chi}_1^0 + \ell + \nu \tag{4.5}$$

increasing the branching ratio of $\tilde{\chi}_1^{\pm} \to \ell\nu\tilde{\chi}_1^0$, and hence the dilepton final state.

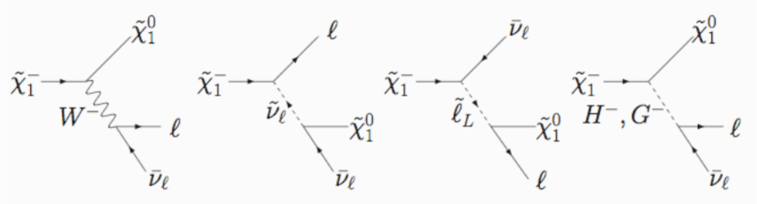

FIGURE 4.1. Schematics of possible decays of the chargino through off-shell particles when $M_{\tilde{\chi}_1^{\pm}} - M_{\tilde{\chi}_1^0} < M_{W^{\pm}}$.

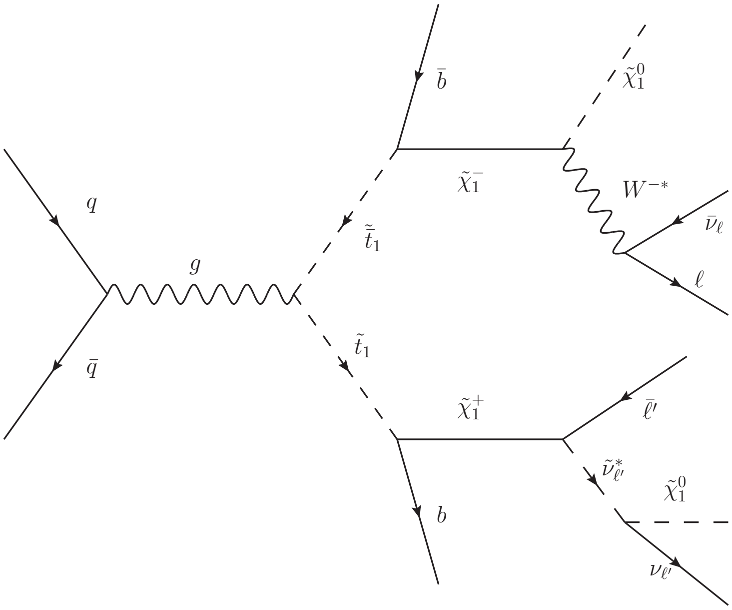

FIGURE 4.2. Schematic of a possible decay scenario leading to the dilepton final state of a $\tilde{t}_1\bar{\tilde{t}}_1$ event, when $M_{\tilde{\chi}_1^{\pm}} - M_{\tilde{\chi}_1^0} < M_{W^{\pm}}$.

Therefore this paper searches in the dilepton final state, which can have branching ratios from 0.11 to 1.0, depending on the $\tilde{t}_1$ and $\tilde{\chi}_1^{\pm}$ masses as well as the other SUSY parameters. The general event topology of signal therefore consists of two b-jets which may, or may not get b-tagged, two opposite sign leptons, and potentially large missing transverse energy. This channel has the advantage of relatively low and well controlled non-top backgrounds, as compared to the L+J and all hadronic channels; as well as the potentially enhanced branching ratio.

4.2. Experimental Motivation to Search for $\tilde{t}_1\bar{\tilde{t}}_1$

Although the search for $\tilde{t}_1\bar{\tilde{t}}_1$ is well motivated for theoretical reasons as described in sections 4.1 and 1.3.3, there was also strong experimental reasons to search for $\tilde{t}_1\bar{\tilde{t}}_1$ events with the chosen decay chain. Had nature allowed the possibility of stop quarks consistent with the listed assumptions 1 through 3, then $\tilde{t}_1\bar{\tilde{t}}_1$ events could enter the top quark event sample, mimicking the top event signatures, thus affecting top properties measurements. With respect to this, one of the most important measurements of the Tevatron is the top quark mass; so it is interesting to see how an admixture of stop would behave under top event reconstruction, and thus how it would effect the top mass measurement. In the dilepton channel where both tops decay semi-leptonically, the final decay products from stops involve an extra neutralino on each side. Since both quarks already have one invisible particle, the neutrino, in the final state, one could expect an extra missing particle on each side would not significantly disturb the top dilepton event reconstruction, and only result in a slightly lower mass due to the neutralinos carrying mass away. However in the case of the lepton + jets decays, an extra invisible particle appears also for the hadronicaly decaying quark. This should violate all of the invariant mass constraints used in top event reconstruction, thus making the stop event be poorly reconstructed under the top hypothesis.

In order to study this, simulated stop events were reconstructed under the top quark hypothesis. For the dilepton channel the neutrino weighting technique pioneered in Run I [45] of the Tevatron was used to reconstruct the top mass; while in the L+J channel the χ^2-mass fitter [46] was used. The result of this exercise for the stop mass of 155 GeV is presented in Fig. 4.4. The top dilepton channel is the cleanest with respect to signal/background ratio, and therefore it would be sufficient to compare the stop and top reconstructed mass distributions. One can see on the left figure that the mass peak for stop events is still reconstructed, although lower than the generated mass due to extra missing particles. While in case of the lepton + jets (the right figure), the stop events are reconstructed poorly and are indistinguishable from the large W + jets background.

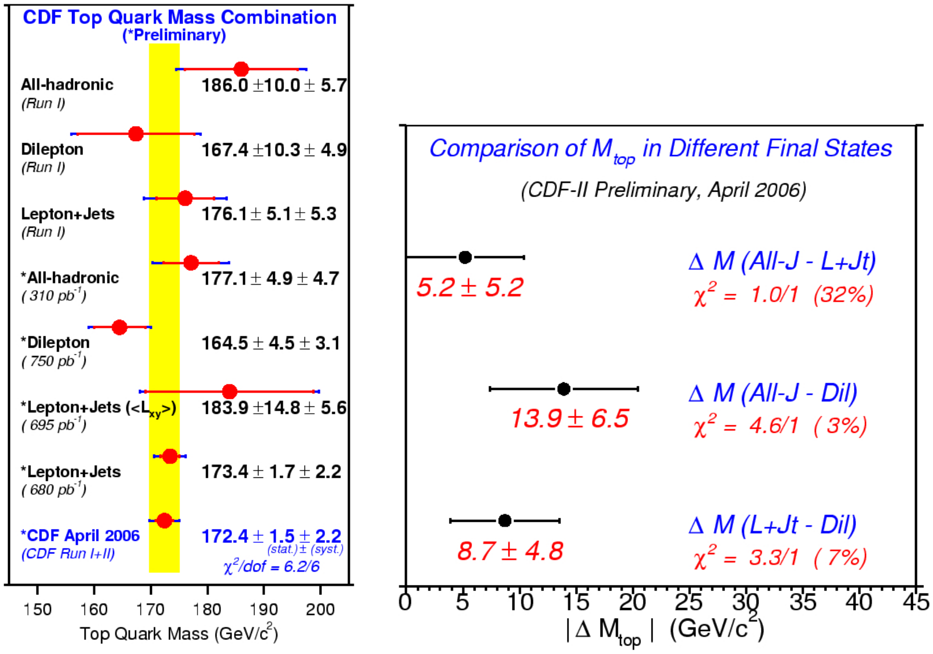

FIGURE 4.3. Summary of top mass measurements from April 2006, near when this analysis was started. More information can be found in [47].

Further, in Fig. 4.5 it can be seen from the results of top mass measurements in simulated data, that one can conclude if the top quark sample has an admixture of stop events, the measured top mass in the dilepton channel would be biased towards a lower value; while the measurement in the lepton + jets channel would not be affected, since the presence of $\tilde{t}_1\bar{\tilde{t}}_1$ would easily be hidden under the W+Jets background uncertainty. This measurment discrepancy is exactly the tendency that was present in the CDF and D0 measurements in the dilepton and lepton + jets channels in the Run I and early Run II observed data sample. In fact, the measurements in the dilepton channel verses the combined top quark mass which is dominated by the lepton + jets and all hadronic measurements (which are both unaffected by stop) were only consistent at the 3% level [47], as can be seen in Fig. 4.3. This observation served as a motivation for the current analysis. Although recent measurements in the dilepton channel are more consistent with those in the lepton + jets channel, such as the measurements used in [48], which should be noted also use a looser dilepton event selection.

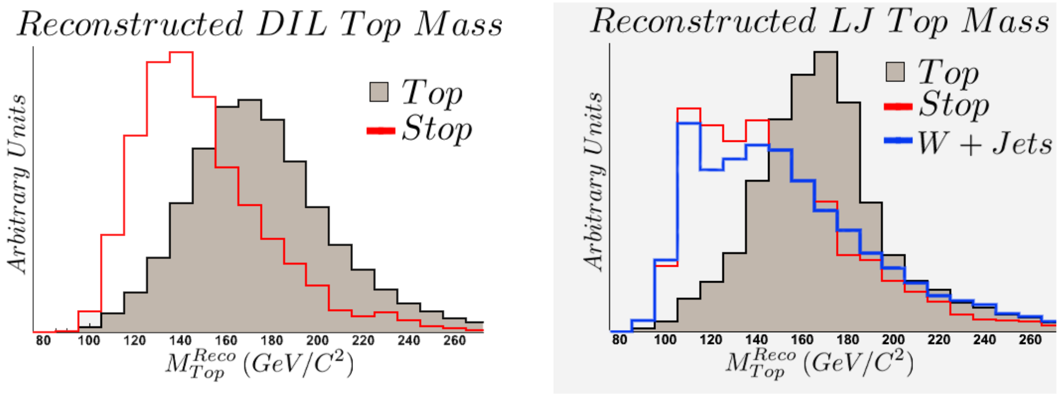

FIGURE 4.4. Results of the top mass fitter ran over signal events in the dilepton channel (left) and lepton + jets channel (right). Filled histogram is $t\bar{t}$, red histogram is stop and blue histogram is W + jets, the major background for $t\bar{t}$ in lepton + jets channel. For stop, SUSY masses of $m(\tilde{t}_1) =$ 155 GeV/c^2, $m(\tilde{\chi}_1^{\pm}) =$ 105.8 GeV/c^2, and $m(\tilde{\chi}_1^0) =$ 58.8 GeV/c^2 are used.

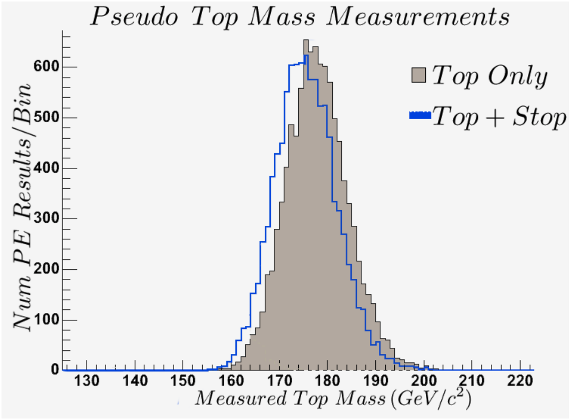

FIGURE 4.5. Results of top mass measurements containing only Standard Model (grey histogram) and an admixture of Standard Model plus $\tilde{t}_1\bar{\tilde{t}}_1$ events (blue hisogram). It can be seen if the observed data sample contains an admixture of$\tilde{t}_1\bar{\tilde{t}}_1$events in the $t\bar{t}$ sample, the measured top quark mass in the dilepton channel would likely be measured lower than the true top quark mass, unlike in the L+J channel. For stop, SUSY masses of $m(\tilde{t}_1) =$ 155 GeV/c^2, $m(\tilde{\chi}_1^{\pm}) =$ 105.8 GeV/c^2, and $m(\tilde{\chi}_1^0) =$ 58.8 GeV/c^2 are used.

4.3. Summary of Search Method

Even with the stated advantages of the dilepton final state, there are still many menacing challenges such as: $\tilde{t}_1\bar{\tilde{t}}_1$ has a production cross section approximately ${}^1\!/_{10}{}^{\mathrm{th}}$ that of its dominant background, $t\bar{t}$ (at similar masses); the $\tilde{t}_1\bar{\tilde{t}}_1$ and $t\bar{t}$ theoretical cross sections are poorly known; and due to the amount of energy carried away by the neutralinos, $\tilde{t}_1\bar{\tilde{t}}_1$ events are subject to high amounts of systematic uncertainties from things like the jet energy scale. Because of this, this analysis was developed in a slightly non-conventional manner.

Typically in high energy physics analyses, the choosing of event selection cuts is one of the first steps of the analysis; and is typically done based on an intermediate figure of merit such as $s/\sqrt{b}$, under consideration of signal and the major backgrounds. Then more refined estimates of backgrounds are performed, followed by the evaluation of the systematic uncertainties. One or two of the event selection cuts may then be refined based on the dominant systematic uncertainties or background. The expected and observed limits can then determined.

However for this $\tilde{t}_1\bar{\tilde{t}}_1$ search a different approach was needed to overcome the low production cross section, high systematic uncertainties, and nearly identical final state event signature to the much more abundant Standard Model background $t\bar{t}$. Instead of making this analysis impractical to set meaningful limits [25], these challenges made a great opportunity to create an original and interesting analysis. To help discriminate $\tilde{t}_1\bar{\tilde{t}}_1$ events from $t\bar{t}$ events, a reconstruction of the event was performed under the stop quark hypothesis, with the resulting reconstructed stop mass of signal obtaining a more resonant peak than $t\bar{t}$ events. To make up for the low production cross section and large systematic uncertainties, event selection was saved for nearly the last step of the analysis. The event selection cuts were chosen with the aid of a genetic algorithm (Chapter 9) to maximize expected sensitivity to exclusion. This algorithm took into account all backgrounds and systematic uncertainties, and allowed non-b-tagged events to have different event selection cuts than b-tagged events. The author could not find any reference to any analysis which optimized event selection cuts to maximize expected sensitivity, taking into account all the systematic uncertainties, previously in Run II of the Tevatron.

4.4. Event Yield Estimations from Monte Carlo

In order to make a prediction of event yields we *expect* to see in the observed data sample, or to create a distribution of a kinematic quantity (ex. histogram of the E_T of a jet, invariant mass of leptons, etc.) from Monte Carlo simulations we must to take into account many things: production cross section, event kinematic acceptances, Monte Carlo scale factors, and process dependent miss-modelings. The number of expected events in the observed data sample from a given process can be found using Monte Carlo simulation by:

$$N_{exp} = L \times \sigma \times \epsilon^{MC}_{\text{selection}} \times \rho^{MC}_{SF} \times \rho^{MC}_{miss} \tag{4.6}$$

- L indicates the integrated luminosity (section 2.2.2) of observed data sample.
- σ is the production cross section of the process of interest and is typically either at next-to-leading-order or measured in the observed data sample.
- $\epsilon^{MC}_{\text{selection}}$ is the fraction of events fiducial to the detector and that pass the given event selection cuts in the Monte Carlo simulations.
- ρ^{MC}_{SF} is the various corrections to the Monte Carlo, such as lepton identification scale factors, trigger efficiencies, b-tag scale factors, as well as other various corrections.
- ρ^{MC}_{miss} is a process, and potentially event, dependent scale factor to account for known limitations of the theoretical modeling of the process.

The quantities $\epsilon^{MC}_{\text{selection}}$ and ρ^{MC}_{SF} are explained below, while ρ^{MC}_{miss} is only non unity for Z+Jets in this analysis, and is explained in section 4.5.4.

Similarly, when creating a kinematic distribution from Monte Carlo, the quantity of interest from each event passing the event selection cuts is placed in a histogram with the weight:

$$w = L \times \sigma \times \rho^{MC}_{SF} \times \rho^{MC}_{miss} / N^{MC}_{gen} \tag{4.7}$$

Where N^{MC}_{gen} is the total number Monte Carlo events simulated. In this way the *area* of the resulting histogram will be equal to N_{exp} from equation 4.6.

4.4.1. Selection Efficiency. Determining the selection efficiency for a given process is the reason all of the computation and simulation described in chapter 3 is necessary. For this analysis, only un-weighted Monte Carlo is used, meaning $\epsilon^{MC}_{\text{selection}}$ is determined by the number of the Monte Carlo events in the sample which both successfully get reconstructed and that pass the desired event selection cuts (jet E_T's, lepton p_T's, $\not\!\!E_T$, number of jets, etc.), divided by the total number of events generated in the Monte Carlo sample.

However, there are a few further complications to finding the selection efficiency. Often times the leading order matrix element used by the Monte Carlo generator is divergent for some range of phase space, typically for either extremely high pseudo rapidity, or low p_T. This doesn't necessarily cause problems since we are unable to probe extremely high η or very low p_T, so we can safely remove the possibility of generating events in these ranges of phase space that we can never detect. This does however change the selection efficiency for the process; meaning we must compensate by using a cross section in equations 4.6 and 4.7, which is computed for the same phase space as is used to generate the Monte Carlo events. It is important to use event selection cuts which make it so this limiting of phase space at generator level doesn't change the number of events making it into the analysis. Another slight detail is that the number of interactions taking place further than ±60 cm from the $z = 0$ cm position in the detector of simulation does not match the observed data sample. Therefore only Monte Carlo events generated within this ±60 cm range are allowed to pass event selection cuts, or be counted towards the number of events generated. Making this vertex requirement at generator level is compensated for as part of the vertex finding efficiency scale factor, ρ_{vrtx}, which is incorporated into ρ^{MC}_{SF}.

4.4.2. Monte Carlo Scale Factors. There are actually many separately computed scale factors which go into ρ^{MC}_{SF}; for this analysis:

$$\rho^{MC}_{SF} = \rho^{ID}_{lep} \times \epsilon_{trigger} \times \rho_{b-tagg} \times \rho_{vrtx} \tag{4.8}$$

with each of these described below:

ρ^{ID}_{lep} : ρ^{ID}_{lep} is simply the product of each of the leptons in the events scale factor described in section 3.2.6.1: e.g. $\rho^{ID}_{lep} = \rho^{ID}_{lep\,1}\rho^{ID}_{lep\,2}$

$\epsilon_{trigger}$: Since potentially either of the leptons in the event may trigger the recording of the event, $\epsilon_{trigger} = \epsilon^{lep\,1}_{trigger} + (1 - \epsilon^{lep\,1}_{trigger})\epsilon^{lep\,2}_{trigger}$. Where $\epsilon^{lep}_{trigger}$ is the trigger efficiency of the given lepton type, and is described in section 3.2.6.4. This formula assumes the probability of each lepton firing the trigger is independent of the other lepton.

ρ_{b-tagg} : This is closer to a b-tag probability. This factor is unity if no b-tagging requirements are placed on the event (the so called pretag event selection). Otherwise the b-tag probability of each jet in the event must be found. As explained in section 3.2.6.3, if a jet is tagged in Monte Carlo, the probability a similar jet in the observed data sample would be tagged is 95%, therefore the probability of that jet being taggged is assigned to be 95% if it is a c- or b-jet at truth level. If a truth level c- or b-jet in Monte Carlo is not b-tagged, the probability of that jet being tagged is assigned to be 0%. Light flavor jets in Monte Carlo are not considered for b-tagging via the SECVTX algorithm, but instead a b-tagg probability is assigned using the mistag matrix, as described in section 3.1.4.3. The b-tag probability for light flavor jets is assigned to be the mistag matrix probability multiplied by a Monte Carlo correction scale factor, described in section 4.5.4.

Once each jet in an event is assigned a probability of being b-tagged, the event b-tag, ρ_{b-tagg}, is then:

$$\rho_{b-tagg} = 1 - \prod_{j} (1 - p_j) \tag{4.9}$$

where p_j is the probability of the j^{th} jet being b-tagged. For the anti-b-tagged channel one would use one minus this value.

ρ_{vrtx} : The z-vertex scale factor

4.5. Signal and Background Event Signatures

This section describes rough qualitative features of the signal and background, as well as special techniques used to estimate these backgrounds above and beyond what was described in the previous section.

4.5.1. Signal Event Signature.

From Fig. 4.2 it can be seen basic event selection for this analysis will include requiring two oppositely charged leptons, two jets, and missing transverse energy ($\not\!\!E_T$). Changing the thresholds for energy or momentum required for these objects, as well as the requirements of these objects relations to each other (both

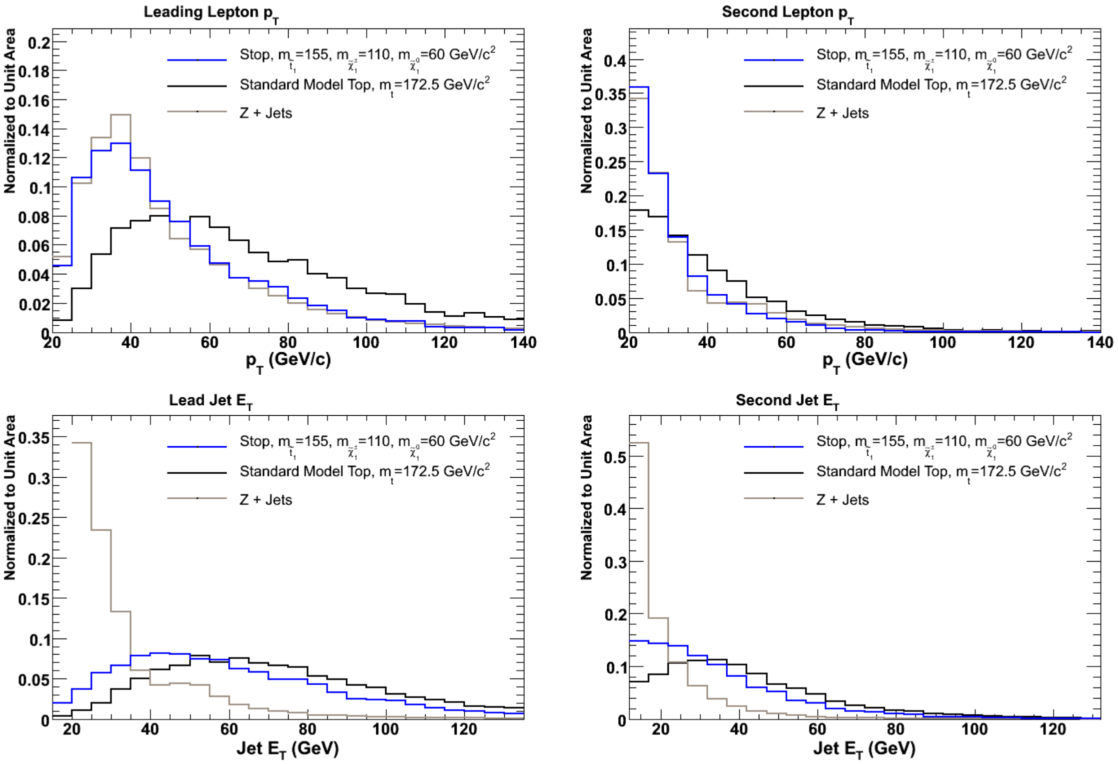

FIGURE 4.6. Lepton p_T and jet E_T distributions for an example $\tilde{t}_1\bar{\tilde{t}}_1$ mass scenario of $m(\tilde{t}_1)$ = 155 GeV/c^2, $m(\tilde{\chi}_1^{\pm})$ = 110 GeV/c^2, and $m(\tilde{\chi}_1^0)$ = 60 GeV/c^2, compared against similar distributions for Standard Model $t\bar{t}$ events and Z + Jets events. Top left is the p_T of the lead lepton in events, top right is the p_T of the second lepton in the event, bottom left is the E_T of the lead jet, and bottom right is the second jet E_T.

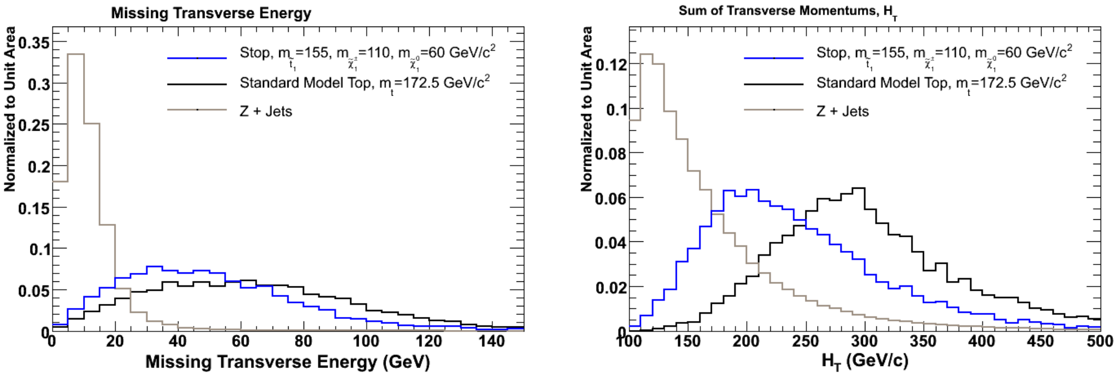

FIGURE 4.7. Missing transverse energy (left), and the scalar sum of transverse momentums, H_T, for an example $\tilde{t}_1\bar{\tilde{t}}_1$ mass scenario of $m(\tilde{t}_1)$ = 155 GeV/c^2, $m(\tilde{\chi}_1^{\pm})$ = 110 GeV/c^2, and $m(\tilde{\chi}_1^0)$ = 60 GeV/c^2, compared against similar distributions for Standard Model $t\bar{t}$ events and Z + Jets events.

are referred to as event selection cuts), will affect the relative amount of signal verses background that will enter the analysis. Additionally, the event selection cuts can also be dependent on things like if the event has a b-tag, or the types of leptons in the event, since the backgrounds also depend on these quantities. Some kinematic distributions of these quantities for an example SUSY mass scenario is compared against Standard Model sources in Figures 4.6 and 4.7. The types of cuts which are target at reducing specific backgrounds are described along with the relevant background description below.

Signal is estimated using the techniques described in section 4.4, with only a minor modification: since jets faking leptons is modeled using fake-leptons (section 3.2.6.2), it is required for both the stop and anti-stop quarks to decay semi-leptonically at truth level. For reference, for a SUSY mass scenario of $m(\tilde{t}_1) = 132.5$ GeV/c^2, $m(\tilde{\chi}_1^{\pm}) = 105.8$ GeV/c^2, and $m(\tilde{\chi}_1^0) = 47.6$ GeV/c^2, at a dilepton branching ration of 0.11, using the final event selection cuts (see Chapter 9), 3.9±0.9 stop events are expected in the tagged channel, and 9.5±1.9 in the non-b-tagged channel.

4.5.1.1. *Signal Monte Carlo Modeling.* For the stop signal simulation, several combinations of SUSY mass scenarios were generated with the PYTHIA generator, and are listed in table 4.1. As the input to the MC generator the stop mass, U(1), and SU(2) gaugino parameters (M_1 and M_2 respectively) are specified. The values M_1 and M_2 are approximately equal to neutralino ($\tilde{\chi}_1^0$) and chargino ($\tilde{\chi}_1^+$) masses. Also the stop mixing angle is set to unity, and $\tan\beta$ to 5.0. Note that the actual values of these last two parameters are irrelevant, since they define mixing between light and heavy stop quarks, while the cross section of pair produced stop quarks does not depend on the mixing, but on the actual value of the stop mass only. Similarly, the actual relationships between $m_{\tilde{\chi}_1^+}$ and M_2, and between $m_{\tilde{\chi}_1^0}$ and M_1 are irrelevant, since masses of the supersymmetric particles will determine the acceptance and kinematics of the stop events.

Since the discriminant between Standard Model and stop events is the reconstructed stop mass, a test was performed to ensure changing the generation parameters did not effect this quantity. This test implicitly verifies that the mass of the virtual particle that the $\tilde{\chi}_1^{\pm}$ decays through doesn't affect the reconstructed stop mass. The results of this test can be seen in figure 4.8, and helps show this analysis is not directly affected by these parameters.

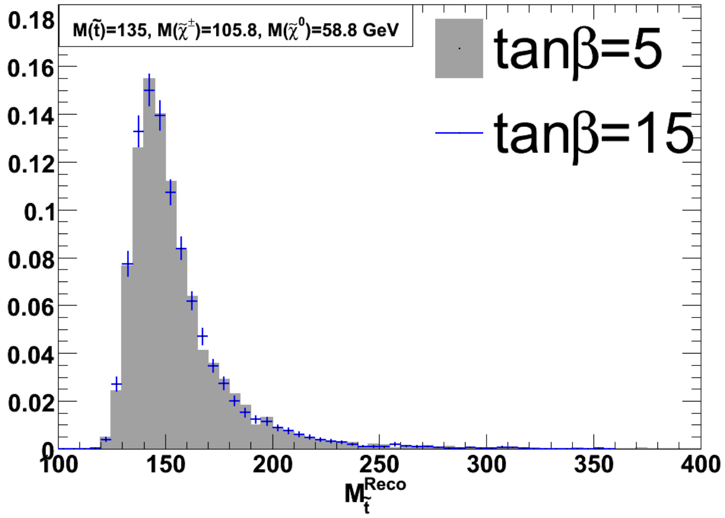

FIGURE 4.8. A comparison of the reconstructed stop mass for Monte Carlo generated signal events of $\tan\beta = 5.0$ and $\tan\beta = 15.0$, for $m(\tilde{t}_1) = 135$ GeV/c^2, $m(\tilde{\chi}_1^{\pm}) = 105.8$ GeV/c^2, and $m(\tilde{\chi}_1^0) = 58.8$ GeV/c^2. Since $M_{\tilde{\chi}_1^{\pm}} - M_{\tilde{\chi}_1^0} < M_{W^{\pm}}$.

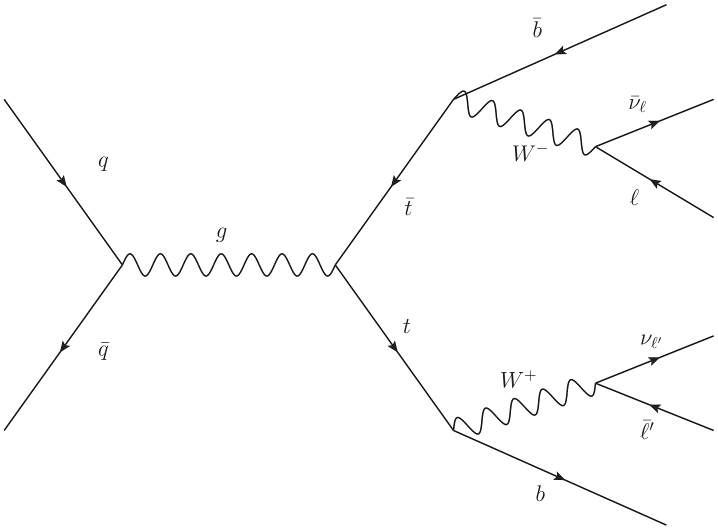

FIGURE 4.9. Schematic representation of the production and decay of a $t\bar{t}$ event at the Tevatron. ℓ and ℓ' can be either e, μ, or τ; for the τ case it must be reconstructed as an e or μ.

4.5.2. Top Event Signatures. The dominant background for this search is $t\bar{t}$ production, and is modeled using inclusive PYTHIA event simulation as described in section 3.2.2.1, at the world average top mass of 172.5 GeV/c^2, and normalized at the theoretical cross section for this mass of 7.23 pb [50]. The event yield, and kinematic distributions

	Inputs to MC						
Dataset name	$m_{\tilde{t}}$, GeV	M_2, GeV	M_1, GeV	$m_{\tilde{\chi}_1^+}$, GeV	$m_{\tilde{\chi}_1^0}$, GeV	NLO Cross Section, pb	DIL BR %
stopab	155	110	60	105.8	58.8	1.23	25.8
stopbb	155	110	45	105.8	43.9	1.23	10.5
stopcb	135	110	45	105.8	43.9	2.77	10.5
stopdb	135	110	60	105.8	58.8	2.77	25.8
stopeb	155	110	45	105.8	43.9	1.23	27.3
stopfb	155	130	60	125.8	58.8	1.23	28.4
stopgb	135	130	60	105.8	58.8	2.77	28.4
stophb	135	110	45	105.8	43.9	2.77	27.3
stopvb	115	110	45	105.8	43.9	6.89	27.3
stopub	115	110	60	105.8	58.8	6.89	25.8
stopxb	115	110	90	105.8	88.5	6.89	15.9
stopyb	135	110	90	105.8	88.5	2.77	15.9
stopzb	155	110	90	105.8	88.5	1.23	15.9
stopac	185	110	90	105.8	88.5	0.416	15.9
stopbc	185	110	60	105.8	58.8	0.416	25.8
stopcc	185	110	45	105.8	43.9	0.416	27.3
stopdc	135	130	90	125.8	88.5	2.77	23.7
stopec	155	130	90	125.8	88.5	1.23	23.7
stopfc	185	130	90	125.8	88.5	0.416	23.7
stopgc	185	130	60	125.8	58.8	0.416	28.4
stophc	185	130	45	125.8	43.9	0.416	10.5
stopic	215	130	45	125.5	43.9	0.156	10.5
stopjc	215	130	60	125.5	58.8	0.156	28.5
stopkc	135	130	110	125.5	108.4	2.77	16.3
stoplc	155	130	110	125.5	108.4	1.23	16.3
stopmc	185	130	110	125.5	108.4	0.416	16.4

TABLE 4.1. Non-systematic and non-"check" stop Monte Carlo samples used in this paper. The first column corresponds to the name the samples are stored under in the CDF software system. All samples were generated with $\tan\beta = 5$. The NLO cross section is in pb for $\tilde{t}\bar{\tilde{t}}$ production at the Tevatron, using CTEQ6M (NLO) [37] parton distribution functions, and where obtained using PROSPINO 2.0 [49] at the nominal renormalization/factorization scales.

are estimated using the techniques of section 4.4. It can be seen from figure 4.9 that the final state event signature of the $t\bar{t}$ events will look the same to the detector as $\tilde{t}_1\bar{\tilde{t}}_1$ events. Similar to $\tilde{t}_1\bar{\tilde{t}}_1$ events, it is required for both the top and anti-top quarks to decay semi-leptonically at truth level, since jets faking leptons are modeled using fake leptons (see section 3.2.6.2).

4.5.2.1. *Reducing the $t\bar{t}$ Background.* With typical cuts on variables such as jet E_T, $\not{E}_T$, H_T, etc., it is hard to reduce this background without also more drastically reducing signal, or letting in copious amounts of other backgrounds. However it is possible to take advantage of the differing decay topologies of stop and top events due to top being a fermion, and stop a scalar. A correlation of variables which is especially sensitive to this different topology is $\Delta\phi(\text{leptons}) \times \Delta\phi(\text{jets})$ verses H_T, as can be seen in figure 4.10. The H_T distribution can be seen in figure 4.7, while the $\Delta\phi(\text{leptons}) \times \Delta\phi(\text{jets})$ distribution can be seen in figure 4.11, from which one can conclude exploiting the correlation between these variables is much more powerful than cutting on either variable alone.

Making a cut in this plane at $H_T \leq 215 + \frac{\Delta\phi(\text{jet}_1,\text{jet}_2)\times\Delta\phi(\text{lep}_1,\text{lep}_2)}{\pi^2} \times 325$ reduces top by a factor of 2, and stop by only 15%. For reference with the final event selection (Chapter [?]) 49.0±6.9 top events are expected in the b-tagged channel, and 25.2±3.3 in the non-tagged channel.

4.5.3. Diboson Event Signatures. WW, WZ, and ZZ events are simulated using inclusive PYTHIA event generation as described in section 3.2.2.1, with each inclusive process being fixed to the NLO theoretical cross section [51] listed in table 4.2. The W+$\gamma^\star$ events represent a very small background, and are simulated using the BAUR Monte Carlo, as seen in table 4.2. These processes represent small backgrounds which can be reduced by higher jet E_T or $\not{E}_T$ requirements. For reference with the final event selection (Chapter 9) 0.5±0.1 diboson events are expected in the b-tagged channel, and 6.0±1.3 in the non-tagged channel.

4.5.4. Z/γ^*+Jets Event Signatures. The Z/γ^*+Jets background is by far the most complex Monte Carlo background to estimate from an analysis point of view. First the inclusive Z/γ^* production cross section must be measured in the observed data sample (as opposed to using the NLO cross section like other processes) in order to minimize the systematics of this background; many Monte Carlo samples of different invariant mass ranges,

Physics Process	Generator	NLO Cross Section (pb)
WW	PYTHIA	12.4
WZ	PYTHIA	3.7
ZZ	PYTHIA	3.8
$W\gamma \rightarrow e\nu$	BAUR	32 × 1.36

TABLE 4.2. Diboson SM Monte Carlo samples and their respective NLO cross sections [51].

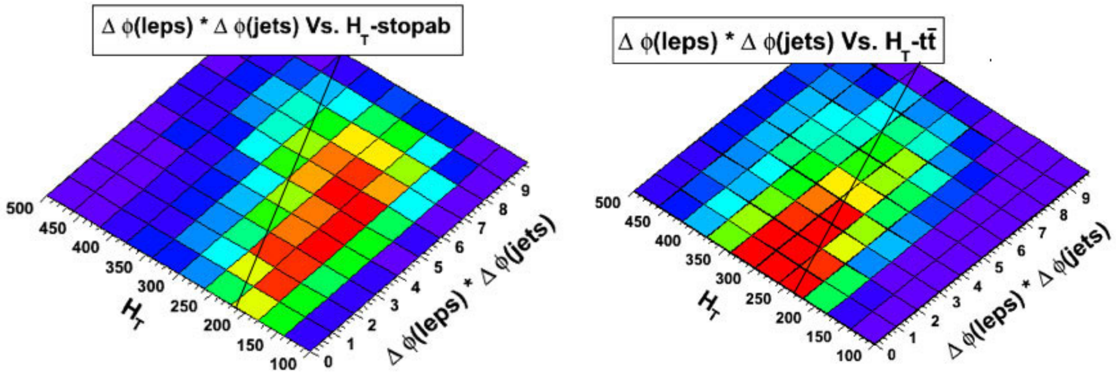

Figure 4.10. $\Delta\phi\,(\mathrm{jet}_1, \mathrm{jet}_2) \times \Delta\phi\,(\mathrm{lep}_1, \mathrm{lep}_2)$ verses H_T for $\tilde{t}_1\bar{\tilde{t}}_1$ events (left) and $t\bar{t}$ events (right). The $\Delta\phi\,(\mathrm{leptons}) \times \Delta\phi\,(\mathrm{jets})$ variable provides nice discrimination between the spin 1/2 top quark events, and spin 0 stop events, which when combined with H_T nicely separates signal from background. The black line corresponds to $H_T = 215 + \frac{\Delta\phi(\mathrm{jet}_1,\mathrm{jet}_2)\times\Delta\phi(\mathrm{lep}_1,\mathrm{lep}_2)}{\pi^2} \times 325$, which is the cut in this plane chosen for final event selection. The stop shown has SUSY masses of $m(\tilde{t}_1) = 155\ \mathrm{GeV}/c^2$, $m(\tilde{\chi}_1^{\pm}) = 105.8\ \mathrm{GeV}/c^2$, and $m(\tilde{\chi}_1^0) = 58.8\ \mathrm{GeV}/c^2$.

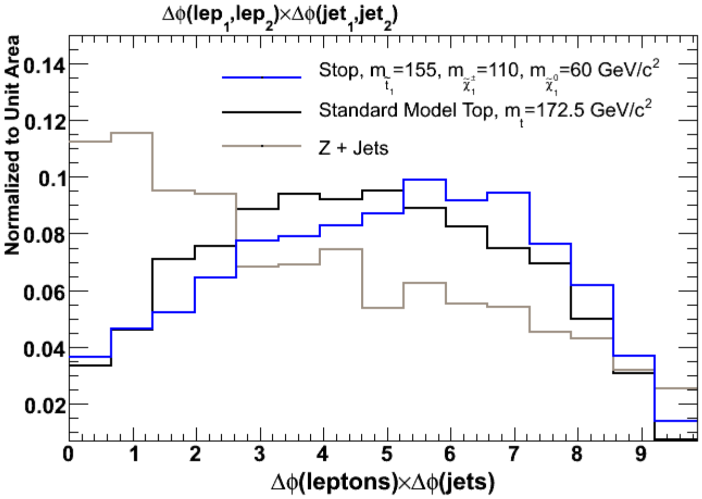

Figure 4.11. The $\Delta\phi\,(\mathrm{jet}_1, \mathrm{jet}_2) \times \Delta\phi\,(\mathrm{lep}_1, \mathrm{lep}_2)$ distribution for stop, top, and Z + Jets events, for an example SUSY mass scenario of $m(\tilde{t}_1) = 155\ \mathrm{GeV}/c^2$, $m(\tilde{\chi}_1^{\pm}) = 105.8\ \mathrm{GeV}/c^2$, and $m(\tilde{\chi}_1^0) = 58.8\ \mathrm{GeV}/c^2$.

different jet multiplicities, different lepton types (e, μ, τ), and seperately Z/γ^*+light-flavor and Z/γ^*+heavy-flavor must be combined using various techniques, so as to improve modeling and reduce Monte Carlo based statistical errors; then since the N-Jet spectrum of simulation does not match that of the observed data sample, this must further be corrected for; the mistag matrix used on Monte Carlo must be scaled according to a derived scale factor; and finally since simulation of Z/γ^*+heavy-flavor is only to leading order, it does not properly predict the fraction of heavy flavor events, so this must be corrected for. These corrections are described below:

4.5.4.1. *Z/γ^* Monte Carlo Sample Combinations.* As noted in section 3.2.2.2 , Z/γ^* is modeled using ALPGEN with separate Matrix Elements for 0, 1, 2, 3, and $\geq$4 jet processes, which must be combined together to model the inclusive Z/γ^* process. Also, since the $Z/\gamma^*+c\bar{c}$+light-flavor jets and $Z/\gamma^*+b\bar{b}$+light-flavor jets production cross sections are much lower than only light flavor jets, the heavy-flavor (HF) processes are generated separately from light-flavor (LF) processes, to reduce the number of events which need to be generated in order to have acceptable Monte Carlo statistics in the b-tagged channel; therefore these processes must be combined together, according to the weights in equation 4.7 using the LO cross sections for each specific sub-process. Similarly, since events near the Z's pole-mass will be required to pass a special veto which will significantly suppress them, in order to model events on the low and high mass tails which will pass this veto with a proper amount of Monte Carlo statistics (since these events will rarely be generated if the entire mass range is simulated in the same sample), the Z/γ^*+X samples are generated in four invariant mass ranges: $[0, 20], [20, 75], [75, 105], [105, 600]$ and combined according to equation 4.7 using the LO cross section for each respective mass range.

4.5.4.2. *Z/γ^* Inclusive Cross Section K-factor.* Since the ALPGEN is the LO matrix element generator, its cross sections for $Z/\gamma^\star \to \ell^+\ell^-$ production need to be corrected to account for NLO effects. All Z/γ^* Monte Carlo samples are combined according to their relative LO cross sections and then normalized to the observed data sample in the Z mass peak and low missing E_T region: 76 GeV$/c^2 < m_{\ell\ell} <$ 106 GeV$/c^2$ with $\not\!\!E_T <$ 20 GeV; a region where nearly no signal is expected. The K-factors for each ee or $\mu\mu$ dilepton category is presented in Table 4.3. For categories including CMX muons, only events with at least one jet $E_T >$ 15 GeV are considered; since for some periods of time, data was collected on a trigger which required a CMX muon and a $E_T \geq$ 10 GeV uncorrected jet. The overall K-factor, denoted K_Z, for the $Z/\gamma^\star \to \ell^+\ell^-$ events is obtained by combining all of the dilepton categories and is found to be K_Z =1.44. For book keeping purposes, this factor is found after correcting the fraction of heavy flavor events in Monte Carlo to be the same as the observed data sample, as described in section 4.5.4.4.

Dilepton Category	K-factor
CEM_CEM	1.44 ± 0.01
CEM_NICEM	1.54 ± 0.03
CEM_PHX	1.40 ± 0.01
PHX_NICEM	1.45 ± 0.03
CMUP_CMUP	1.49 ± 0.01
CMUP_NICMUP	1.82 ± 0.07
CMUP_CMU	1.56 ± 0.02
CMUP_NICMU	1.98 ± 0.14
CMUP_CMP	1.48 ± 0.02
CMUP_NICMP	1.75 ± 0.12
CMUP_CMX	1.52 ± 0.03
CMUP_NICMX	1.76 ± 0.10
CMX_NICMUP	1.89 ± 0.11
CMUP_CMIO	1.38 ± 0.02
CMX_CMX	1.38 ± 0.04
CMX_NICMX	1.46 ± 0.12
CMX_CMU	1.51 ± 0.06
CMX_NICMU	1.85 ± 0.23
CMX_CMP	1.37 ± 0.05
CMX_NICMP	1.35 ± 0.17
CMX_CMIO	1.43 ± 0.07
All_Leptons	1.44 ± 0.01

TABLE 4.3. NLO K-factors for $Z/\gamma^\star$ events in various dilepton categories. Errors are statistical only.

4.5.4.3. *Z/γ^* N-Jet Scale Factors.* Although the ALPGEN generator takes care of the correct matrix element treatment for $Z/\gamma^\star \to \ell^+\ell^-$ production in association with jets, the jet multiplicity distribution does not agree with the observed data sample perfectly. It was noted that the agreement can be improved if one shifts the Q^2 or the JES scale [52]. Instead an N_{jet} scale factors relative to the global K-factor is applied to correct for the number of $Z/\gamma^\star \to \ell^+\ell^-$ events per each jet multiplicity bin: 0, 1 and ≥ 2. The N_{jet} scale factor in general depends on the jet energy thresholds. Table 4.4 shows the N_{jet} scale factors (denoted K^i_{N-jet}, where 1 refers to jet multiplicity) for the leading jet $E_T > 15$ GeV, and the second jet $E_T > 12$ GeV.

4.5.4.4. *Z/γ^* Heavy Flavor Fraction and Mistag Corrections.* On top of the overall Z cross section and N-Jet K-factors, an additional K-factor is needed to correct for the heavy-flavor (K_{HF}) fraction observed in the real data being different than Monte Carlo predicts (due to Monte Carlo being LO), and also to correct for the rate of mistags in Monte Carlo verses the real data K_{mistag}. The mistag K-factor is simple the number of mistags predicted in the observed data sample (using the mistag matrix), divided by the number predicted by the mistag matrix run over light-flavor Monte Carlo samples: The heavy-flavor K-factor is determined by

$$K^{i}_{HF} = \left(N^{tagged,\,i}_{data} - N^{mistag,\,i}_{data}\right) / K_Z N^{tagged,\,i}_{HF\;MC} \tag{4.10}$$

where i indicates either the 1 jet bin, or ≥2 jet bin. An additional factor K^{i}_{LF} must be introduced in order to ensure $N^{pretag,\,i}_{data} = K_{LF} N_{MC\;LF} + K_{HF} N_{MC\;HF}$. The mistag K-factor is then simply:

$$K_{mistag} = N^{mistag}_{data} / K_{LF} N^{mistag}_{LF\;MC} \tag{4.11}$$

and is found to be 1.06, however for simplicity since this is consistent with unity within errors, a factor of 1.0 is used.

A technical problem prevented generating $Z/\gamma^\star + c\bar{c}$ with Z masses below 75 GeV/c^2, therefore since the event kinematics of $Z/\gamma^\star + c\bar{c}$ and $Z/\gamma^\star + b\bar{b}$ are the same and only differ by b-tagging probabilities, $Z/\gamma^\star + b\bar{b}$ Monte Carlo is used to represent Z + heavy flavor events, since the Z + heavy flavor scale factor is fit for anyway. The heavy flavor scale factors using jet thresholds of 15 GeV for the leading and 12 GeV for the second jet is computed without $Z + c\bar{c}$ contribution and are given in Table 4.5, and used in this

	0j	1j	≥ 2j
ee	0.983 ± 0.003	0.937 ± 0.008	1.178 ± 0.016
$\mu\mu$	1.021 ± 0.007	1.015 ± 0.011	1.189 ± 0.018
Total	0.992 ± 0.019	0.969 ± 0.040	1.182 ± 0.011

TABLE 4.4. Jet bin correction factors (K^{i}_{N-jet}) for Z events obtained within the Z mass peak region 76 GeV/c^2 $< m_{\ell\ell} <$ 106 GeV/c^2 relative to the total K-factor = 1.44. The third row represents the N_{jet} scale factor for combined $ee + \mu\mu$ events; half of the discrepancy between ee and $\mu\mu$ channels is added in quadrature to the statistical uncertainty of the fit. These numbers are for the jet definition which requires the lead jet to have $E_T > 15$ GeV, and the second jet to have $E_T > 12$ GeV, as was used for the final event selection in the b-tagged channel.

analysis. It is of note that if $Z/\gamma^\star + c\bar{c}$ Monte Carlo is used under the Z-mass peak, then the heavy-flavor K-factors agree well with NLO theoretical predictions.

After applying all these scale factors we have effectively fixed it so $Z/\gamma^\star$ Monte Carlo predicts exactly the same number of events as observed in the real data sample, for pre-tag, tagged, and mistagged events. Although being derived in a region were signal is not expected, these same $K-factors$ are applied to the $Z/\gamma^\star$ Monte Carlo in the signal regions.

	1j	$\geq$ 2j
ee	2.31 ± 0.10	1.44 ± 0.10
$\mu\mu$	2.90 ± 0.11	1.43 ± 0.10
Total	2.57 ± 0.15	1.44 ± 0.07

Table 4.5. Jet bin correction factors for Z + heavy flavor events without $Z + c\bar{c}$ events. The uncertainty on the total scale factor takes into account statistical uncertainty added in quadrature to half of the discrepancy between ee and $\mu\mu$ channels.

4.5.4.5. *Reducing the $Z/\gamma^\star$ Background.* The $Z/\gamma^\star$ background is reduced through requiring a b-tagg, increasing jet E_T thresholds, or increasing the $\not{E}_T$ cut as can be seen in Figures 4.7 and 4.6. Also if ee or $\mu\mu$ events have an invariant mass near the Z-pole, and additional met significance cut of 4 GeV can be applied; where met significance is defined as:

$$\text{Met Significance} \equiv \frac{\not{E}_T}{\sqrt{\sum E_T}} > 4 \text{ GeV}, \tag{4.12}$$

For reference with the final event selection (Chapter 9) 4.0±0.5 Z + Jets events are expected in the b-tagged channel, and 25.0±5.3 in the non-tagged channel.

4.5.5. W+Jets Event Signatures - Fake Lepton. As described in section 3.2.6.2 this background is modeled using events in the real data sample which have at least one fakeable lepton and exactly one fully identified lepton. These events are required to pass the same event selection cuts as other processes once the fake-lepton has been promoted to be treated in the same way as regular leptons, only with each event entering the background estimation with a weight equal to the leptons fake rate. There are no cuts targeted at specifically reducing this background; however it is small, and is reduced through the standard cuts like jet E_T. For reference with the final event selection (Chapter 9) 2.8±0.9 fakeable events are expected in the b-tagged channel, and 9.8±2.9 in the non-tagged channel.

CHAPTER 5

Stop Event Reconstruction

The reconstructed stop mass proved to be an ideal discrimination variable between $\tilde{t}_1\bar{\tilde{t}}_1$ events and the Standard Model for many reasons, including:

- The reconstructed stop mass of $\tilde{t}_1\bar{\tilde{t}}_1$ events produces a more resonant structure than SM events, due to $\tilde{t}_1\bar{\tilde{t}}_1$ events better satisfying the $\tilde{t}_1\bar{\tilde{t}}_1$ decay hypothesis.
- It provides a variable which smoothly changes according to the SUSY masses, allowing interpolation of the reconstructed stop mass template between generated Monte Carlo samples. This allows the setting of smooth exclusion regions, rather than just exclusions for the finite number of signal Monte Carlo samples which could be generated. The results can consequently be interpreted in a more meaningful manner.
- Since event reconstruction takes into account nearly all the available information in the event, including the complicated relations of measured quantities, the discrimination power of the reconstructed stop mass is competitive with the discrimination power of multivariate techniques such as artificial neural networks.
- Unlike multivariate techniques which would need to be retrained for individual SUSY mass scenarios, the reconstructed stop mass provides a universal solution. It was found using an artificial neural network on a different SUSY mass scenario than it was trained on often resulted in losing almost all of the discrimination power.

Complete reconstruction of the $\tilde{t}_1\bar{\tilde{t}}_1$ events in the dilepton channel is a challenging endeavor since only four of the eight final state particles are detected. By using the invariant mass constraints of intermediate particles, determining the transverse momentum sum of the undetected particles by the $\not{E}_T$, using a approximation prompted by only caring about the sum of the neutrino and neutralino on each side of the event, taking the mass of the $\tilde{\chi}_1^{\pm}$ as a parameter of the reconstruction, and using a weighted sum over all possible directions of undetected particles, a decent event reconstruction can be performed. This allows the computation of the reconstructed stop mass.

The basic steps of reconstructing dilepton events under the $\tilde{t}_1\bar{\tilde{t}}_1$ hypothesis is as follows:

- Assignment of jets to either the b or $\bar{b}$ parton.
- Approximation of the neutrino and neutralino on each side of the decay as one massive *Psuedo-Particle*, since only the sum of the $\tilde{\chi}_1^0$ and ν are relevant to reconstruct the $\tilde{t}_1$ or $\bar{\tilde{t}}_1$ mass and kinematics.
- Mass and $\not\!\!E_T$ constraints are utilized to solve for the Psuedo-Particle's kinematics.
- A χ^2 is formed for a given direction of undetected particles, which gives a measure of how well the event fits the $\tilde{t}_1\bar{\tilde{t}}_1$ hypothesis. This χ^2 is minimized with respect to all uncertainties.
- A weighted sum of the stop mass is performed over all possible invisible particle directions to obtain an expected value of this quantity.

It should be noted that this reconstruction algorithm is an extension of the *neutrino-ϕ weighting algorithm* pioneering in Run I of the Tevatron to measure the top quark mass [45].

5.1. Stop Reconstruction

5.1.1. Jet-To-Parton Assignment. Correctly identifying which jet corresponds to the b or $\bar{b}$ quarks greatly affects reconstruction resolution of the stop mass and ensures the discrimination between $\tilde{t}_1\bar{\tilde{t}}_1$ and the SM. Two methods were considered to determine the jet-to-parton (or equivalently jet-to-lepton) assignment: picking the assignment which minimizes the sum of χ^2 (equation 5.1.4) over all the invisible particle directions, or using the invariant masses of the leptons and jets to determine pairing. The first method yielded proper jet-to-lepton assignment 60-70% of the time, depending on the SUSY masses. The second method achieved correct pairing 85%-90% of the time, and was therefore chosen for this analysis. The importance of the correct assignment is demonstrated in Fig. 5.1.

To determine proper pairing, the two highest E_T jets are assumed to be the b-quark jets in the event, and are matched to the proper leptons using logic based on the jet-lepton invariant mass quantities by the following method:

$\Delta M_1 = M\left(Jet_1 + lep\right) - M\left(Jet_2 + lep\right)$

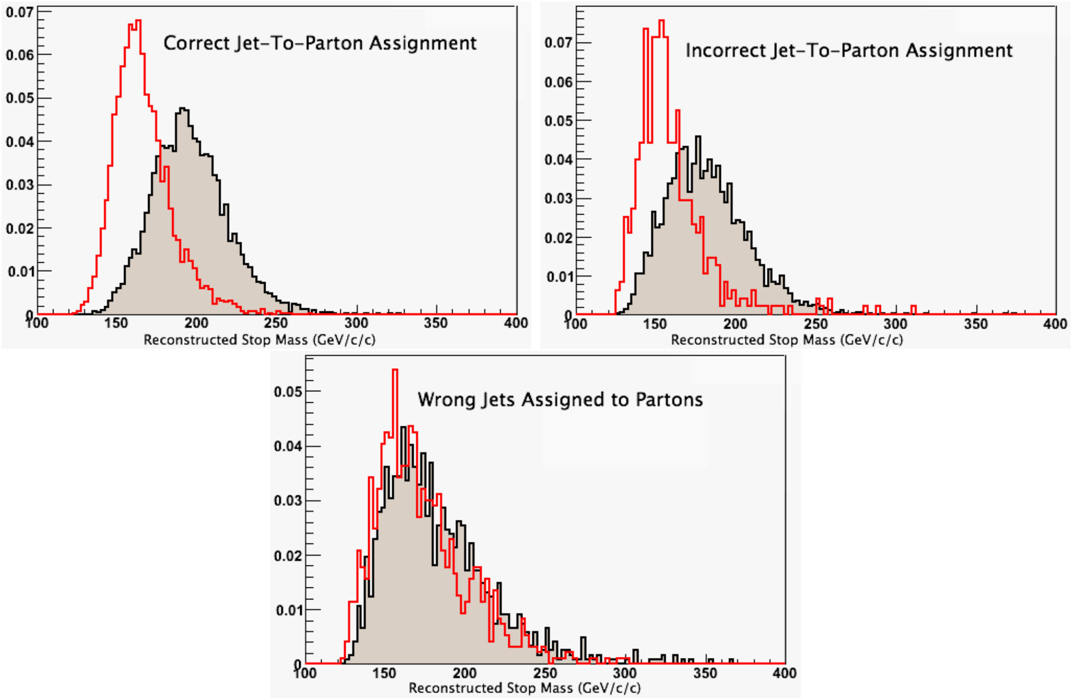

FIGURE 5.1. The reconstructed stop mass for stop events (red) over top events (black) Top Left: the correct b-jet - lepton assignment has been made (for both stop and top). Top Right: incorrect b-jet asignment chosen (for both stop and top). Bottom: at least one of the jets selected was not the b or $\bar{b}$ parton. SUSY masses of $m(\tilde{t}_1) = 155$ GeV/c^2, $m(\tilde{\chi}_1^{\pm}) = 105.8$ GeV/c^2, and $m(\tilde{\chi}_1^0) = 58.8$ GeV/c^2, is used.

$$\Delta M_2 = M\left(Jet_1 + \overline{lep}\right) - M\left(Jet_2 + \overline{lep}\right)$$

if $\Delta M_1 > \Delta M_2$ then Jet_1 is the b-jet, Jet_2 is the $\bar{b}$-jet.

if $\Delta M_2 > \Delta M_1$ then Jet_2 is the b-jet, Jet_1 is the $\bar{b}$-jet.

When the two b-candidates are correctly isolated, this procedure results in choosing the correct jet-to-lepton matching 85 to 95% of the time, depending on the stop sample, as opposed to 60-70% of the time based on using the χ^2.

5.1.2. Pseudoparticle Approximation. One of the most important approximations made in this reconstruction algorithm is the combination of the four-momenta of the $\tilde{\chi}_1^0$ and ν on each side of the decay (either the $\tilde{t}_1$ or $\bar{\tilde{t}}_1$ side of the decay), so as to treat them as one massive pseudoparticle. This approximation is valid since we do not care about the individual momentum of the undetected particles, but only the sum of them for each side of the decay when determining the mass and momentum of the $\tilde{t}_1$ and $\bar{\tilde{t}}_1$ particles. This approximation works so well since the $\tilde{\chi}_1^0$ and ν on each side of the event form an invariant mass similar to that of a particle with a large width. The invariant mass of the $\tilde{\chi}_1^0$ and ν can be seen for the two distinct cases of a virtual or real W in the event, in Fig. 5.2. The mass of such a pseudoparticle is chosen to be 75 GeV, and assigned a width of 5 GeV. The width was both doubled and halved, with no significant effect on the reconstructed mass observed. It was found that the signal Monte Carlo samples used in this paper followed pseudoparticle mass distributions similar to one of the two distributions in Fig. 5.2. This pseudoparticle approximation effectively reduces the number of undetected particles in the fit to approximately two.

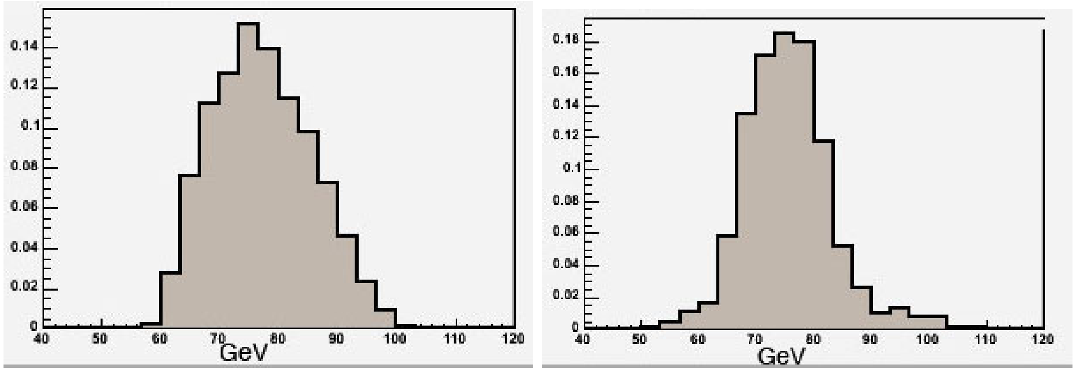

FIGURE 5.2. The invariant mass of the pseudoparticle ($\tilde{\chi}_1^0 + \nu$) at the generator level. The plot on the left corresponds to $\tilde{t}_1$ mass of 155 GeV, $\tilde{\chi}_1^\pm$ mass of 130 GeV, $\tilde{\chi}_1^0$ mass of 45 GeV. The right plot corresponds to $\tilde{t}_1$ mass of 135 GeV, $\tilde{\chi}_1^\pm$ mass of 110 GeV, $\tilde{\chi}_1^0$ mass of 60 GeV. The shape of this pseudoparticle's mass depends on whether the event has a real (right) or virtual (left) W boson. It is found that all stop samples generated have approximately these two distributions of pseudoparticle masses.

5.1.3. Mass and $\not\!\!E_T$ Constraints Utilized.

5.1.3.1. $\tilde{\chi}_1^\pm$ - *Mass Constraint.* In general, the chargino mass in an unknown parameter. However, the event reconstruction can be helped if it is set to a fixed value. In the stop mass reconstruction algorithm, the $m_{\tilde{\chi}_1^\pm}$ serves as an input variable. The reconstruction is performed for two different values of $m_{\tilde{\chi}_1^\pm}$ as specified in table 4.1, corresponding to the chargino masses the exclusion limits are determined for. The Standard Model backgrounds and data are reconstructed under each of the two $m_{\tilde{\chi}_1^\pm}$ hypotheses, and are used for setting the respective limits.

5.1.3.2. *Solving for Pseudoparticle Kinematics.* After making the pseudoparticle approximation, choosing the jet-to-lepton pairing, and placing the $\tilde{\chi}_1^{\pm}$ - mass constraint, the event kinematics are still underconstrained (a -1C system), such that it is not possible to reconstruct kinematics of the event uniquely. To compensate two quantities, the pseudoparticle ϕ's, will be assumed (creating a +1C system), so that event kinematics can be solved for, and χ^2 to the $\tilde{t}_1\bar{\tilde{t}}_1$ hypothesis can be formed; given these two assumptions. An integration over the two assumed variables can then be performed, using the χ^2 to form a likelihood to weight each value of assumptions by, and thus obtain expected quantities. The method developed is similar to that of the top dilepton neutrino weighting technique [45]. The integration over possible pseudoparticle directions is performed in a net of 12 possible ϕ-directions ($0 < \phi < \pi$) of the four-momenta of each pseudoparticle, i.e. 144 various combinations of $(\phi_{PP_1}, \phi_{PP_2})$ are considered in total. For a given $(\phi_{PP_1}, \phi_{PP_2})$, the transverse momentum of the pseudoparticles may then be solved for from the following set of equations:

$$p_T^{PP_1} = \frac{\not{E}_x \sin(\phi_{PP_2}) - \not{E}_y \cos(\phi_{PP_2})}{\sin(\phi_{PP_2} - \phi_{PP_1})}, \tag{5.1}$$

$$p_T^{PP_2} = \frac{\not{E}_x \sin(\phi_{PP_1}) - \not{E}_y \cos(\phi_{PP_1})}{\sin(\phi_{PP_1} - \phi_{PP_2})} \tag{5.2}$$

where the p_z of the pseudoparticles is then determined from the invariant mass constraint of the $\tilde{\chi}_1^{\pm}$, by the equations:

$$p_z^{PP} = \frac{-b \pm \sqrt{b^2 - 4ac}}{2a} \tag{5.3}$$

where

$$a = p_\ell^{z^2} - E_\ell^2 \tag{5.4}$$

$$b = 2dp_\ell^z \tag{5.5}$$

$$c = d^2 - E_\ell^2 \left(P_{PP}^{x^2} + P_{PP}^{y^2} + M_{PP}^2 \right) \tag{5.6}$$

$$d = \frac{1}{2}M^2_{\tilde{\chi}_1^\pm} - \frac{1}{2}M^2_{PP} + p^x_{PP}p^x_\ell + p^y_{PP}p^y_\ell \tag{5.7}$$

Where ℓ is the lepton paired to its corresponding pseudoparticle. It is worth noting that varying ϕ's between 0 and π is sufficient because adding π to ϕ only swaps the sign of p_T in equations 5.1 and 5.2. Since the equation 5.1 and 5.2 break down when the ϕ of both pseudoparticles is the same, this point is avoided by offsetting the ϕ's used by $\pi/24$. Summing over both ϕ's is equivalent to summing over all possible directions of pseudoparticles, since the p_T and p_z of the pseudoparticles can be determined for a given $(\phi_{PP_1}, \phi_{PP_2})$.

5.1.4. The χ^2 function.

The χ^2 function is constructed as follows

$$\begin{aligned}
\chi^2 = & \frac{\left(\vec{\ell}_{meas} - \vec{\ell}_{fit}\right)^2}{\sigma^2_\ell} + \frac{\left(\vec{\bar{\ell}}_{meas} - \vec{\bar{\ell}}_{fit}\right)^2}{\sigma^2_\ell} + \frac{\left(\vec{u}_{meas} - \vec{u}_{fit}\right)^2}{\sigma^2_{uncl}} \\
& + \sum_{jets\, i} \frac{\left(\vec{j}_{i_{meas}} - \vec{j}_{i_{fit}}\right)}{\sigma^2_{jet_i}} + \frac{\left(M^{fit}_{PP_1} - M^{assume}_{PP}\right)^2}{\Gamma^{hepg}_{PP}} \\
& + \frac{\left(M^{fit}_{PP_2} - M^{assume}_{PP}\right)^2}{\Gamma^{hepg}_{PP}} + \frac{\left(M_{PP_1,\ell} - M_{\tilde{\chi}^\pm}\right)^2}{\Gamma^{\tilde{\chi}^\pm}} \\
& + \frac{\left(M_{PP_1,\bar{\ell}} - M_{\tilde{\chi}^\pm}\right)^2}{\Gamma^{\tilde{\chi}^\pm}} + \frac{\left(M_{PP_1,\bar{\ell},b_{jet}} - M_{PP_2,l,\bar{b}_{jet}}\right)}{\Gamma^{\tilde{t}}}
\end{aligned} \tag{5.8}$$

Where $\vec{\ell}_{meas}$ is the lepton measured momentum, $\vec{\ell}_{fit}$ is the fitted lepton momentum. Similarly, u refers to the unclustered energy in the event, which includes all jets except for b-jets assumed to be originating from the stop decay. PP_i are pseudoparticles. The first four terms in the χ^2 function refer to how the measured physics quantities are allowed to vary within their esimated uncertainties. The lepton momentum σ_ℓ values are taken from Ref. [27] and the unclustered energy is from Ref. [53]. The uncertainties on the jet momenta σ_{jet}'s are top specific uncertainties from Ref. [54]. With no deep insight on what widths of supersymmetric particles should be, the widths are chosen to be $\Gamma_{\tilde{\chi}^\pm} = \Gamma_W = 2.12$ GeV$/c^2$ and $\Gamma_{\tilde{t}_1} = \Gamma_t = 1.5$ GeV$/c^2$, and verified that using half or double these values does not significantly impact the reconstruction.

5.1.5. χ^2 Minimization. For each of the $(\phi_{PP_1}, \phi_{PP_2})$ direction combinations, the χ^2 is minimized via TMinuit [55]. The directions of the leptons and jets are assumed to be measured precisely, but their momenta vary according to the aforementioned uncertainties. The unclustered energy components, u_x and u_y, are allowed to vary independently of each other. The $\not{E}_T$ is constructed as the negative vector sum of the fit momenta of the leptons, jets, and unclustered energy, such that it dynamically changes in the fit. The p_z's of the pseudoparticles are free parameters in the TMinuit fit. However, the starting values of p_z of the pseudoparticles are obtained from equations 5.3-5.7. There are two possible values of p_z for each pseudoparticle obtained from the quadratic equations, therefore giving four possible starting combinations of p_z values. All four starting values are separately minimized, and only the p_z combination that gives the lowest χ^2 is kept.

5.1.6. Weighted Mass. To find the weighted mass, or rather what is referred to in this paper as *reconstructed mass*, each ϕ-combination of the pseudoparticles directions is considered, then a sum weighted according to the minimized χ^2 is performed over the reconstructed stop masses for all possible ϕ-combinations. The reconstructed stop mass of an event is determined by the following relation:

$$M_{\tilde{t}_1}^{Reco} = \frac{1}{\sum_{\phi\, i,j} e^{-\chi^2_{i,j}}} \sum_{\phi\, i,j} M_{i,j}^{fit} e^{-\chi^2_{i,j}} \tag{5.9}$$

where i and j indicate the ϕ positions of the Psuedo-Particles.

5.1.7. Performance of Reconstruction. The reconstruction technique can be tested by determining how well it reconstructs event kinematics. Specifically if the reconstruction gets the directions of the pseudoparticles and stop quarks correct, it provides confidence the algorithm is working as intended. These distributions can be seen in Figures 5.4 and 5.4, where it is seen that the reconstructed directions are very near the truth-level directions of these particles.

5.1.8. Reconstructed Stop Mass. Although it is interesting to check the performance of the reconstruction algorithm on the various intermediate-state quantities as in the previous section, the real purpose of event reconstruction is to obtain the reconstructed stop mass of events with the hope signal will have a more resonant structure than backgrounds. This can be seen to be the case in Fig. 5.5. It is the case for all SUSY masses

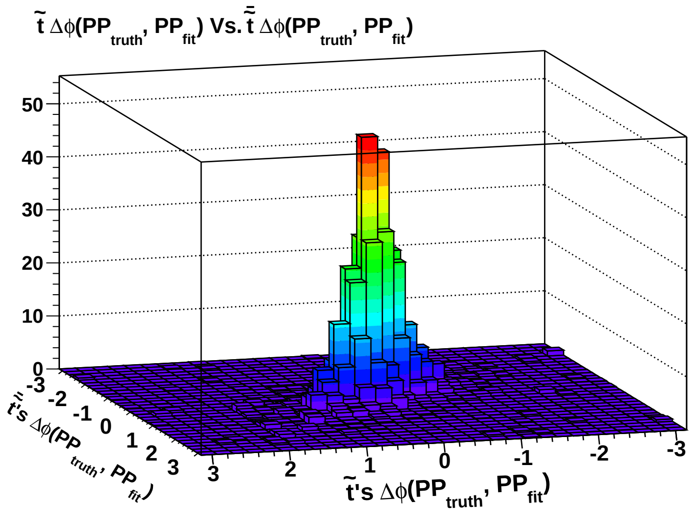

FIGURE 5.3. $\Delta\phi$ between the pseudoparticle at the truth and reconstructed levels, for each side of the decay. The peak near the origin shows that the $\tilde{t}_1\bar{\tilde{t}}_1$ event reconstruction is able to accurately reconstruct the sum of ν and $\tilde{\chi}_1^0$ on each side of the decay. SUSY masses of $m(\tilde{t}_1) = 155$ GeV/c^2, $m(\tilde{\chi}_1^{\pm}) = 105.8$ GeV/c^2, and $m(\tilde{\chi}_1^0) = 58.8$ GeV/c^2, are used for this plot.

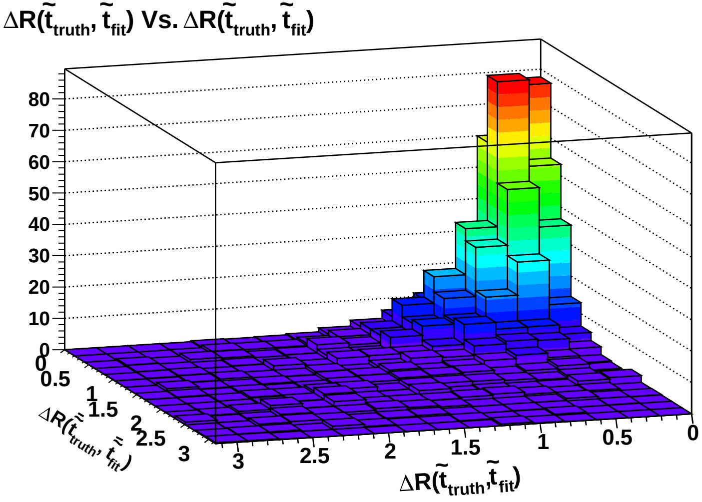

FIGURE 5.4. ΔR between the truth level, and reconstructed stop and anti-stop four-vectors. The fact that the distribution peaks near the origin shows that the $\tilde{t}_1\bar{\tilde{t}}_1$ event reconstruction is able to reconstruct the direction of the $\tilde{t}_1$ and $\bar{\tilde{t}}_1$ particles. SUSY masses of $m(\tilde{t}_1) = 155$ GeV/c^2, $m(\tilde{\chi}_1^{\pm}) = 105.8$ GeV/c^2, and $m(\tilde{\chi}_1^0) = 58.8$ GeV/c^2, are used for this plot.

investigated in this paper that stop has a narrower structure than the Standard Model backgrounds. At higher stop masses the discrimination power between signal and Standard Model is diminished, as seen in Fig. 5.5, resulting in lower sensitivity to exclusion for these masses. The reconstructed stop mass provides a nice discriminant for the SUSY masses of primary interest to this analysis.

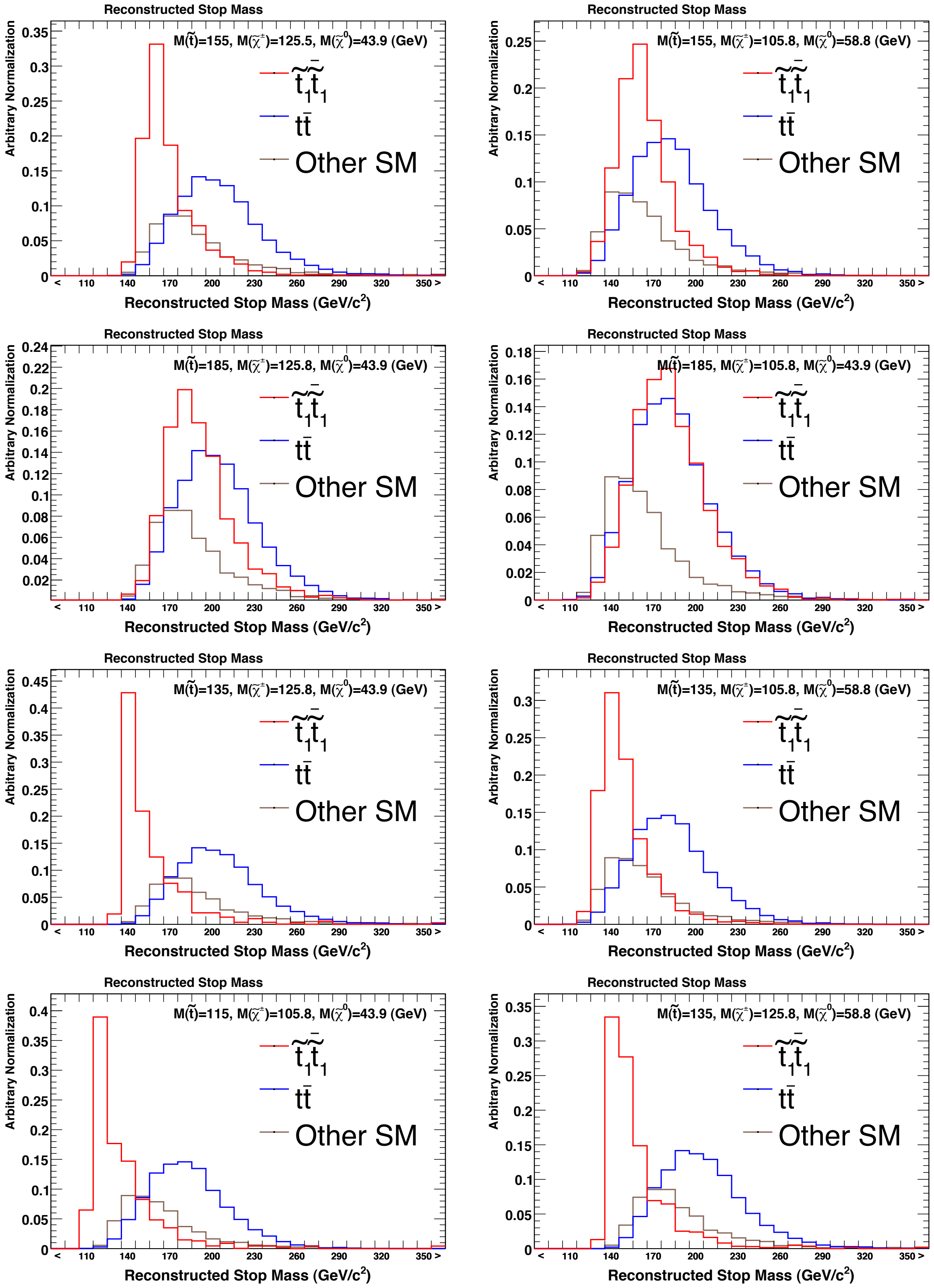

FIGURE 5.5. Comparisons of the reconstructed stop mass for signal (red), $t\bar{t}$ (blue), and the other Standard Model backgrounds (brown), for various SUSY mass scenarios. Signal and $t\bar{t}$ have been normalized to the same area, while the other Standard Model backgrounds are normalized to half of this same area.

CHAPTER 6

Systematic Uncertainties

Due to imperfect experimental and theoretical knowledge, this analysis takes into account a number of *systematic uncertainties* which reduce the sensitivity to signal, but in turn allow an honest statement about the exclusion confidence level. During the optimization of the event selection cuts via the genetic algorithm (Section 9), the systematic uncertainties were re-evaluated for each set of event selection cuts, so the *expected* exclusion limits could be computed taking into account how the cuts affect the systematic uncertainties using the CLs limit setting procedure described in Section 8. This chapter describes the *prescriptions* used to determine the systematic uncertainties. The rate uncertainties are listed in table 6.1, and graphical representations of the shape uncertainties for the final event selection cuts are shown throughout this chapter.

6.1. Jet Energy Scale

The uncertainty on the jet energy scale (JES) is taken into account for both its effect on event acceptance, as well as its impact on the shape of the reconstructed stop mass template. The physical sources of JES error, as well as how this error is estimated is described in section 3.1.4.2; this section describes how this uncertainty manifests in this analysis.

For the shape uncertainty, the stop mass reconstruction (Section 5) is run with the JES shifted either "up" by 2σ, or "down" by 2σ for all jets. The mass templates corresponding to $+2\sigma$ or -2σ shifted jet energy scale are then obtained by using the results of the JES shifted reconstruction for only events passing event selection for $+2\sigma$ and -2σ JES respectively. The shape systematic takes into account both the change of mass due to the shift in JES, and also the moving in and out of events from the analysis due to changing JES. As mentioned in chapter 7, horizontal morphing is used to interpolate the JES shifted templates to arbitrary values of σ_{JES} for throwing pseudo-experiments, or fitting to data.

b-tagged channel								
	JES	*b*-tag	miss-tag	ID/Trig	ISR/FSR	σ_{prod}	Top Mass	$\int \mathcal{L}\, dt$
$t\bar{t}$	-0.049, +0.036	+0.038, -0.039	±0.003	±0.012	-0.044, -0.016	±0.010	∓0.055	±0.059
Z+HF	-0.064, +0.170	-	-	-	-	±0.084	-	-
Z+LF	-0.043, +0.092	-	-	-	-	±0.021	-	-
Diboson	-0.010, -0.055	+0.034, -0.035	±0.034	±0.012	-	±0.1	-	±0.059
fakes	-	-	-	-	-	±0.3	-	-
stop	+0.120, -0.110	+0.038, -0.039	±0.003	±0.012	+0.014, -0.030	±0.178	-	±0.059

anti-tagged channel								
	JES	*b*-tag	miss-tag	ID/Trig	ISR/FSR	σ_{prod}	Top Mass	$\int \mathcal{L}\, dt$
$t\bar{t}$	-0.012, +0.010	-	∓0.001	±0.012	-0.048, -0.018	±0.010	-0.065, +0.021	±0.059
Z+HF	+0.165, +0.017	-	∓0.001	-	-	±0.138	-	-
Z+LF	+0.351, -0.180	-	∓0.002	-	-	±0.018	-	-
Diboson	+0.138, -0.151	-	∓0.001	±0.012	-	±0.1	-	±0.059
fakes	-	-	-	-	-	±0.3	-	-
stop	+0.134, -0.163	-	∓0.001	±0.012	-0.034, -0.070	±0.178	-	±0.059

TABLE 6.1. The systematic errors on acceptance due to systematic uncertainties in for the final event selection cuts used. Errors are given in fraction of acceptance gained for a 1σ shifts in the respective uncertainty. For the example stop sample, SUSY masses of $m(\tilde{t}_1) = 155\ \text{GeV}/c^2$, $m(\tilde{\chi}_1^{\pm}) = 105.8\ \text{GeV}/c^2$, and $m(\tilde{\chi}_1^0) = 58.8\ \text{GeV}/c^2$ are used. For $Z/\gamma^{\star}$+Jets σ_{prod} is the error on normalization which is experimentally found. Asymmetric errors are quoted according to positive then negative shifts of the uncertainty.

The effects of JES on acceptance for signal, top, and dibosons is determined by performing event selection with the JES shifted by $+1\sigma$ and -1σ, to determine the fraction of events which are either added to, or lost from passing the event selection cuts. This acceptance error is taken as an asymmetric error that is completely correlated with the shape error[1].

The normalization procedure for Z+Jets in section 4.5.4 is re-performed at +(-) 1 σ JES, with the resulting normalization factors used for the JES varied Z+Jet normalizations and templates in the signal region. Re-performing this procedure for the varied JES scales greatly minimizes the uncertainties on the number of $Z/\gamma^{\star}$ + Jets which enters into the analysis. The JES systematic is not applied to fake lepton background since it is obtained from data. This uncertainty is taken as correlated between all applicable Monte Carlo derived backgrounds.

6.2. Z+Jets Normalization

The normalization of Z plus light flavor jet events (Z+LF) is determined from the $76 < m_{\ell\ell} < 106$ GeV, $\not\!\!E_T < 20$ GeV region and is extrapolated into the signal region. As a systematic uncertainty for this background, the statistical uncertainty of the N_{jet} scale factor in the ≥ 2 jets bin (see section 4.5.4) is added in quadrature to half the difference of the N_{jet} scale factor as individually determined by $Z \rightarrow ee$ and $Z \rightarrow \mu\mu$ events. It should be noted that the ee and $\mu\mu$ channels are consistent with each other within statistical uncertainty. This uncertainty is dependent on the definition of jet thresholds. When the leading jet is required to have $E_T > 15$ GeV and the second jet $E_T >$12 GeV, this systematic obtains a value of 1.1%.

6.3. Z+Heavy Flavor Jets Normalization

Similarly, a rate uncertainty for normalization of the Z plus heavy flavor jet events (Z+HF) is derived in the Z mass region of $76 < m_{\ell\ell} < 106$ GeV and $\not\!\!E_T < 20$ GeV, and is taken as an uncertainty for the heavy flavor scale factor in the ≥ 2 jets bin (see section 4.5.4.4). Again, the statistical uncertainty is added in quaderature with half of the difference between the heavy flavor scale factor determined separately by $Z \rightarrow ee$ and $Z \rightarrow \mu\mu$ events. For the final set of event selection cuts in the tagged channel, were the

---

[1] Using an acceptance value for $\frac{a}{b}\sigma_{JES}$ means that the reconstructed stop mass template used will correspond to $\frac{a}{b}\sigma_{JES}$ as well.

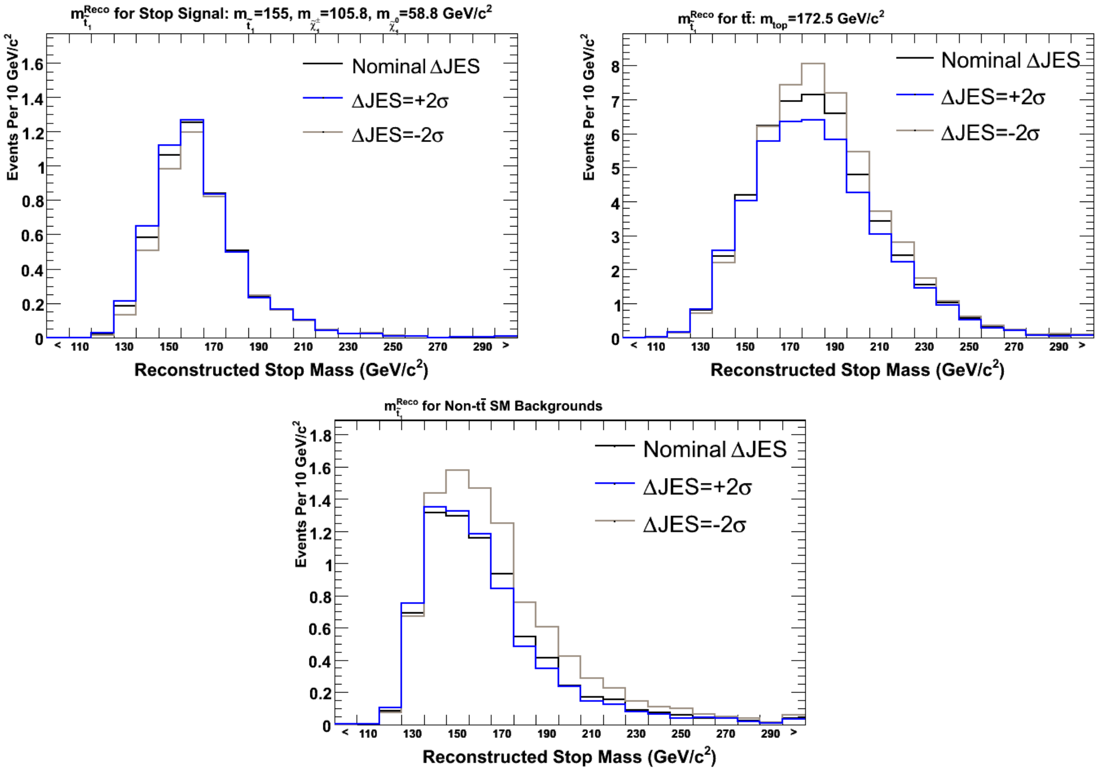

FIGURE 6.1. The effect of the JES uncertainty on the reconstructed stop mass for stop (top left), $t\bar{t}$ events (top right), and all other SM backgrounds (bottom), in the b-tagged channel using the final event selection cuts. The histograms are normalized to the expected event yields at ΔJES=-2,0,+2 respectively, with stop being plotted at a branching ratio of 0.26 for SUSY masses of $m(\tilde{t}_1) = 155$ GeV/c^2, $m(\tilde{\chi}_1^{\pm}) = 105.8$ GeV/c^2, and $m(\tilde{\chi}_1^0) = 58.8$ GeV/c^2.

leading jet $E_T > 15$ GeV and the second jet $E_T > 12$ GeV, this uncertainty is equal to 7.2%.

6.4. B-Tagging

To estimate systematic uncertainties due to the SECVTX b-tagging scale factor between Monte Carlo and data efficiencies, the per-jet tagging probability is varied by $\pm 1\sigma$ (see section 3.1.4.3) and event selection is re-performed. The tagging probabilities for heavy flavor jets and light flavor mistags are varied independently. The migrations of events between the untagged and tagged channels is also accounted for. Only a rate uncertainty is taken for this systematic.

Since the Z+HF rate is normalized to data, this background is not subject to an uncertainty due to the b-tagging scale factor. Therefore, to avoid double counting of systematics, the b-tagging uncertainty is explicitly not applied to Z+HF events. Additionally, since the fake lepton background is derived from data, the b-tagging uncertainty is not applicable to this background either. This uncertainty is taken as correlated between signal, top, and diboson backgrounds.

6.5. Lepton ID/Trigger Efficiencies

Statistical uncertainties on trigger efficiencies and lepton scale factors are taken as systematics. They are converted into uncertainties per each dilepton category, and assumed to be fully correlated between MC based samples. The statistical uncertainties due to these effects are found to be approximately 0.4% for the final event selection. When comparing predicted Z event yield in each dilepton category to data however, it was seen that this was possibly an underestimate of the error. Instead, a sum weighted by each dilepton categories yield in the signal region, over the fractional difference between the predicted and observed number of events for each dilepton category in Z events is used, as determined from table 4.3. The error is then found to be 1.2% due to trigger and lepton ID scale factor errors. It is of note Z+Jets are particularly sensitive to the PDFs used to generate the Monte Carlo events, changing the overall acceptance by up to 6% when NLO PDFs are used, as opposed to the nominal LO PDFs. The use of LO PDF for Z+Jets Monte Carlo may be cause for at least part of this 1.2% discrepancy, but this larger uncertainty is taken in order to be conservative. This uncertainty is not applied to the $Z/\gamma^{\star}$+Jets background since it is normalized using the data, or the fake lepton background since it is data derived.

6.6. Fake Lepton Uncertainty

To estimate the uncertainty on the fake lepton background normalization, the exercise in section 3.2.6.2 of determining the fake rates for the various lepton types is repeated. Instead of using QCD data taken using the JET_50 trigger though, data from JET_20 and JET_70 triggers is used. To estimate the systematic uncertainty on the fake predictions, the fake rate matrix is computed from a sample JET_X and applied to a sample JET_Y. The predicted number of identified leptons is then compared to the actual number of identified leptons in that jet sample, neglecting any real lepton contamination. The results of this exercise can be seen in Fig. 6.2, which also shows the results of using JET_20 and JET_70 instead of JET_50 fake rates to make the prediction of number of jets faking leptons in the signal region.

The largest deviations from this exercise is that fake rates from JET_20 over predict the number of leptons in the JET_70 sample by 18.3%, and that these same JET_20 fake rates predict 21.0% more non-b-tagged signal region events than the nominal JET_50 fake rates; the next largest errors are less than half as large.

Since the fake lepton background uncertainty has little effect on the expected limits, an uncertainty of 30% is taken for this background. This is the value historically taken for similar backgrounds in dilepton analyses, even though the definition of fakeables used in this analysis has been improved relative to others.

Comparison of Different Fake Rates				
Fake Rate Source	Sample Applied To	Predicted	Observed	Relative Error
JET_20	JET_50	9087	7681	+18.3%
JET_70	JET_50	7854	7681	+2.3%
JET_50	JET_20	4653	5116	-9.0%
JET_50	JET_70	1070	1014	+5.6%
Fake Rate Source	Signal Region Data	Predicted	Nominal	Relative Error
JET_20	≥ 1 b-tag	2.7	2.8	-3.5%
JET_20	non-b-tagged	3.4	2.8	+21.0%
JET_70	≥ 1 b-tag	2.9	2.8	+2.0%
JET_70	non-b-tagged	2.9	2.8	+4.1%

TABLE 6.2. The predicted and observed numbers of leptons for the various JET triggered data samples using fake rates derived from other JET samples (top), and the predicted number of jets faking leptons for signal region data using fake rates derived from the JET_20 and JET_70 data samples (bottom). Fake rates derived from the JET_50 data sample are used for the nominal prediction of jets faking leptons in the signal region data.

6.7. Top Mass

The $t\bar{t}$ background is modeled using the world average top mass of 172.5 ± 1.5 GeV [56], for which the corresponding theoretical $t\bar{t}$ cross section is 7.23 pb [50]. Consequently three top mass points are used in this analysis to account for the uncertainty of the top mass: 170, 172.5, and 175 GeV/c^2, where 170 the 175 samples are treated as 1.67σ systematic samples. The reconstructed stop mass templates are created for each of these three samples

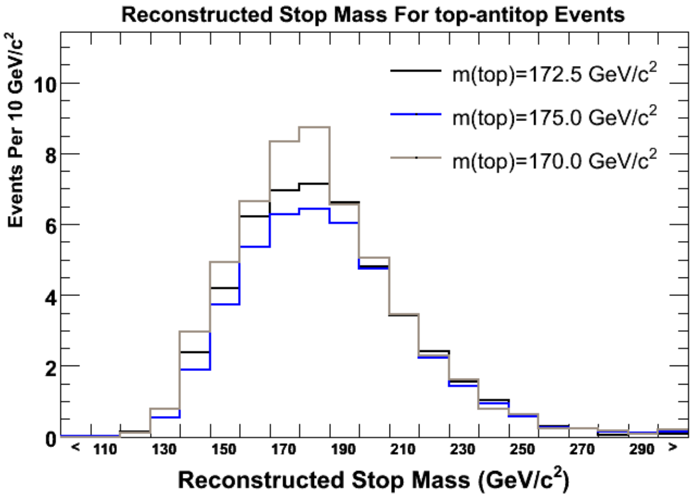

FIGURE 6.2. The reconstructed stop mass for $t\bar{t}$ events at masses of 170 GeV/c^2 (brown), 172.5 GeV/c^2 (black), and 175 GeV/c^2 (blue), for the b-tagged channel using the final event selection cuts. The distributions are normalized to the expected number of events predicted in the b-tagged channel for the respective top mass.

using the relevant theoretical cross sections to determine the normalization. The top mass is then used as a nuisance parameter in the likelihood fit, as well as being randomly chosen according to a Gaussian in the creation of pseudo-data. The template shapes are linearly interpolated corresponding to different top mass points, and normalization accounted for due to acceptance changes and variation of the $t\bar{t}$ cross section. The effect of this systematic can be seen for the reconstructed stop mass in Fig. 6.2.

6.8. Initial/Final State Radiation

Since experimentally in an analysis like this there is little sensitivity to differentiate initial state radiation (ISR) from final state radiation (FSR); stop and $t\bar{t}$ samples were generated with either both ISR and FSR decreased or increased and taken as systematic samples to account for the possible mis-modeling of radiation. This systematic is taken into account as both a rate and shape uncertainty by interpolating stop and top templates, and controlling the amount of ISR/FSR as a nuisance parameter in the likelihood fit and is randomly chosen according to a Gausian distribution for pseudo-experiment generation. The effect of this systematic can be seen in Fig. 6.3.

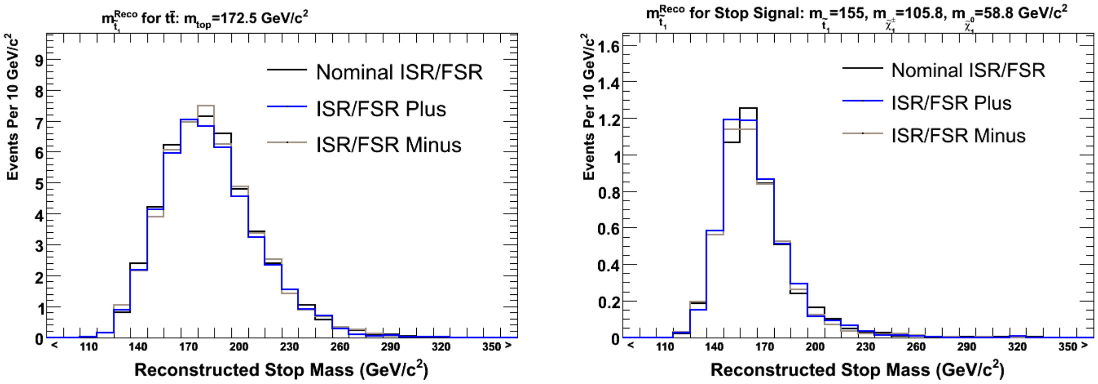

FIGURE 6.3. The effect of initial state radiation (ISR) and final state radiation (FSR) more (brown), and less (blue) for $t\bar{t}$ events (left), and stop events (right) in the b-tagged channel. The histograms are normalized to their respective number of expected events for the final set of analysis cuts. Stop is plotted at a branching ratio of 0.26 for SUSY masses of $m(\tilde{t}_1) = 155$ GeV/c^2, $m(\tilde{\chi}_1^{\pm}) = 105.8$ GeV/c^2, and $m(\tilde{\chi}_1^0) = 58.8$ GeV/c^2.

6.9. Luminosity

The integrated luminosity uncertainty of 5.9% [57] is only applicable to $t\bar{t}$, stop, and diboson sources, and only as a rate uncertainty.

6.10. Theoretical Cross Section

The uncertainty of the NLO theoretical cross section calculations for $t\bar{t}$, stop, and diboson events are applied as rate uncertainties. The uncertainty for combined diboson processes is 10%, and is taken as uncorrelated with any other systematics. The uncertainty in $t\bar{t}$ and stop pair production cross sections can be separated into the uncertainty due to Q^2 scale, and the uncertainty due to parton distribution functions. The Q^2 and PDF errors are each 7% for the $t\bar{t}$ production cross section. For stop production, the uncertainties are larger: 11% due to Q^2, and 14% due to PDFs. The uncertainties due to PDFs are taken as correlated between top and stop, while the uncertainties due to Q^2 are taken as uncorrelated. The Q^2 uncertainty is found by computing the cross section with $Q = 1/2 \times m(t \text{ or } \tilde{t}_1)$, and $Q = 2 \times m(t \text{ or } \tilde{t}_1)$. The PDF uncertainty is found by recomputing the cross section for each of the 41 different sets of PDFs which orthogonally represent the error of the CTEQ6M PDF set [37], and adding these differences in quadrature. More details on the theoretical cross section uncertainty computation can be found in [50].

6.11. Effects of Systematics On Expected Limits

To see the effect each of the systematic uncertainties have on the expected limit, a study was performed that evaluated the expected limits when all but one of the uncertainties were considered. The results can be seen in Fig. 6.4. The largest systematic degrading the sensitivity to excluding stop is the theoretical cross section uncertainty due to PDFs, followed by the theoretical cross section uncertainty of $\tilde{t}_1\bar{\tilde{t}}_1$ events due to the renormalization scale, followed by the jet energy scale.

It should be noted that in Fig. 6.4, removing systematics such as ID/Trigger Efficiency, ISR/FSR, and the Diboson theoretical cross section, actually makes the expected exclusion worse. This is not an indication of anything being amiss. The CLs method used to determine the exclusion confidence levels is a (modified) Frequentist method, and as a result, this worsening of expected limits is a known philosophical difficulty in interpreting the answer in Baysian terms [58]. There is nothing inconsistent, or wrong in terms of Frequintist thinking however.

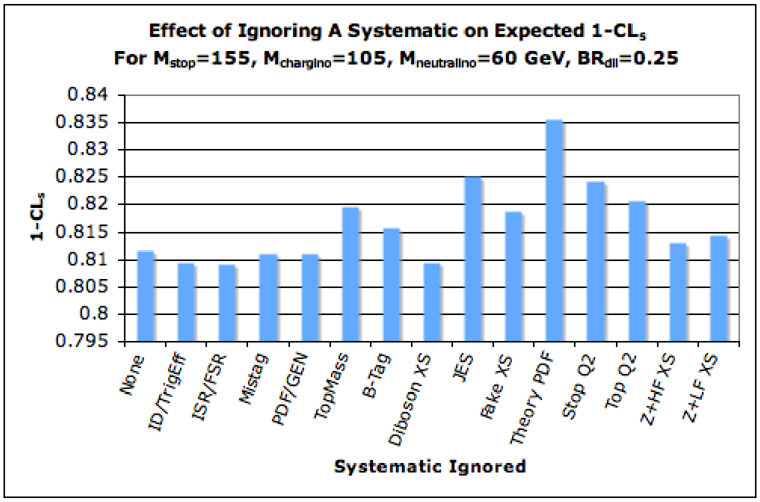

FIGURE 6.4. The effect on the expected exclusion level (1-CL$_S$) when a single systematic uncertainty is removed. The column labeled "None" is with all systematic uncertainties included. Limits are evaluated for a dilepton branching ratio of 0.25 with SUSY masses of $m(\tilde{t}_1) = 155$ GeV/c^2, $m(\tilde{\chi}_1^{\pm}) = 105.8$ GeV/c^2, and $m(\tilde{\chi}_1^0) = 58.8$ GeV/c^2.

CHAPTER 7

Template Morphing

Template *morphing* is the procedure of interpolating the shape of a histogram as a function of one or more parameters. This analysis uses morphing to both account for shape uncertainties as well as create the reconstructed stop mass templates for arbitrary SUSY mass scenarios. There are two basic classes of interpolation algorithms typically used: *horizontal* and *vertical*. Vertical morphing is the more intuitive procedure, and simply involves varying the height of a histograms bins linearly between input histograms. Horizontal morphing involves linearly interpolating between the inverse of the cumulative distribution functions of two or more input histograms, then differentiating the resulting cumulative distribution function in order to obtain the final interpolated histogram. The naming of the procedures will become apparent shortly. Both types of morphing can be extended to handle multiple morphing parameters, treating the parameters as uncorrelated; this is called compound morphing. This analysis extends these procedures, especially horizontal morphing, to take into account correlations among the morphing parameters (hence potentially shape uncertainties), and is referred to as *Grid Morphing*.

7.1. Vertical Morphing

Let histograms $h_A(x)$ and $h_B(x)$ of a physics quantity x correspond to the shapes of the investigated distribution for certain values of a parameter ν: $\nu = \nu_A$ for the histogram $h_A(x)$, and $\nu = \nu_B$ for the histogram $h_B(x)$. We would like to obtain the shape of our distribution for an arbitrary value of ν: $\nu_A < \nu < \nu_B$. In the vertical interpolation technique one subtracts one histogram from the other on bin-by-bin basis: $\Delta h(x) = h_B(x) - h_A(x)$ and obtains the interpolated histogram $h_\nu(x)$ by adding $\Delta h(x)$, re-scaled according to the value of ν, to the histogram $h_A(x)$, such that the interpolated histogram $h_\nu(x)$ is given by:

$$h_\nu(x) = h_A(x) + \frac{\nu - \nu_A}{\nu_B - \nu_A} \times [h_B(x) - h_A(x)] \tag{7.1}$$

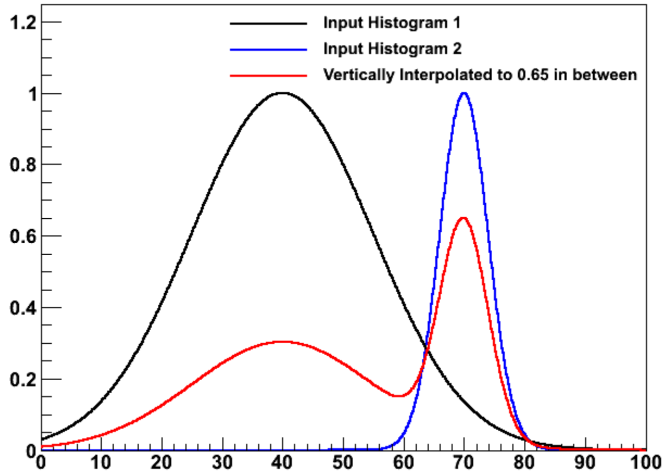

FIGURE 7.1. A simple illustration of vertical template morphing failure; in this case between a Gaussian with a mean of 40 and σ=15, and another Gaussian with mean of 70 and σ=4. If this distribution corresponds something such as an invariant mass, the horizontal morphing procedure in Fig. 7.2 performs in a much more expected manner.

Vertical morphing works well for small shape differences, or distributions where the bins-to-neighboring-bin migration effects are small; however it works rather poorly in distributions such as invariant masses where it is expected that the distribution will move horizontally [59]. An example of when this procedure fails is illustrated in Fig. 7.1, and the equivalent horizontal morphing behaving as desired in Fig. 7.2. This analysis does not use vertical morphing.

7.2. Horizontal Morphing

The horizontal interpolation technique is based off of the interpolation of the inverse of the cumulative distribution function (C.D.F) of the distribution of interest [59]. Although this technique is described below, Fig. 7.2 graphically describes the basic procedure. In the horizontal interpolation technique, one integrates the histograms $h_A(x)$ and $h_B(x)$, to obtain their cumulative distribution functions: $c_A(x)$ and $c_B(x)$:

$$c_{A,B}(x) = \int_{x_{min}}^{x} h_{A,B}(z)dz/N_{A,B}, \tag{7.2}$$

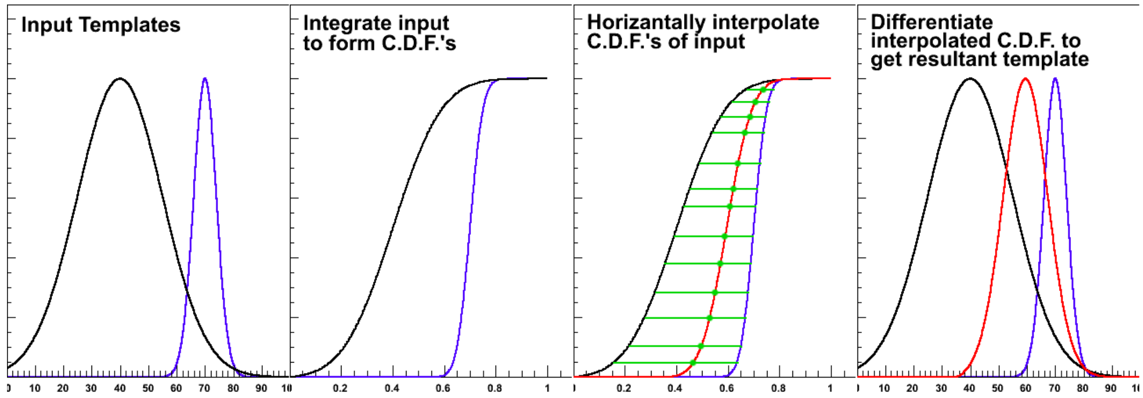

FIGURE 7.2. A simple illustration of how horizontal template morphing is performed; in this case between a Gaussian with a mean of 40 and σ=15, and another Gaussian with mean of 70 and σ=4, to get a resulting Gaussian (the red distribution) with a distance 0.65 between inputs, with mean of 59.5 and σ=7.85. The inputs and distance interpolated are the same as in Fig. 7.1.

where

$$N_{A,B} = \int_{x_{min}}^{x_{max}} h_{A,B}(z)dz \tag{7.3}$$

are the total integrals of the histograms $h_A(x)$ and $h_B(x)$ over the area of interest. Then the inverse of the interpolated C.D.F $c_\nu^{-1}(y)$ is determined by:

$$c_\nu^{-1}(y) = c_A^{-1}(y) + \frac{\nu - \nu_A}{\nu_B - \nu_A} \times [c_B^{-1}(y) - c_A^{-1}(y)] \tag{7.4}$$

The interpolated histogram is found by taking the derivative of $c_\nu(x)$: $h_\nu(x) = c'_\nu(x) \times N_\nu$, where N_ν is the normalization factor that is also linearly interpolated based on values of N_A and N_B given by Equation 7.3:

$$N_\nu = \frac{N_A \cdot (\nu_B - \nu) + N_B \cdot (\nu - \nu_A)}{\nu_B - \nu_A}, \tag{7.5}$$

This technique works fairly well for interpolation of histograms, although it does not guarantee the accuracy of extrapolation. It should also be noted that using this procedure properly maintains the statistical uncertainties of each bin in the resulting histogram if the input histograms are filled using unweighted events.

7.3. Compound Morphing

If it is necessary to vary the template with two or more parameters, morphing can be extended to compound the effects of multiple parameters. When the morphing techniques are applied for evaluating the shape distortions due to systematic effects, we usually know the nominal shape $h_0(x)$, and shifted shapes $h_{1,\pm}(x), h_{2,\pm}(x), ...$, corresponding to floating the respective parameter $\nu_1, \nu_2, ...$, according to its $\pm 1\sigma$ (or more than one σ) uncertainty.

In the compound template morphing technique [60], the interpolation is done for each parameter ν_i individually, then the sum of differences due to variations of each parameter is added to the nominal shape:

$$\begin{aligned} c^{-1}(y) = c_0^{-1}(y) + \textstyle\sum_i max(\nu_i, 0)[c_{i,+}^{-1}(y) - c_0^{-1}(y)] \\ - \textstyle\sum_i min(\nu_i, 0)[c_{i,-}^{-1}(y) - c_0^{-1}(y)], \end{aligned} \tag{7.6}$$

where $c_{i,\pm}^{-1}(y)$ are the inverse C.D.F. for values $\nu_i = \pm 1; \nu_j \equiv 0, j \neq i$. To state another way, the change in the inverse C.D.F. due to each morphing is added to the nominal inverse C.D.F. to determine the final inverse C.D.F. which is then inverted and differentiated to obtain the final template. This procedure works well for accounting for multiple shape uncertainties, as long as they are uncorrelated. This procedure was used to handle the multiple shape systematics in this analysis.

7.4. Grid Morphing

Unfortunately, using Compound Morphing with two or more parameters simultaneously is an extrapolation, which by construction is not prompted to give the correct, or expected results.

In order to merely make use of the interpolation and avoid the extrapolation completely, additional shapes corresponding to floating two or more systematics parameters simultaneously are needed as input. For instance if there are two parameters ν_1 and ν_2, and the shape corresponding to $(\nu_1, \nu_2) = (a, b); a > 0, b > 0$ needs to be obtained. Grid Morphing makes use of 4 different input templates corresponding to points $(0, 0)$ - nominal, $(0, +1), (+1, 0)$

and $(+1,+1)$. First, the shapes $(0,0)$ and $(+1,0)$ are interpolated to obtain $(a,0)$:

$$c^{-1}_{(a,0)}(y) = c^{-1}_{(0,0)}(y) + a \cdot [c^{-1}_{(+1,0)}(y) - c^{-1}_{(0,0)}(y)]. \tag{7.7}$$

Next, the same exercise with the $(0,+1)$ and $(+1,+1)$ templates is performed to obtain $(a,+1)$:

$$c^{-1}_{(a,+1)}(y) = c^{-1}_{(0,+1)}(y) + a \cdot [c^{-1}_{(+1,+1)}(y) - c^{-1}_{(0,+1)}(y)]. \tag{7.8}$$

Finally, the templates $(a,0)$ and $(a,+1)$ are morphed to obtain (a,b):

$$c^{-1}_{(a,b)}(y) = c^{-1}_{(a,0)}(y) + b \cdot [c^{-1}_{(a,+1)}(y) - c^{-1}_{(a,0)}(y)]. \tag{7.9}$$

This algorithm is illustrated in Fig. 7.4. In this paper this algorithm is referred to as Grid Morphing, since one requires an N-dimensional grid of various systematic parameter points to interpolate between them. This technique can be used for an arbitrary number of morphing parameters; however the number of input templates goes as 2^N, where N is the number of morphing parameters. This algorithm was originally developed to account for the shape correlations in systematic uncertainties (particularly the JES and top mass). Compound morphing was found to be sufficient for this analysis though, and greatly decreased computation time so was used instead. This algorithm did however prove to be *very* useful for setting smooth limits in the plains of $\tilde{t}_1$ and $\tilde{\chi}^0_1$ by providing a way to obtain the reconstructed stop mass distribution for an arbitrary set of SUSY masses and systematic uncertainties from the finite number of SUSY masses which could be simulated due to the high computational cost of simulating events. The ability to do so allowed the setting of smooth confidence limits, making the results of this analysis easy to interpret, as opposed to only setting limits for a finite number of unconnected SUSY mass points.

To obtain the reconstructed stop mass for input into the limits, this Grid Morphing was performed in the following dimensions: $\tilde{t}_1$, $\tilde{\chi}^0_1$, JES, and ISR/FSR, for the various $\tilde{\chi}^\pm_1$ masses. It was verified that using Grid Morphing accurately interpolates the reconstructed stop mass between generated Monte Carlo samples. This was done by comparing the reconstructed stop mass templates made directly from a Monte Carlo sample, to a template made by

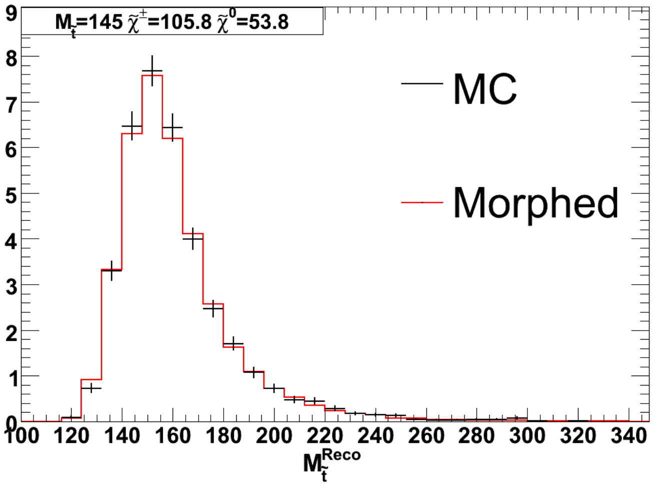

FIGURE 7.3. A check that Grid Morphing could be used to accurately make the reconstructed stop mass template for an arbitrary set of SUSY masses. The black histogram with error bars is the result of stop mass reconstruction on Monte Carlo, while the red histogram has been interpolated from other Monte Carlo samples with SUSY masses ($m_{\tilde{t}_1}$, $m_{\tilde{\chi}_1^{\pm}}$, $m_{\tilde{\chi}_1^0}$): (155, 105.8, 58.8), (135, 105.8, 58.8), (135, 105.8, 43.9), and (155, 105.8, 43.9).

interpolating from other Monte Carlo samples, the results are demonstrated in Fig. 7.3. The results of morphing in the stop and neutralino directions can be seen in Fig. 7.5.

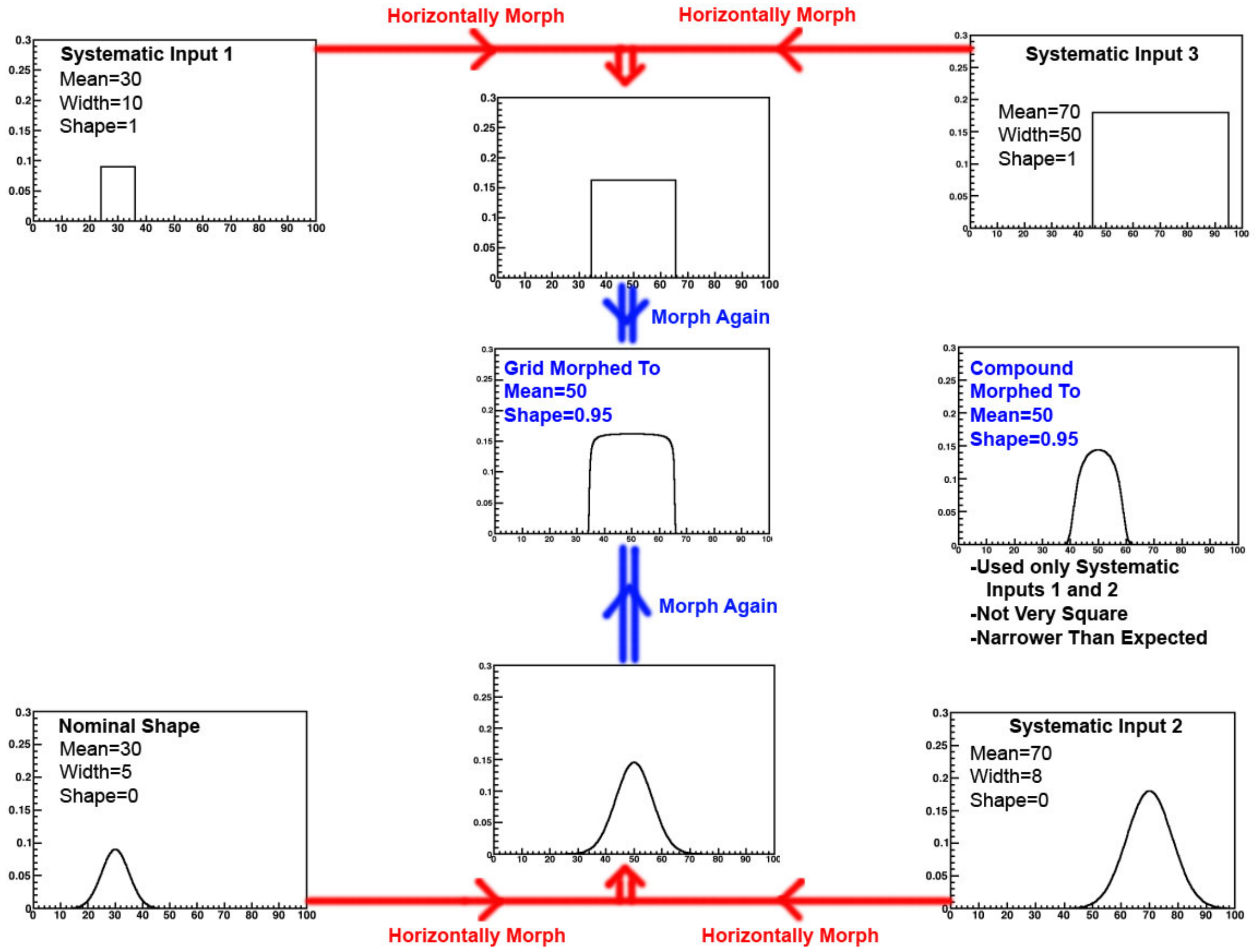

FIGURE 7.4. Illustration of the Grid Morphing Algorithm in two dimensions. As a comparison, also shown is the result from the compound morphing algorithm that ignores the systematic input 3 by construction, thus given an undesirable results.

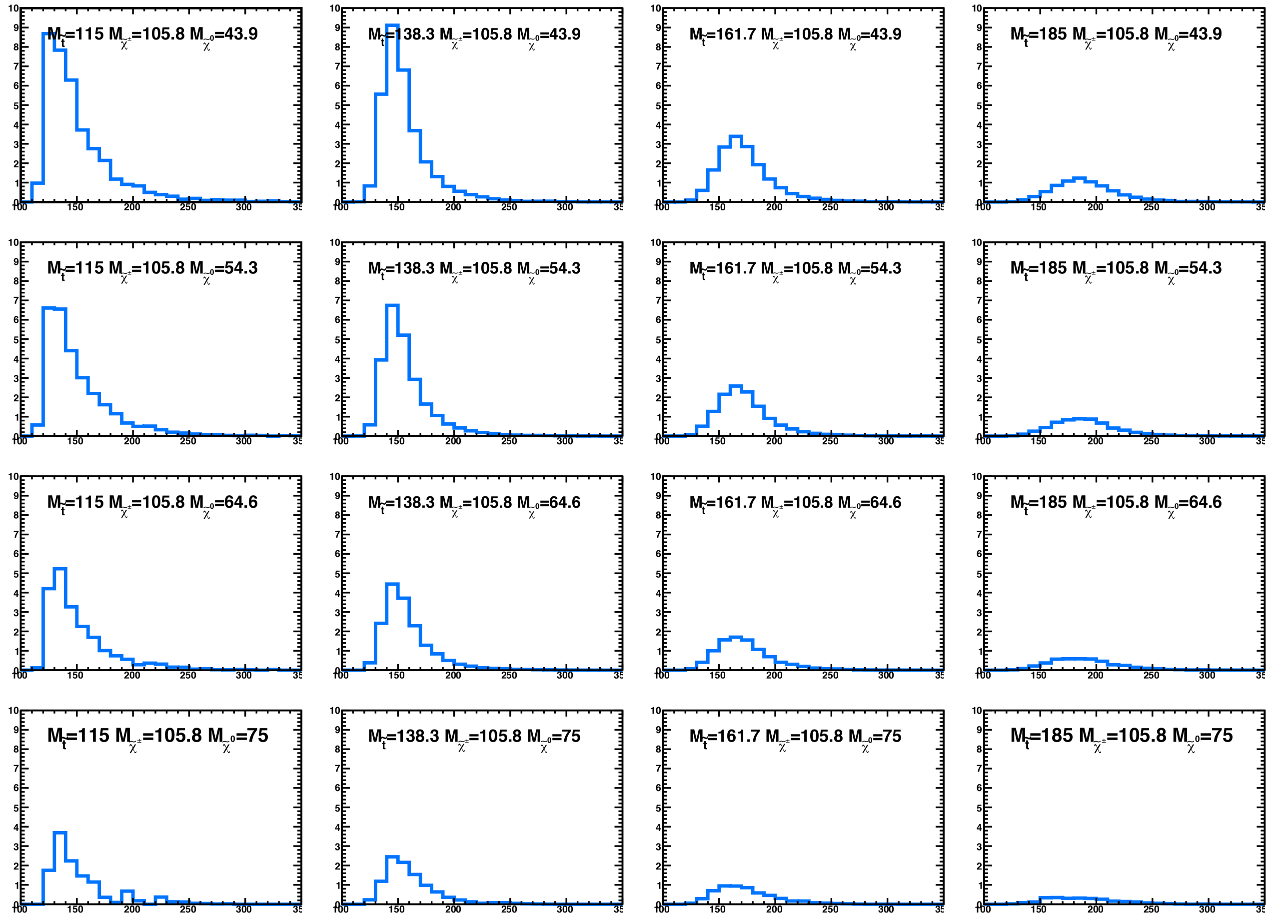

FIGURE 7.5. How the reconstructed stop mass "morphs" as a function of stop mass, and neutralino mass, for $m_{\tilde{\chi}_1^{\pm}} = 105.8\ \mathrm{GeV}/c^2$, and a subrange of $m_{\tilde{t}_1}$ and $m_{\tilde{\chi}_1^0}$ used in this analysis. Masses labeled on the plot are in units of GeV/c^2, and the 'x' axis is the reconstructed stop mass (GeV/c^2). The normalization of histograms corresponds to expected number of events for the respective SUSY mass point, in the b-tagged channel at a fixed branching ratio.

CHAPTER 8

Confidence Level Calculation

The Modified Frequentist procedure, $\mathrm{CL_S}$ [61][62], is used to determine the exclusion confidence level (CL) of signal. The $\mathrm{CL_S}$ procedure was originally developed at the LEP experiments to be used in the exclusion of the Higgs boson. $\mathrm{CL_S}$ is based on the test statistic, $Q = {}^{\mathcal{L}(s+b)}/_{\mathcal{L}(b)}$[1], which is the ratio of the signal plus background likelihood to the background only likelihood, given the observed data sample. It can be shown Q is an optimal choice of test statistic [63], and is at the heart of the $\mathrm{CL_S}$ procedure. This chapter describes the $\mathrm{CL_S}$ procedure, as well the specifics of how it is used in this paper.

This analysis was performed two times, once with 1.9 fb^{-1} of observed data, and then updated to include 2.7 fb^{-1} of observed data. For the original 1.9 fb^{-1} analysis, exclusions were computed using computer code written by the author to implement the procedures described in this chapter. For the 2.7 fb^{-1} analysis, the MCLIMIT [60] program was used to compute limits, due to it being more computationally efficient. Both codes used the principles described in this chapter, and produced the same results. The MCLIMIT program is widely used within the CDF experiment, as well as a number of other experiments, for the computation of limits; it contains many features not described here, including a Bayesian limit calculation routine.

8.1. The $\mathrm{CL_S}$ Procedure

8.1.1. Basics of the $\mathrm{CL_S}$ Procedure. In this analysis, binned histograms are used to represent the distributions of reconstructed stop mass for both Monte Carlo simulations and the observed data sample. Two orthogonal channels are used to perform this search: the b-tagged and not-b-tagged channels. This increases sensitivity due to fact that two channels have different signal to background ratios.

---

[1] More generally Q can be described as the ratio of the likelihood of the test hypothesis to the likelihood of the null hypothesis.

Ignoring systematic uncertainties for the moment, the test statistic for this analysis is given by:

$$Q \equiv \mathcal{L}(data|s+b)/\,\mathcal{L}(data|b) = \prod_{c}\prod_{i} \frac{e^{-(s_{i,c}+b_{i,c})}\,(s_{i,c}+b_{i,c})^{d_{i,c}}}{d_{i,c}!} \bigg/ \frac{e^{-b_{i,c}} b_{i,c}^{d_{i,c}}}{d_{i,c}!}\ , \tag{8.1}$$

where the products are over the b-tagged and not-b-tagged channels c, and over bins i of the histograms. The symbols $s_{i,c}$, $b_{i,c}$, and $d_{i,c}$ indicate the bin contents of the i^{th} bin in the c^{th} channel for the sum of signal plus backgrounds, sum of backgrounds, and the observed data sample histograms respectively; the $d_{i,c}!$ cancel out in this equation, but were left in to emphasize that these are Poisson likelihoods. Large values of Q can be thought of as the observed data looking more like the signal+background hypothesis, than the background only hypothesis.

The definition of the test statistic in equation 8.1 turns out to be inconvenient to work with for numerical stability reasons, so it is worthwhile to redefine the test statistic in a more convenient form, $-2\ln Q$. The equivalent of equation 8.1 is then:

$$-2\ln Q = -2\ln\left(\mathcal{L}(s+b)\right) + 2\ln\left(\mathcal{L}(b)\right) = \sum_{c}\sum_{i} 2s_{i,c} + 2d_{i,c}\ln\left(\frac{b_{i,c}}{s_{i,c}+b_{i,c}}\right), \tag{8.2}$$

where again the sum over c is analysis channels, and the sum over i is histogram bins. The quantity $-2\ln Q$ is not only more numerically tractable but can also be interpreted as a difference of χ^2 between the two hypotheses, thus giving some intuitive meaning to this quantity [61]. The remainder of this chapter will refer to $-2\ln Q$ as the test statistic.

The quantity to use to compute the confidence level for excluding the presence of signal plus background is then:

$$\mathrm{CL_{s+b}} \equiv \mathrm{P_{s+b}}\left(-2\ln Q \geq -2\ln Q_{\mathrm{obs}}\right), \tag{8.3}$$

where this is the probability that, assuming the presence of signal and background at the hypothesized levels, the test statistic $-2\ln Q$ would be greater than or equal to the observed test statistic for a large ensemble of identical experiments[2]. If a value of $\mathrm{CL_{s+b}} = 0.05$ was observed, then the test hypothesis would be excluded at the 95% level. This probability may be analytically computed in the case of a small number of bins and channels without

---

[2] Or to put it another way, $\mathrm{CL_{s+b}}$ is the the probability that the signal+background hypothesis would fluctuate down look as much like the background only hypothesis as the observed data.

systematic uncertainties; the computation for a more realistic case will be discussed shortly. Similarly, a quantity may be defined for the confidence level of the presence of background only:

$$1 - \mathrm{CL_b} \equiv \mathrm{P_b}\left(-2\ln Q \leq -2\ln Q_\mathrm{obs}\right), \tag{8.4}$$

where this is the probability that assuming the presence of the background only, one would observe a result that looks at least as signal like as the one observed. This is the quantity typically used to quantify the confidence level of a discovery; for a five sigma discovery, this quantity is required to be less than 2.8×10^{-7} or 5.7×10^{-7}, depending on whether a one-sided or two-sided exclusion is desired.

The Modified Frequentist confidence level, CL$_\mathrm{S}$, which is used in this analysis to determine exclusion confidence levels, is defined as:

(8.5)

$$\mathrm{CL_S} \equiv \mathrm{CL_{s+b}} \Big/ \mathrm{CL_b} = \mathrm{P_{s+b}}\left(-2\ln Q \geq -2\ln Q_\mathrm{obs}\right) \Big/ \mathrm{P_b}\left(-2\ln Q \geq -2\ln Q_\mathrm{obs}\right)$$

As will be seen shortly, using this quantity to find the exclusion confidence level, CL $= 1 - \mathrm{CL_S}$, has the benefit of preventing the exclusion of signal which the experiment has no sensitivity to; the use of CL$_\mathrm{s+b}$ to place 95% CL limits on signal which the experiment has no sensitivity to would allow ruling out the hypothesized signal 5% of the time, when it is clear the experiment should not be placing limits on such a signal.

8.1.2. PDFs of $-2\ln Q$, and Incorporating Systematics.

The previous section did not address two important concerns: how to calculate $\mathrm{P_{s+b}}\left(-2\ln Q \geq -2\ln Q_\mathrm{obs}\right)$ and $\mathrm{P_b}\left(-2\ln Q \geq -2\ln Q_\mathrm{obs}\right)$, or how to include the effects of systematic uncertainties.

Although $\mathrm{P_{s+b}}\left(-2\ln Q \geq -2\ln Q_\mathrm{obs}\right)$ and $\mathrm{P_b}\left(-2\ln Q \geq -2\ln Q_\mathrm{obs}\right)$ can be computed analytically for simple scenarios[3], in a realistic experiment the *probability distribution function* (PDFs) of $-2\ln Q$ must be determined for the signal plus background (test) and background only (null) hypotheses. These PDFs can be most easily constructed using a large number of pseudo-experiments (PEs). The purpose of a PE is to create a random potential outcome that could be observed by an experiment, assuming a given hypothesis

---

[3] In the case of a single channel and single bin, $\mathrm{P}\left(-2\ln Q \geq -2\ln Q_\mathrm{obs}\right)$ is the probability the given hypothesis would yield less than or equal to the number of events in the observed data sample.

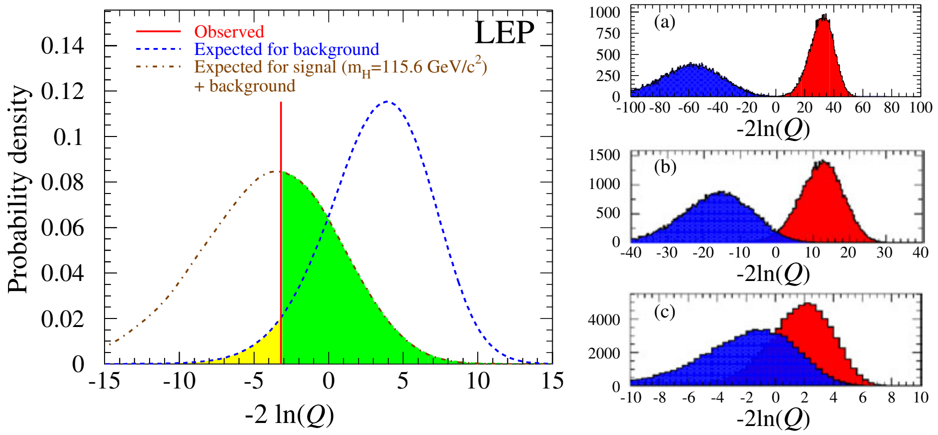

FIGURE 8.1. Example distributions of $-2\ln Q$ for a Higgs boson search at the LEP experiments. Left: The dashed blue distribution is the PDF for the background only hypothesis, while the dashed brown distribution is for signal + background hypothesis. The yellow region to the left of the observed value of $-2\ln Q$ is 1-CL$_\mathrm{b}$; the green region to the right of the observation is CL$_\mathrm{s+b}$. Right: Illustration of the evolution of the PDFs with declining sensitivity from (a) to (c) as the Higgs mass is increased and it's cross section falls. Figures from reference [62].

was correct; this resulting output of simulated data is called pseudo-data. For the case of this analysis, the observed data sample is a random Poisson process for each bin, so the pseudo-data histograms are created by:

$$h^{b}_{i,c} = \mathrm{rand}_P\left(b_{i,c}\right), \tag{8.6}$$

$$h^{s+b}_{i,c} = \mathrm{rand}_P\left(s_{i,c} + b_{i,c}\right), \tag{8.7}$$

where $\mathrm{rand}_P\left(\lambda\right)$ is a random Poisson number generated with a mean of λ, resulting in an integer N distributed according to the probability $e^{-\lambda}\lambda^N/N!$.

The test statistics $-2\ln Q$ can then be found for a large number of PEs[4], in order to form the PDFs of $-2\ln Q$ for both the test and null hypotheses, using $h^{s+b}_{i,c}$ and $h^{b}_{i,c}$ in place of $d_{i,c}$ of equation 8.1, for the test and null hypothesis PDFs respectively. Example PDFs of $-2\ln\left(Q\right)$ for the LEP Higgs search are displayed in Fig. 8.1.2.

Systematic uncertainties are handled in the CL$_\mathrm{S}$ procedure when creating the psuedo-data samples in equations 8.6 and 8.7. Instead of using the sum of the nominal background

---

[4] To be clear, for each pseudo-experiment, a new randomly generated pseudo-data sample is created, and hence a new value of $-2\ln Q$.

and signal histograms to determine $s_{i,c}$ and $b_{i,c}$, the nuisance parameters (e.g. the systematic uncertainties one doesn't desire to measure) are fluctuated randomly according to a unit width Gaussian distribution. The effects of the fluctuated nuisance parameters are propagated onto $s_{i,c}$ and $b_{i,c}$ (see section 8.1.3, specifically equation 8.11, for exactly how this is done). In this manner, both rate and shape systematics will change $s_{i,c}$ and $b_{i,c}$, thus the pseudo-data samples will be created with altered mean values in each bin. The systematics are re-fluctuated, and pseudo-data sample is regenerated for each pseudo experiment. The affect of varying the systematic uncertainties while creating PEs has the resulting effect of broadening and creating larger overlap between the PDFs of $-2\ln Q$, thus reducing the sensitivity to signal, as can be seen in Fig. 8.1.2. This process of making the CL_S quantity not depend on the systematic uncertainties is referred to as *marginalization*; the Bayesian equivalent of this process is to integrate the probability of each outcome over all nuisance parameters, weighted by the priors for the nuisances parameters.

Some of the sensitivity loss due to systematic uncertainties can be recovered, however, by using the observed data sample (or in the case of PEs, the pseudo-data sample) to further constrain the nuisance parameters. This is done by extending the likelihoods in equation 8.1 to include the nuisance parameters, and maximizing the likelihoods with respect to these parameters for the given observed data (or pseudo-data)[5].

For systematic uncertainties $\theta_j \in \vec{\theta}$, the likelihoods become:

$$-2\ln\left(\mathcal{L}(\vec{\theta},\text{data}|\text{b})\right) = 2b_{i,c}(\vec{\theta}) - 2d_{i,c}\ln(b_{i,c}(\vec{\theta})) + 2\ln(d_{i,c}!) + \sum_j \theta_j^2 \tag{8.8}$$

$$-2\ln\left(\mathcal{L}(\vec{\theta},\text{data}|\text{s+b})\right) = 2s_{i,c}(\vec{\theta}) + 2b_{i,c}(\vec{\theta}) - 2d_{i,c}\ln(s_{i,c}(\vec{\theta}) + b_{i,c}(\vec{\theta})) + 2\ln(d_{i,c}!) + \sum_j \theta_j^2, \tag{8.9}$$

where now background and signal predictions for each bin become explicit functions of the nuisance parameter, and the value squared of each of the nuisance parameters is added to $-2\ln(\mathcal{L})$. The $-2\ln(\mathcal{L})$ in 8.8 and 8.9 is then separately minimized (equivalently the likelihoods are maximized) to the given observed data (or pseudo-data) using the MINUIT

---

[5] This is often referred to as a *profile* likelihood method.

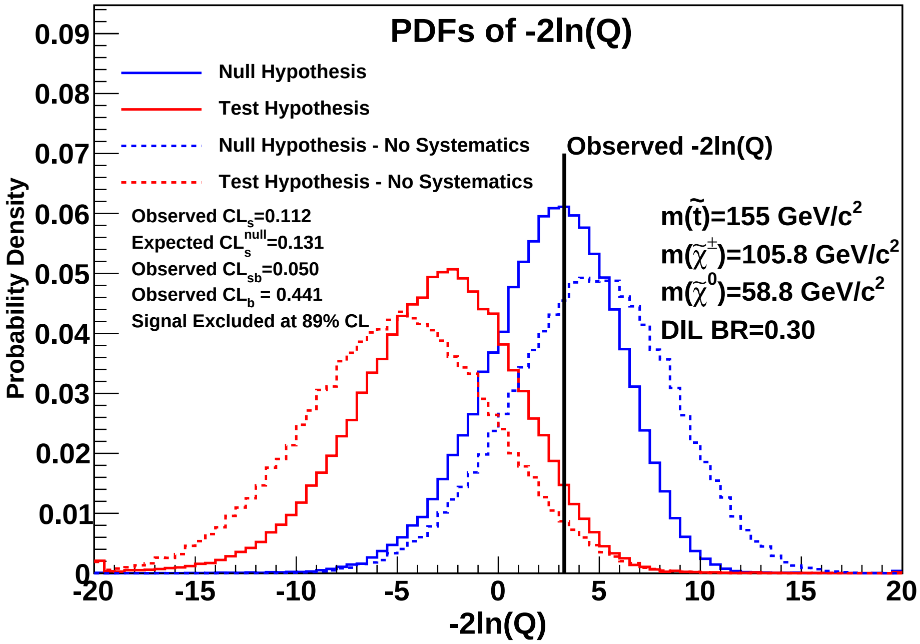

FIGURE 8.2. Example PDFs of $-2\ln Q$ for a SUSY mass scenario of $m(\tilde{t}_1) = 155$ GeV$/c^2$, $m(\tilde{\chi}_1^{\pm}) = 105.8$ GeV$/c^2$, and $m(\tilde{\chi}_1^0) = 58.8$ GeV$/c^2$; at a dilepton branching ratio of 0.3. It can be seen rhat the observed $-2\ln Q$ is very near what is expected under the background only hypothesis. The dashed distributions correspond to systematic uncertainties not being considered. The degradation of sensitivity due to systematic uncertainties can be seen by the increased overlap of the PDFs which are made considering systematics.

[55] minimization package. The test statistic used for this analysis in its final form is then:

$$-2\ln(Q) = 2\ln\left(\mathcal{L}(\text{data}|\text{b};\vec{\theta})\right) - 2\ln\left(\mathcal{L}(\text{data}|\text{s+b};\vec{\theta}')\right) \tag{8.10}$$

Where these $-2\ln(\mathcal{L})$'s are separately minimized with respect to the nuisance parameters (e.g. $\vec{\theta}$ and $\vec{\theta}'$ are different). An example distribution of the PDFs of $-2\ln(Q)$ for the signal plus background and background only hypothesis, as well as the observed data test statistic, for this analysis can be seen in Fig. 8.1.2.

8.1.3. Details of Handling Systematic Uncertainties. The previous section showed how systematic uncertainties are incorporated into the likelihoods, and how they are accounted for in reducing the sensitivity to signal, but it did not explicitly explain how $s_{i,c}(\vec{\theta})$ and $b_{i,c}(\vec{\theta})$ are calculated.

From Chapter 6, it can be seen that rate systematics are quoted as a fractional uncertainty corresponding to a "1σ" uncertainty and may potentially be asymmetric. Additionally, shape systematics will change the predicted amount of events on a bin-by-bin basis, the shape systematics are accounted for using compound morphing as described in section 7.3. The histograms used below to determine bin contents are assumed to have already been morphed according to the relevant set of nuisance parameters, $\vec{\theta}$.

The application of rate uncertainties for a given bin (i), channel (c), and physics source (k) is performed by:

$$r^{varied}_{i,c,k} = r^{central}_{i,c,k} \prod_j \left(1 + \theta_j \frac{f^+_{k,j} - f^-_{k,j}}{2} + \theta_j^2 \frac{f^+_{k,j} + f^-_{k,j}}{2}\right) \tag{8.11}$$

Where $f^+_{k,j}$ ($f^-_{k,j}$) indicates the fractional uncertainty for a *positive* (*negative*) 1σ shift of the j^{th} nuisance parameter of the k^{th} physics source. For the case of a symmetric uncertainty, the θ_j^2 term drops out. For asymmetric uncertainties, the linear plus quadratic dependence on θ_j ensures the uncertainty is treated asymmetrically while avoiding a discontinuity across the $\theta_j^2 = 0$ boundary. Such a discontinuity could cause a jump in the likelihood causing MINUIT to return an unexpected result. To be explicit, $b_{i,c}(\vec{\theta})$ and $s_{i,c}(\vec{\theta})$ are:

$$b_{i,c}(\vec{\theta}) = \sum_k \left[r^{central}_{i,c,k} \prod_j \left(1 + \theta_j \frac{f^+_{k,j} - f^-_{k,j}}{2} + \theta_j^2 \frac{f^+_{k,j} + f^-_{k,j}}{2}\right)\right], \tag{8.12}$$

$$s_{i,c}(\vec{\theta}) = r^{central}_{i,c,k=s} \prod_j \left(1 + \theta_j \frac{f^+_{k=s,j} - f^-_{k=s,j}}{2} + \theta_j^2 \frac{f^+_{k=s,j} + f^-_{k=s,j}}{2}\right), \tag{8.13}$$

where the product is over the nuisance parameters j, and sum for $b_{i,c}(\vec{\theta})$ over the physics sources k. $k = s$

8.2. Finding Expected Test Statistics and Limits

It is useful to evaluate the *expected* test statistic under either the background only (null), or signal plus background (test) hypothesis in order to determine the expected $\mathrm{CL_S}$, $\mathrm{CL_b}$, or $\mathrm{CL_{s+b}}$. There are two ways of determining the expected $-2\ln Q$ for each of the hypotheses: use the mean or the median of the respective PDF.

This analysis uses the median test statistic to determine expected sensitivity. The reasoning for this is twofold. First, the median test statistic is the value one would expect half of experiments to outperform or underperform. Second, the median test statistic is invariant to a change of parameters. For instance, if an expected limit is placed on a parameter σ which is dependent on the square of another parameter θ^2, then the expected limit can easily be transformed to an expected limit on θ. This wouldn't be the case if the mean $-2\ln Q$ was used. This analysis was optimized using the expected $\mathrm{CL_S}$, which is the $\mathrm{CL_S}$ computed using the median test statistic in the null hpothesis.

CHAPTER 9

Event Selection Optimization

As mentioned in Chapter 4, a novel features of this analysis is optimizing the event selection cuts based on all systematic uncertainties, in order to maximize expected sensitivity to exclusion of signal. This was accomplished by creating software that, for an arbitrary set of event selection cuts[1]: estimate signal and background normalizations (Chapter 4), create the corresponding reconstructed stop mass distribution (Chapter 5), calculate systematic uncertainties (Chapter 6), find the expected exclusion CL to signal under the background only hypothesis (Chapter 8). This software was then interfaced to a Genetic optimization library [64], which then helped chose optimal event selection cuts.

9.1. Pre-Selection

A number of minimum event selection cuts were imposed in order to ensure accurate modeling of the physics, as verified in a very broad dilepton control region (places were no signal is expected) analysis.

Cosmic Veto: Since cosmic muons may be present in the observed data sample, a veto is applied to $\mu\mu$ events to remove events out of time with bunch crossings or with track impact parameter not consistent with the interaction region.

Conversion Veto: Events found to have an electron conversion are vetoed.

Opposite Lepton Charge: Since two opposite sign leptons are expected for signal, this requirement is imposed.

Lepton Types: One lepton is required to be a tight central lepton (CEM, CMUP, or CMX), while the second lepton can be a looser lepton: (NI)CEM, PHX, (NI)CMU, (NI)CMP, (NI)CMUP, (NI)CMX, or a minimum ionizing particle-CMIO. Where (NI) denotes the possibility of that lepton type being non-isolated. If the second lepton is a PHX, then the tight central lepton may be non-isolated.

---

[1] Not completely arbitrary, but event selection cuts within the very broad phase space of the dilepton analysis region which was found could be accurately modeled.

Lepton Mass : The leptons must have an invariant mass above 20 GeV/c^2, and be separated by $\sqrt{\Delta\phi^2 + \Delta\eta^2} > 0.4$, in order to avoid potential mis-modelings.

$\not{E}_T$: The event must have $\not{E}_T > 20$ GeV since less than this was considered a control region, due to very little signal expected in this region.

Z-Veto: ee and $\mu\mu$ events within the invariant mass range of $76 < m_{\ell\ell} < 106$ GeV/c^2 are required to pass a veto of Met Significance $\equiv \frac{\not{E}_T}{\sqrt{\sum E_T}} > 4$ GeV. These values were not considered for optimization.

Second Jet E_T: The second jet in the event must have a corrected E_T of at least 12 GeV; this was the lowest E_T validated in the control regions.

9.2. Control Region Modeling Validation

An extensive validation of control regions where little to no signal was expected was performed in order to ensure sufficient physics modeling for this analysis. During the validation, many kinematic quantities and normalization predictions were checked for nearly every distinct applicable region of physics modeling of interest. Kinematics and yields were checked for various combinations of: b-tagg requirements, combinations of types of leptons in the event, different regions of $\not{E}_T$, with and without the Met Significance Z-veto, different combinations of lepton isolations, different jet bins, and so on. Presented here is a summary of the control regions.

- Various kinematics of pre-tag low $\not{E}_T$ events with 1 jet are presented in Fig. 9.1.
- Various kinematics of pre-tag low $\not{E}_T$ events with ≥2 jets are displayed in Fig. 9.2.
- The scalar sum of transverse momentums in low $\not{E}_T$ events with ≥2 jets, Fig. 9.3.
- The lead jet E_T in pre-tag low $\not{E}_T$ events with 1 jet is shown in Fig. 9.4.
- Pre-tag same-sign electron-muon events with one jet is presented in Fig. 9.5, and shows accurate modeling of the fake lepton background.
- The kinematics of pre-tag high $\not{E}_T$ events with one jet is shown in Fig. 9.6.
- The kinematics of pre-tag high $\not{E}_T$ events with ≥2 jets is shown in Fig. 9.7
- The event kinematics of b-tagged ≥2 jet events with low $\not{E}_T$ is shown in Fig. 9.8.
- The scalar sum of transverse momentums of b-tagged ≥2 jet events with low $\not{E}_T$ is shown in Fig. 9.9.

From these plots it can be seen both the yields and kinematics of events are well modeled.

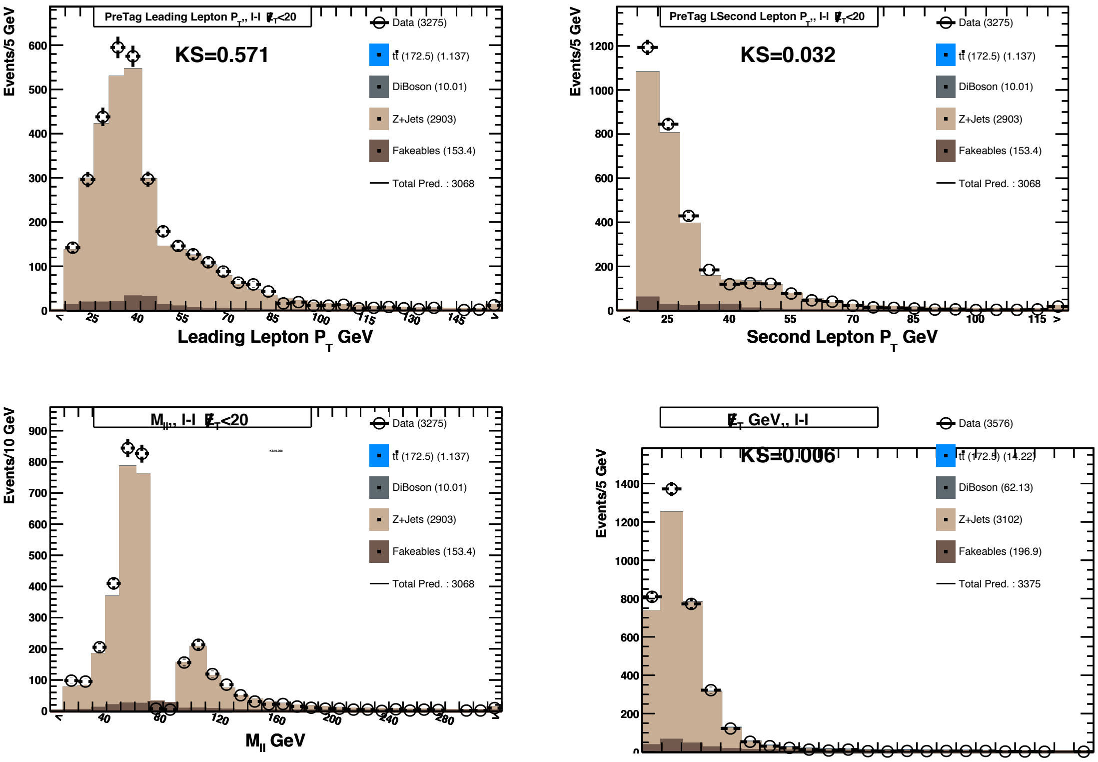

FIGURE 9.1. Kinematics of pre-tag, opposite-sign events with $\not\!\!E_T < 20$ GeV, exactly 1 jet, and Met Significance > 4 GeV for *ee* and $\mu\mu$ with invariant mass of 76 GeV/c^2 $< m_{\ell\ell} <$ 106 GeV/c^2.

9.3. Genetic Algorithm

Genetic algorithms have been used to solve a wide range of difficult problems, ranging from improving jet engine designs [65] to routing telecommunication networks [66] to building electronics requiring the minimum number of components[2] [67]. In this analysis, a Genetic algorithm is used to search the large phase space of event selection cuts in order to find an optimal set to maximize expected exclusion of signal.

Genetic algorithms use a *population* of abstract representations (*chromosomes*) of potential solutions (*individuals*) which, through biological reproduction, evolve toward an optimal solution to the problem at hand. Starting from a large population of individuals with randomly chosen chromosomes, each individual is evaluated for their fitness for survival. The poorly performing individuals are discarded, and the survivors allowed to reproduce.

---

[2] sometimes producing circuits which baffle researches as to how they even work

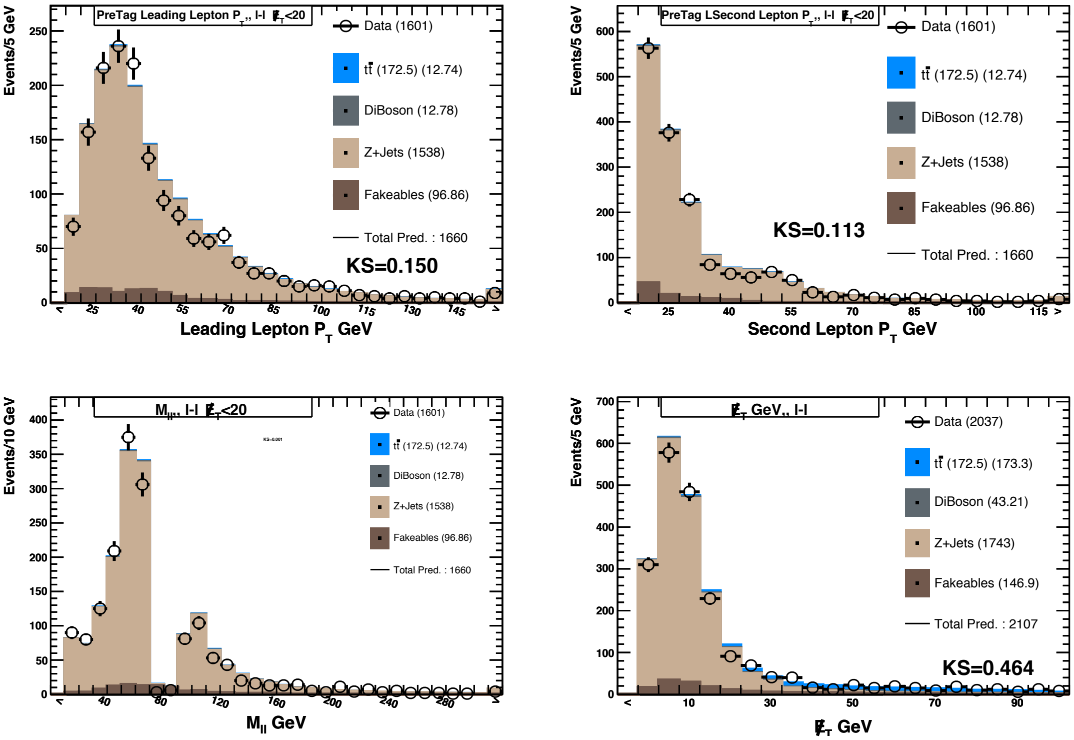

FIGURE 9.2. Kinematics of pre-tag, opposite-sign events with $\not{E}_T < 20$ GeV, ≥ 2 jets, and Met Significance > 4 GeV for ee and $\mu\mu$ events with invariant mass of 76 GeV/$c^2 < m_{\ell\ell} < 106$ GeV/c^2.

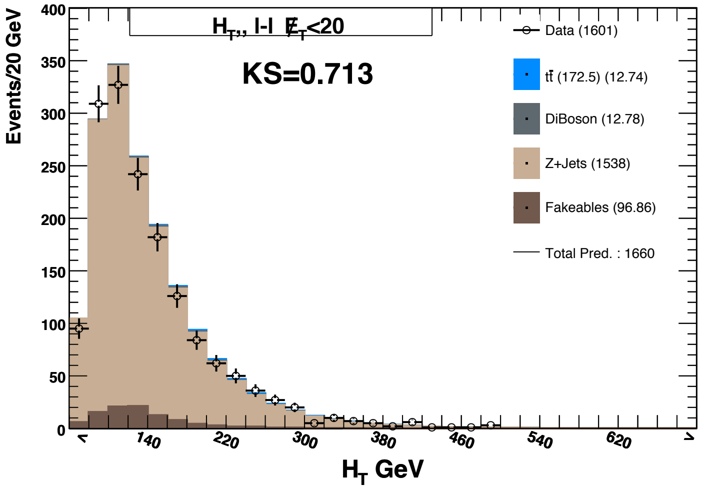

FIGURE 9.3. The scalar sum of transverse momentum, H_T, for pre-tag opposite-sign events with $\not{E}_T < 20$ GeV, ≥ 2 jets, and Met Significance > 4 GeV for ee and $\mu\mu$ events with invariant mass of 76 GeV/$c^2 < m_{\ell\ell} <$ 106 GeV/c^2.

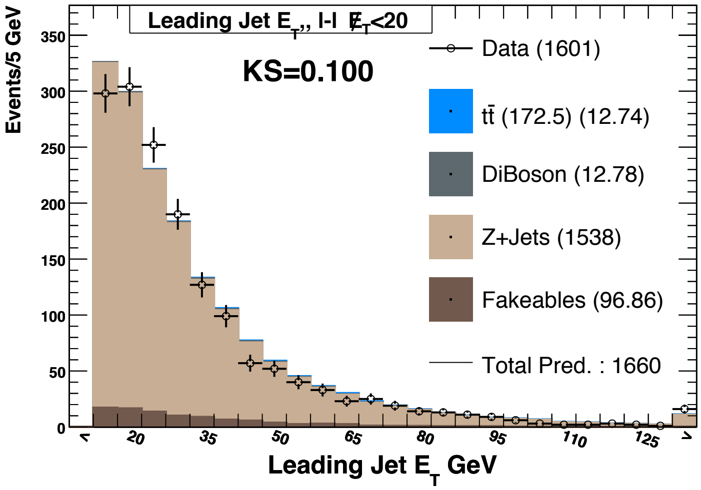

FIGURE 9.4. The E_T of the leading jet in pre-tag, opposite-sign events with $\not\!\!E_T < 20$ GeV, exactly 1 jet, and Met Significance > 4 GeV for ee and $\mu\mu$ events with invariant mass of 76 GeV$/c^2 < m_{\ell\ell} < 106$ GeV$/c^2$.

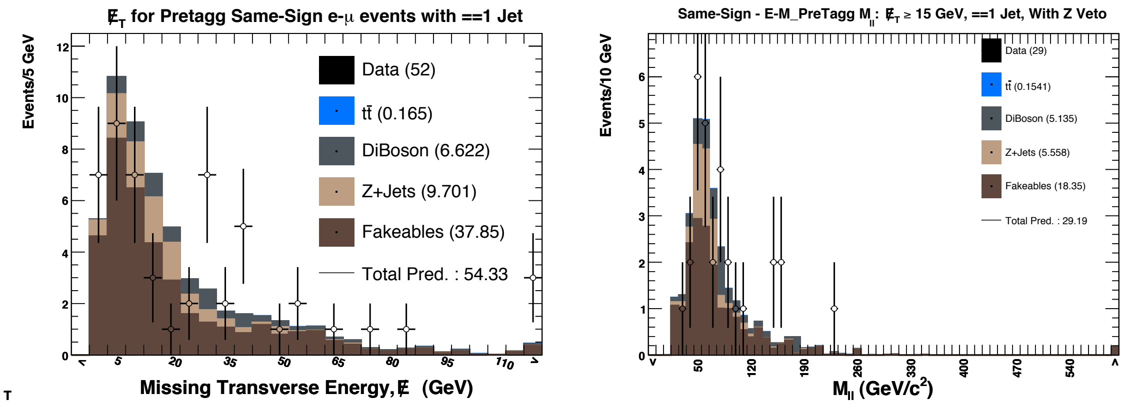

FIGURE 9.5. The $\not\!\!E_T$ distribution (left) and the invariant mass of leptons (right) in electron-muon same-sign events in the 1 jet bin. The invariant mass plot also requires $\not\!\!E_T > 15$ GeV . Theses plots show good modeling of the fake lepton background.

To facilitate reproduction, the population is recombined[3] until the original population size is reached again. The resulting sets of chromosomes are then subjected to random mutations, with the size of mutations either increasing or decreasing in magnitude depending on recent performance improvements. Fitness evaluation and reproduction are repeated until the fitness level reaches a plateau.

---

[3] That is, new offspring are created by combining randomly chosen chromosomes from two parents.

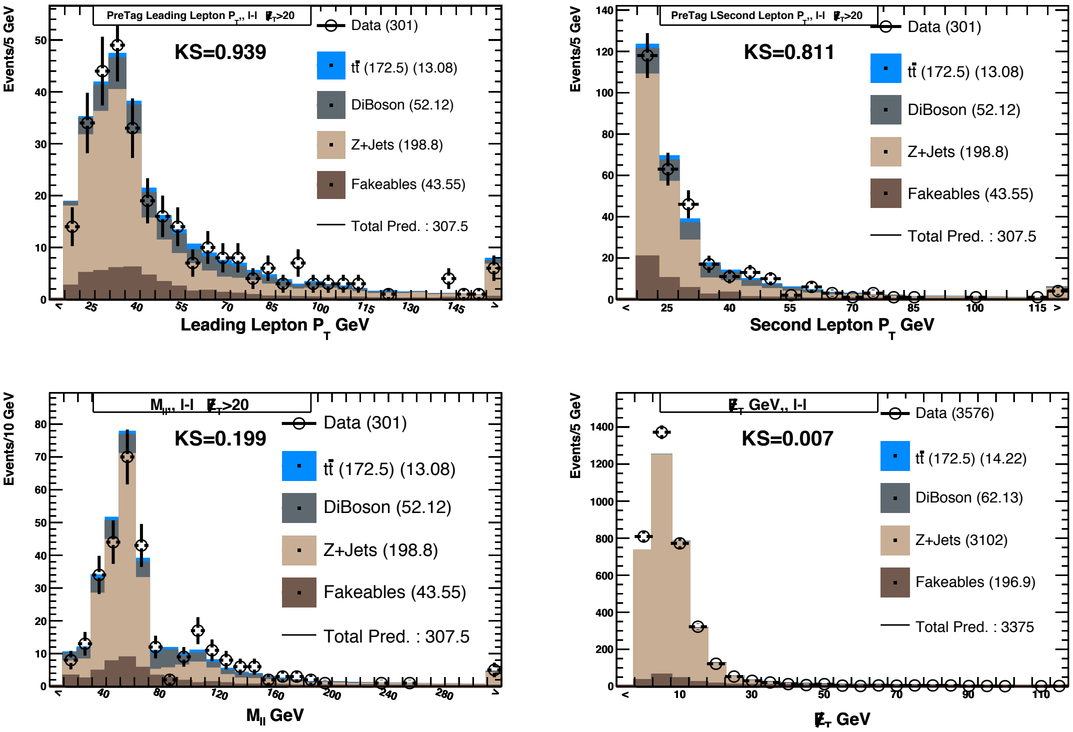

FIGURE 9.6. Kinematics of pre-tag, opposite-sign events with $\not{E}_T > 20$ GeV, exactly 1 jet, and Met Significance > 4 GeV for ee and $\mu\mu$ events with invariant mass of 76 GeV/$c^2 < m_{\ell\ell} < 106$ GeV/c^2.

For this analysis, the chromosomes represent event selection cut values, with an individual being defined by a complete set of event selection cuts. The fitness is the expected sensitivity to signal exclusion under the null hypothesis. So for this analysis, the Genetic event selection functions according to:

Initialization: A starting population of individuals is created with the set of event selection cuts randomly chosen for each individual.

Evaluation: For each individual, the signal and background estimations, the corresponding reconstructed stop mass distributions, and systematic uncertainties are all computed and fed into the limit finding machinery. The result is the individuals expected exclusion power being used as the individuals fitness.

Selection: Individuals are kept or discarded depending on their expected exclusion; the worst performing fraction of the population is removed from the population.

Reproduction: The surviving individuals are then crossed until the original population size is reached again. Mutation of the chromosomes values is then performed

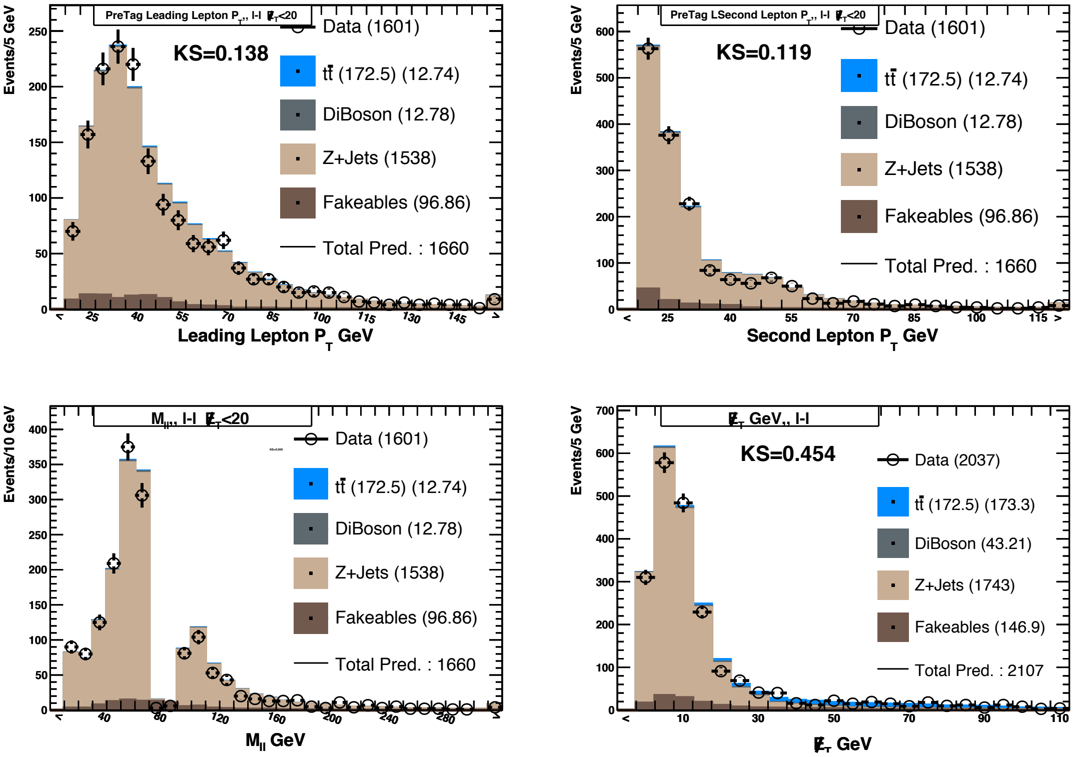

FIGURE 9.7. Kinematics of pre-tag, opposite-sign events with $\not\!\!E_T > 20$ GeV, $\geq$2 jets, and Met Significance > 4 GeV for ee and $\mu\mu$ events with invariant mass of 76 GeV$/c^2 < m_{\ell\ell} < 106$ GeV$/c^2$.

according to Gaussian distribution with a width that is dependent on how much improvement has been seen in the previous generations.

Termination: This process is repeated until no significant improvement is seen for a number of generations. The individual who showed the best performance is then selected as the candidate result.

A visual demonstration of this is presented in Fig. 9.3.

One of the benefits of Genetic algorithms is that they are able to probe a large parameter space in a relatively small amount of computational time in order to find a near optimal solution. Another benefit of Genetic algorithms (and why one was chosen for this analysis) is that they are less likely to get stuck in a locally optimal solution and miss the global solution. This is due in part, to the fact that it is a highly parallel algorithm, containing many candidate solutions at any one time. For other series-based optimization algorithms, if a solution runs into a "dead-end," the results obtained so far must be thrown away and

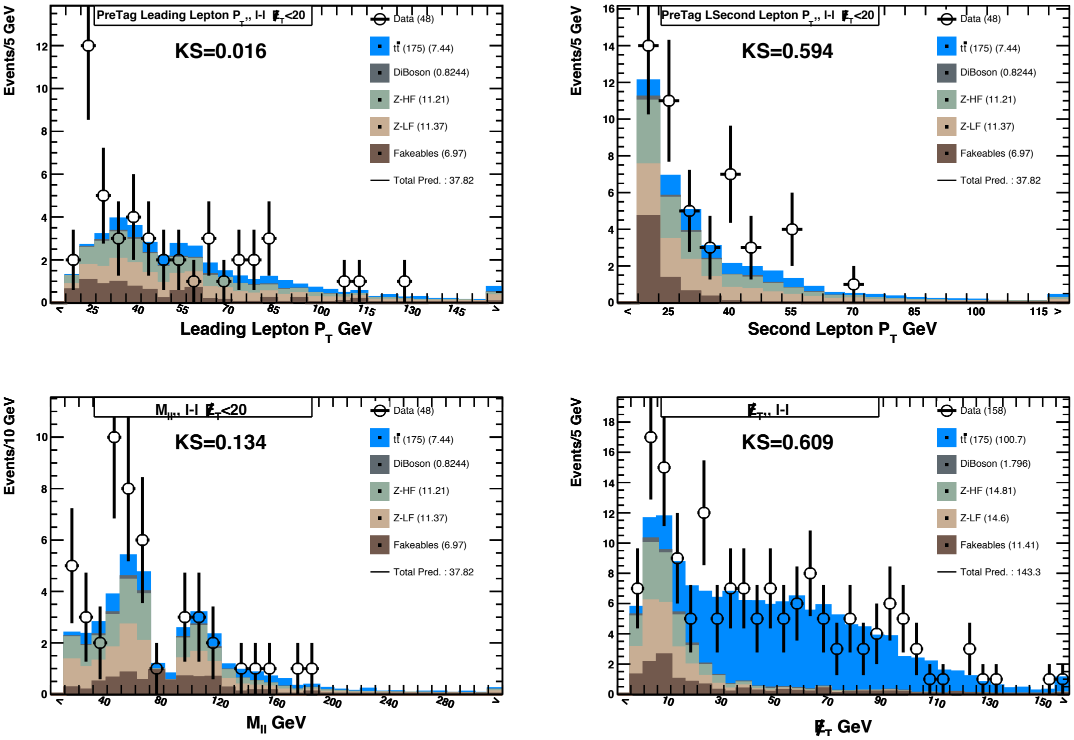

Figure 9.8. Kinematics of b-tagged opposite-sign events with $\not\!\!E_T < 20$ GeV, $\geq$2 jets, and and Met Significance $>$ 4 GeV for ee and $\mu\mu$ events with invariant mass of 76 GeV/$c^2 < m_{\ell\ell} <$ 106 GeV/c^2. It should be noted that the $\not\!\!E_T$ plot isn't strictly a control region, but it was not consulted before limits were set.

the process restarted from new initial conditions; in Genetic algorithms, the "dead-end" solutions are simply discarded and the optimization continues.

9.3.1. Optimization Strategy For This Analysis.

For this analysis, a population size of 100 individuals was used. The width of the mutation Gaussian is multiplied (divided) by 0.6 if less (more) than 3 of 6 generations saw improvement.

This optimization was performed in several steps. Firstly, for a set of reasonable event selection cuts chosen by hand, the expected sensitivity of the available signal Monte Carlo samples was evaluated to determine which samples could easily be excluded, and which samples had little sensitivity to exclusion. It was decided to optimize the event selection cuts on the samples which could potentially be excluded at dilepton branching ratios of 20-30%. The chosen SUSY mass scenarios were ($m(\tilde{t}_1)$, $m(\tilde{\chi}_1^{\pm})$, $m(\tilde{\chi}_1^0)$)={(155, 105.8, 58.8), (135, 105.8, 43.9), (155, 125.8, 58.8) }, with the masses measured in GeV/c^2. It was found

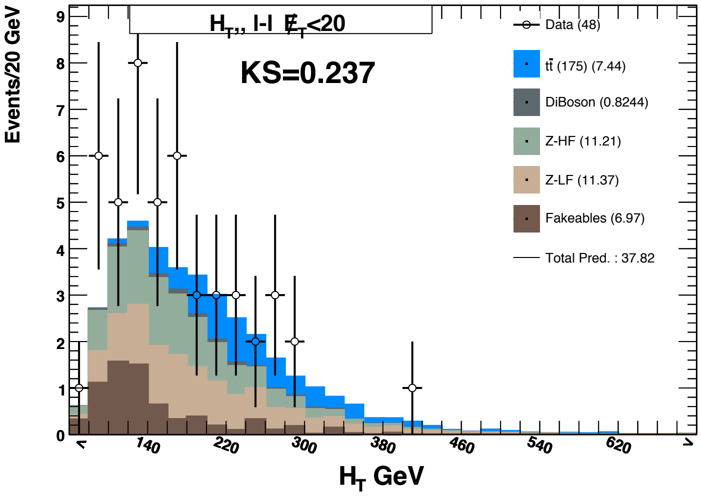

FIGURE 9.9. The scalar sum of transverse momentum, H_T, for b-tagged opposite-sign events with $\not{E}_T < 20$ GeV, $\geq$2 jets, and Met Significance $>$ 4 GeV for ee and $\mu\mu$ events with invariant mass of 76 GeV$/c^2 < m_{\ell\ell} <$ 106 GeV$/c^2$.

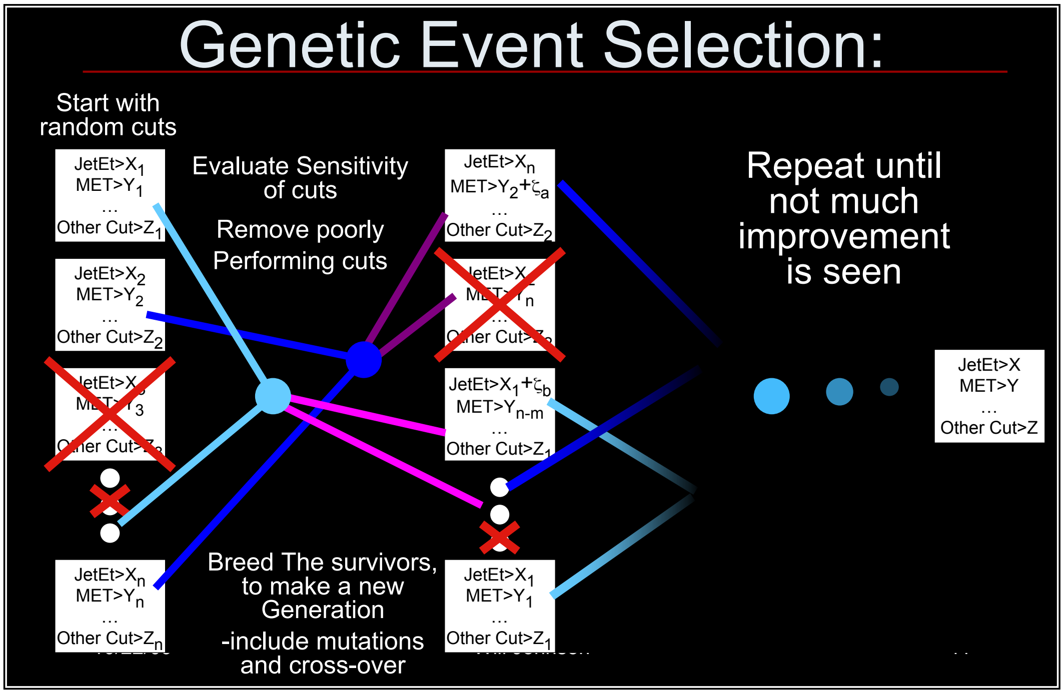

Genetic Event Selection:

Start with random cuts

JetEt>X_1
MET>Y_1
…
Other Cut>Z_1

JetEt>X_2
MET>Y_2
…
Other Cut>Z_2

JetEt>X_3
MET>Y_3
…
Other Cut>Z_3

JetEt>X_n
MET>Y_n
…
Other Cut>Z_n

Evaluate Sensitivity of cuts

Remove poorly Performing cuts

Breed The survivors, to make a new Generation

-include mutations and cross-over

JetEt>X_n
MET>$Y_2+\zeta_a$
…
Other Cut>Z_2

JetEt>X_x
MET>Y_n
…
Other Cut>Z_2

JetEt>$X_1+\zeta_b$
MET>Y_{n-m}
…
Other Cut>Z_1

JetEt>X_1
MET>Y_1
…
Other Cut>Z_1

Repeat until not much improvement is seen

JetEt>X
MET>Y
…
Other Cut>Z

FIGURE 9.10. A graphical representation of how the Genetic algorithm was used to optimize event selection cuts for this analysis.

that event selection cuts which worked well for one mass scenario, often worked well for other scenarios; this is primarily because the Standard Model background processes are the same for all scenarios and that one of the most powerful event selection cuts relied on the scalar nature of signal events ($H_T \leq A + \frac{\Delta\phi(\text{jet}_1,\text{jet}_2)\times\Delta\phi(\text{lep}_1,\text{lep}_2)}{\pi^2} \times B$) as opposed to the standard model backgrounds.

Event selection optimization was then performed twice, once to limit the phase space of allowed event selection cuts, and a second time to find an optimum set of event selection cuts in the limited phase space. The initial optimization allowed event selection cuts on the low or high values required for: jet E_T's; lepton p_T's; $\not\!\!E_T$; A and B for $H_T \leq A + \frac{\Delta\phi(\text{jet}_1,\text{jet}_2)\times\Delta\phi(\text{lep}_1,\text{lep}_2)}{\pi^2} \times B$; on the "L" cut, where if $\not\!\!E_T$ is below a given value, then the jets and leptons must be a given ϕ away from the $\not\!\!E_T$ direction; and how far $m_{\ell\ell}$ must be away from the Z-pole mass for ee and $\mu\mu$ events. It was found that the upper values on jet E_T's and lepton p_T's, and $\not\!\!E_T$ tended to be values above what was expected for signal or the Standard Model, so these possibilities were not included for the second round of event selection cuts. The lower values of the leptons' p_T tended to be near the predefined minimum of 20 GeV/c for identification, therefore this cut was not optimized in the second round of optimizations. Additionally, the $m_{\ell\ell}$ cut for near the Z-pole mass was seen to be not needed since it tended towards zero, probably due to the Z-veto imposed in pre-selection, so it was not used in the second round of optimizations either.

Listed below is the event selection cuts for which the analysis was optimized, and the allowed values the cuts could take, for the second round of optimizations. Although different selection cuts were allowed in the non-b-tagged channel and b-tagged channel, the same range of allowed cuts was used for each channel. The optimized cuts were:

Lead Jet E_T: Threshold values allowed were between 15 and 35 GeV.

Second Jet E_T: Threshold values allowed were between 12 and 35 GeV.

Missing Transverse Energy: Lower bounds between 15 and 55 GeV were allowed.

Topology Cut: In $H_T \leq A + \frac{\Delta\phi(\text{jet}_1,\text{jet}_2)\times\Delta\phi(\text{lep}_1,\text{lep}_2)}{\pi^2} \times B$, A was allowed to vary between 155 and 325, while B allowed between 200 and 475.

"L"-cut: This cut requires if $\not\!\!E_T$ is below a certain value, all jets and leptons must be further than another value in ϕ from the $\not\!\!E_T$direction. The $\not\!\!E_T$ requirement could vary between 20 and 65 GeV, and ϕ between 0 and 30 degrees.

Once the event selection optimization was performed for the benchmark SUSY mass scenarios, the resulting cuts were then applied to the other benchmark points. The set of cuts performing the combined best were then used for the event selection cuts[4]. Due to time constraint, the optimization was stopped before the pre-defined threshold of convergence (expected CL exclusion improvement by less than 0.009 in the previous 6 generations); however, solutions showed little improvement, and had progressed beyond 10 generations when stopped.

9.4. Final Event Selection Cuts

The final event selection cuts chosen were based on those optimized from ($m(\tilde{t}_1)$=135 GeV/c^2, $m(\tilde{\chi}_1^{\pm})$=105.8 GeV/c^2, $m(\tilde{\chi}_1^0)$=43.9 GeV/c^2 since these cuts performed nearly as well as the specifically optimized cuts on the other benchmark mass scenarios. The final event selection cuts can be seen in table 9.1. The final expected and observed event yields and sensitivities are found in the next chapter.

It is interesting to compare the expected event yields for the optimized event selection cuts to those traditionally used for top dilepton analyses. The notable differences between the optimized and traditional event selection cuts are traditionally both jets are required to have E_T>15 GeV, $\not{E}_T$>25 GeV, the topological cut is not required, the "L" cut is used in both channels, and the same cuts are used for the not-b-tagged and b-tagged channels [46]. For a SUSY mass scenario of $m(\tilde{t}_1) = 132.5$ GeV/c^2, $m(\tilde{\chi}_1^{\pm}) = 105.8$ GeV/c^2, $m(\tilde{\chi}_1^0) = 47.6$ GeV/c^2, at a dilepton branching ratio of 0.3, in the b-tagged channel[5]: for the optimized cuts 25.8 ± 5.1 signal events and 56.3 ± 5.9 background events are expected, while for the traditional cuts 16.9 ± 3.5 and 87.7 ± 9.8 events are expected for signal and background respectively. The optimization reduced the background uncertainty from 11.2% to 10.4%[6], and increased the $s/\sqrt{b}$ from 1.8 to 3.4. The effects of shape systematics on the optimization is harder to quantify, but were no doubt influential in the process.

---

[4] Values found were rounded to nearest integers, and where it made little difference in sensitivity, to the nearest multiple of 5. To paraphrase proffessor Maxwell Chertok in his particle physics course, people tend to ask fewer question about values that are multiples of the number of fingers on their hand.

[5] The majority of the sensitivity to signal comes from the b-tagged channel.

[6] The dominant rate uncertainty for both signal and background is the theoretical cross section uncertainty for signal and $t\bar{t}$ respectively, which event selection optimization could do little to mitigate.

Variable	Non-b-Tagged Channel	b-Tagged Channel
Two leptons	$m_{\ell\ell}$ >20 GeV/c^2, p_T>20 GeV/c, oppositely charged	
Met Significance	> 4 GeV (for ee and $\mu\mu$: $76 < m_{\ell\ell} < 106$ GeV/c^2)	
Topology cut A	215 GeV	
Topology cut B	325 GeV	
$\not\!\!E_T$	> 20 GeV	
$E_T^{jet_1}$	> 20 GeV	> 15 GeV
$E_T^{jet_2}$	>20 GeV	> 12 GeV
"L"-cut $\not\!\!E_T$	50 GeV	None
"L"-cut $\Delta\phi$	20^0	None

Table 9.1. Final event selection cuts for this analysis. The topology cut variables refer to $H_T \leq A + \frac{\Delta\phi(\mathrm{jet}_1,\mathrm{jet}_2)\times\Delta\phi(\mathrm{lep}_1,\mathrm{lep}_2)}{\pi^2} \times B$. $\not\!\!E_T$ is corrected for jets with $E_T \geq 12$ GeV, to level 5. Also Cosmic and Conversion veto's are applied, as well as the silicon good run list applied.

CHAPTER 10

Results and Conclusion

This search for the supersymmetric partner of the top quark was optimized according to expected sensitivity to signal exclusion under the Standard Model only hypothesis for 1.9 fb^{-1} of data. The researchers remained blind to the observed data sample in the signal region until all aspects of the analysis' design were finalized, and sufficient physics modeling was extensively ensured in control regions. The signal region of the observed data sample was originally consulted in April of 2008 using 1.9 fb^{-1} of data. The observed data sample was observed to be consistent with the standard model only hypothesis; consequently 95% CL limits were placed on the dilepton branching ratio for $\tilde{t}_1\bar{\tilde{t}}_1$ events at theoretical cross sections. The results were updated in May of 2009 to include 2.7 fb^{-1} of data, using the same event selection cuts and methodologies as before, in order to improve the previous limits with the increased statistics. The final exclusion limits can be seen in Fig. 10.1.

Events per 2.7 fb^{-1} in the signal region with ≥1 b-tag

Source				ee	$\mu\mu$	$e\mu$	ll
top				11.6 ± 1.8	10.4 ± 1.5	27.0 ± 3.7	49.0 ± 6.9
z/γ^*+HF				1.2 ± 0.2	0.8 ± 0.1	0.4 ± 0.1	2.4 ± 0.4
z/γ^*+LF				0.8 ± 0.1	0.5 ± 0.1	0.3 ± 0.1	1.6 ± 0.2
diboson				0.2 ± 0.1	0.1 ± 0.1	0.2 ± 0.1	0.5 ± 0.1
fakeables				0.5 ± 0.2	0.5 ± 0.1	1.9 ± 0.6	2.8 ± 0.9
Total				14.3 ± 2.0	12.3 ± 1.6	29.7 ± 3.8	56.4 ± 7.2
$m(\tilde{t})$	$m(\tilde{\chi}^{\pm})$	$m(\tilde{\chi}^{0})$	BR	$\tilde{t}_1\bar{\tilde{t}}_1$ Signal			
132.5	105.8	47.6	0.11	2.0 ± 0.4	2.1 ± 0.5	5.4 ± 1.1	9.5 ± 1.9
155.8	105.8	64.9	0.5	0.8 ± 0.2	1.0 ± 0.2	2.3 ± 0.4	4.1 ± 0.8
179.2	105.8	61.3	1.0	0.5 ± 0.1	0.6 ± 0.1	1.3 ± 0.3	2.3 ± 0.4
135.0	125.8	55.1	0.25	0.4 ± 0.1	0.6 ± 0.1	1.2 ± 0.3	2.2 ± 0.5
160.0	125.8	58.8	0.25	1.2 ± 0.2	1.2 ± 0.2	3.0 ± 0.6	5.4 ± 1.1
168.3	125.8	71.7	0.5	0.7 ± 0.1	0.8 ± 0.2	1.9 ± 0.4	3.3 ± 0.7
Data	15	12	30	57			

TABLE 10.1. Predicted vs. observed number of events in the b-tagged signal region. For signal, the masses of the SUSY particles are quoted in units of GeV/c^2 and normalized to the dilepton branching ratio (BR) excluded at the 95% CL.

Events per 2.7 fb^{-1} in the not-b-tagged signal region

Source				ee	$\mu\mu$	$e\mu$	ll
top				6.1 ± 0.9	6.1 ± 1.0	13.0 ± 1.8	25.2 ± 3.3
z/γ^*+HF				0.3 ± 0.1	0.3 ± 0.0	0.1 ± 0.1	0.7 ± 0.1
z/γ^*+LF				11.9 ± 3.3	8.2 ± 2.1	4.1 ± 0.3	24.3 ± 5.6
diboson				1.7 ± 0.4	1.4 ± 0.3	2.9 ± 0.7	6.0 ± 1.3
fakeables				1.8 ± 0.6	2.0 ± 0.6	5.9 ± 1.8	9.8 ± 2.9
Total				21.9 ± 3.9	18.0 ± 2.9	26.1 ± 4.0	65.9 ± 9.8
$m(\tilde{t})$	$m(\tilde{\chi}^{\pm})$	$m(\tilde{\chi}^{0})$	BR	$\tilde{t}_1\bar{\tilde{t}}_1$ Signal			
132.5	105.8	47.6	0.11	0.8 ± 0.2	0.9 ± 0.3	2.2 ± 0.5	3.9 ± 0.9
155.8	105.8	64.9	0.5	0.3 ± 0.1	0.4 ± 0.1	0.9 ± 0.2	1.6 ± 0.3
179.2	105.8	61.3	1.0	0.2 ± 0.1	0.2 ± 0.1	0.5 ± 0.1	1.0 ± 0.2
135.0	125.8	55.1	0.25	0.5 ± 0.1	0.6 ± 0.2	1.2 ± 0.3	2.2 ± 0.5
160.0	125.8	58.8	0.25	0.4 ± 0.1	0.5 ± 0.1	1.2 ± 0.3	2.0 ± 0.3
168.3	125.8	71.7	0.5	0.3 ± 0.1	0.3 ± 0.1	0.7 ± 0.2	1.3 ± 0.3
Data				27	12	26	65

TABLE 10.2. Predicted vs. observed number of events in the not-b-tagged signal region. For signal, the masses of the SUSY particles are quoted in units of GeV/c^2 and normalized to the dilepton branching ratio (BR) excluded at the 95% CL.

The observed and predicted number of events in the signal region for 2.7 fb^{-1} of data can be seen in tables 10.1 and 10.2 for the b-tagged and not-b-tagged channels respectively. It can be seen that the number of evente in the observed data sample is consistent with standard model prediction. An interesting thing to note from the tables is that for most SUSY mass scenarios the number of signal events excluded at the 95% CL is actually smaller than the magnitude of the 1σ systematic uncertainty on the prediction of the Standard Model. This shows that most of the discrimination power comes from the shape of the reconstructed stop mass, as opposed to the raw number of observed events. The reconstructed stop mass distributions in the observed data sample is also consistent with the standard model only hypothesis, as can be seen for various SUSY mass scenarios in Figures 10.2 through 10.11.

A study was carried out to determine the increase in sensitivity that additional data would bring to this analysis. The results can be seen in Fig. 10.12, where it can be seen that the increase in expected sensitivity does not significantly improve above the levels reported in this paper. To increase the sensitivity of this search, improvements in the method would be necessary, such as including the lepton plus jets channel or reducing the p_T requirement of the second lepton in the event. It is not planned to update this search using data from the CDF II detector.

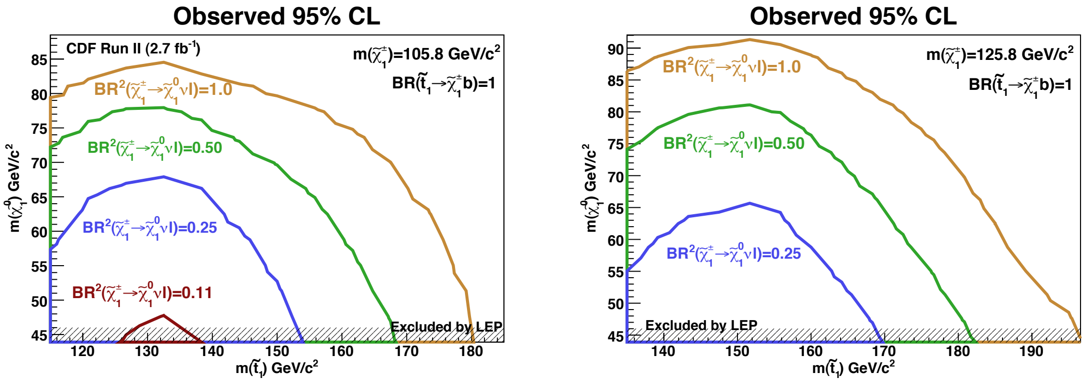

FIGURE 10.1. The observed 95% CL exclusion levels for in the plane of $\tilde{t}_1$ and $\tilde{\chi}_1^0$ masses for $m(\tilde{\chi}^\pm) = 105.8\,\text{GeV}/c^2$ (left) and $m(\tilde{\chi}^\pm) = 105.8\,\text{GeV}/c^2$ (right), for various dilepton branching ratios.

The limits set by this analysis are the first for this decay scenario of $\tilde{t}_1\bar{\tilde{t}}_1$ events. The limits set for a branching ratio of 0.11 for stop masses between 128 and 135 GeV/c^2 for $m(\tilde{\chi}^\pm) = 105.8$ and $m(\tilde{\chi}^0) = 47.6\,\text{GeV}/c^2$ are independent of the dilepton branching ratio. This analysis was performed to be dependent only on SUSY parameters as far as they effect masses of $\tilde{t}_1$, $\tilde{\chi}_1^\pm$, $\tilde{\chi}_1^0$; therefore the limits obtained are applicable to any R-parity conserving SUSY scenario where the neutralino is the LSP and the stop decays exclusively in $\tilde{\chi}_1^\pm$b.

In conclusion, this paper presents the results of a search for pair production of supersymmmetric stop quarks decaying via $\tilde{t}_1 \rightarrow b\tilde{\chi}_1^\pm \rightarrow b\tilde{\chi}_1^0\ell^\pm\nu$ using an observed data sample corresponding to 2.7 fb^{-1} of integrated luminosity in 1.96 TeV $p\bar{p}$ collisions. The fit to the observed reconstructed stop mass distribution reveals no evidence for $\tilde{t}_1\bar{\tilde{t}}_1$ production. World first limits are placed on the masses of $\tilde{t}_1$ and $\tilde{\chi}_1^0$ for several values of $m(\tilde{\chi}_1^\pm)$ and branching ratios of BR$(\tilde{\chi}_1^\pm \rightarrow \tilde{\chi}_1^0\ell^\pm\nu)$.

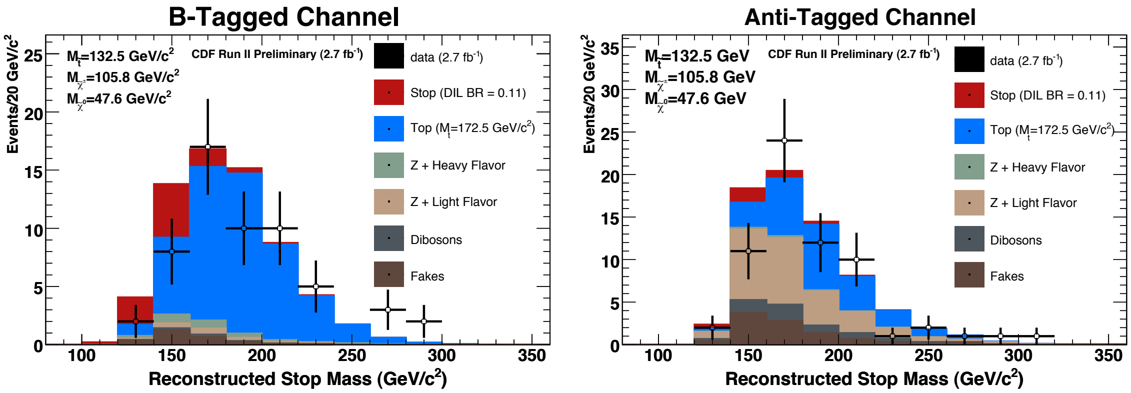

FIGURE 10.2. The reconstructed stop mass distributions for the b-tagged (left) and not-b-tagged (right) channels. Signal is plotted at the dilepton branching ratio of 0.11, the level excluded at the 95% CL for the SUSY mass scenario of $m(\tilde{t}) = 132.5$ GeV$/c^2$, $m(\tilde{\chi}^{\pm}) = 105.8$ GeV$/c^2$, and $m(\tilde{\chi}^0) = 47.6$ GeV$/c^2$.

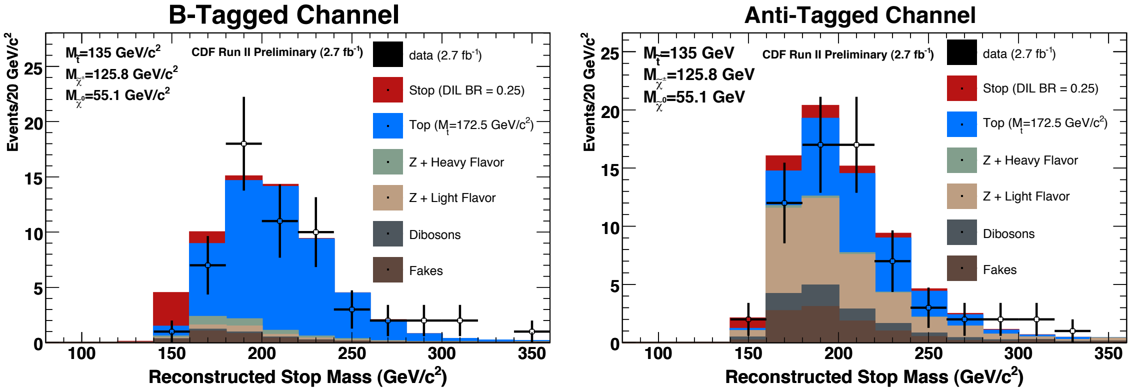

FIGURE 10.3. The reconstructed stop mass distributions for the b-tagged (left) and not-b-tagged (right) channels. Signal is plotted at the dilepton branching ratio of 0.25, the level excluded at the 95% CL for the SUSY mass scenario of $m(\tilde{t}) = 135$ GeV$/c^2$, $m(\tilde{\chi}^{\pm}) = 125.8$ GeV$/c^2$, and $m(\tilde{\chi}^0) = 55.1$ GeV$/c^2$.

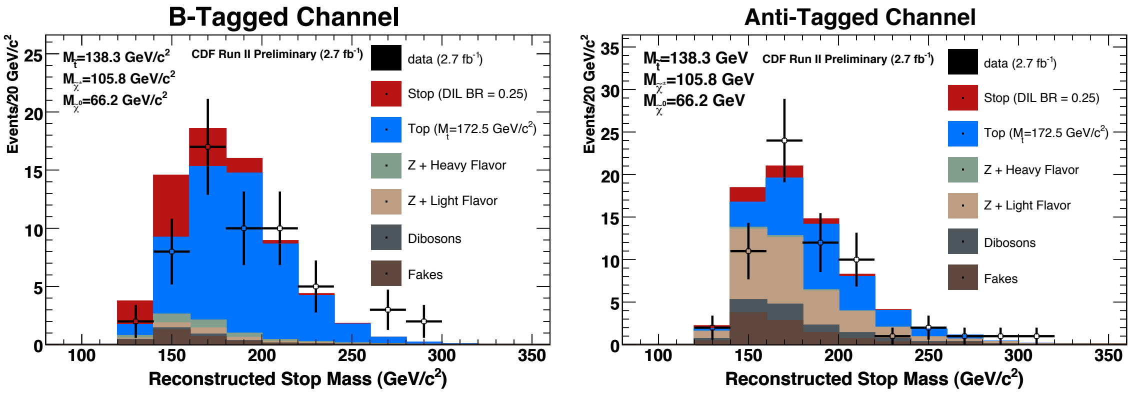

FIGURE 10.4. The reconstructed stop mass distributions for the b-tagged (left) and not-b-tagged (right) channels. Signal is plotted at the dilepton branching ratio of 0.25, the level excluded at the 95% CL for the SUSY mass scenario of $m(\tilde{t}) = 138.3$ GeV$/c^2$, $m(\tilde{\chi}^{\pm}) = 105.8$ GeV$/c^2$, and $m(\tilde{\chi}^0) = 66.2$ GeV$/c^2$.

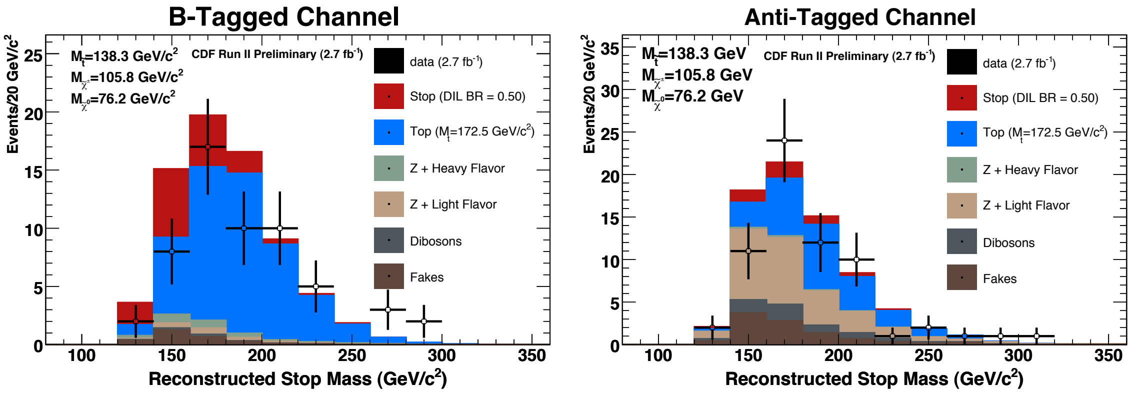

FIGURE 10.5. The reconstructed stop mass distributions for the b-tagged (left) and not-b-tagged (right) channels. Signal is plotted at the dilepton branching ratio of 0.5, the level excluded at the 95% CL for the SUSY mass scenario of $m(\tilde{t}) = 138.3$ GeV$/c^2$, $m(\tilde{\chi}^{\pm}) = 105.8$ GeV$/c^2$, and $m(\tilde{\chi}^0) = 76.2$ GeV$/c^2$.

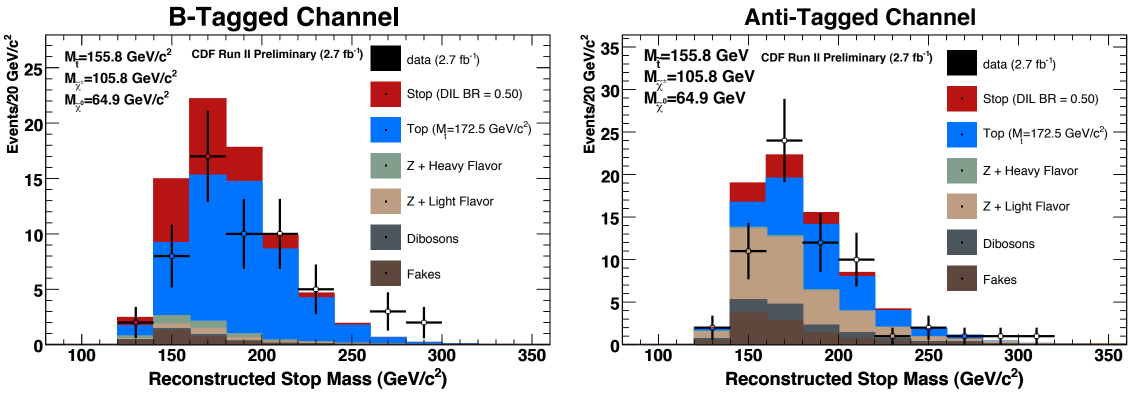

FIGURE 10.6. The reconstructed stop mass distributions for the b-tagged (left) and not-b-tagged (right) channels. Signal is plotted at the dilepton branching ratio of 0.5, the level excluded at the 95% CL for the SUSY mass scenario of $m(\tilde{t}) = 155.8\ \mathrm{GeV}/c^2$, $m(\tilde{\chi}^{\pm}) = 105.8\ \mathrm{GeV}/c^2$, and $m(\tilde{\chi}^0) = 64.9\ \mathrm{GeV}/c^2$.

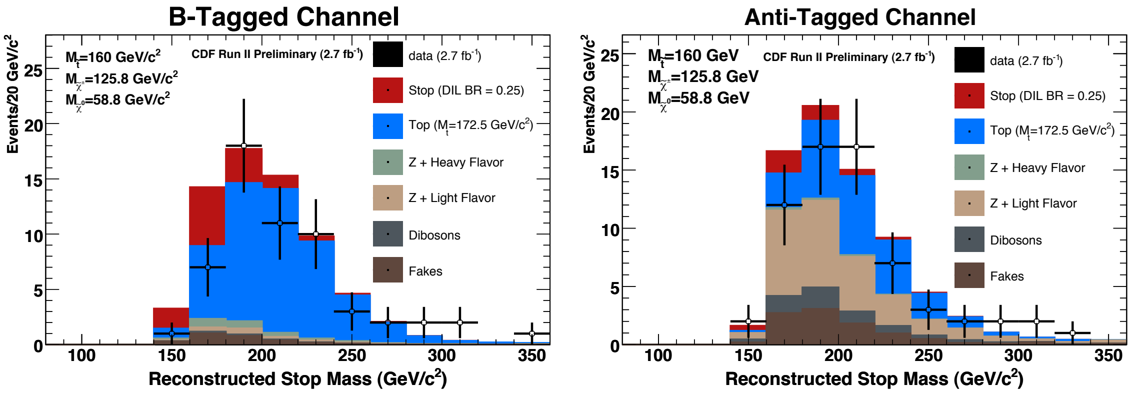

FIGURE 10.7. The reconstructed stop mass distributions for the b-tagged (left) and not-b-tagged (right) channels. Signal is plotted at the dilepton branching ratio of 0.25, the level excluded at the 95% CL for the SUSY mass scenario of $m(\tilde{t}) = 160\ \mathrm{GeV}/c^2$, $m(\tilde{\chi}^{\pm}) = 125.8\ \mathrm{GeV}/c^2$, and $m(\tilde{\chi}^0) = 58.8\ \mathrm{GeV}/c^2$.

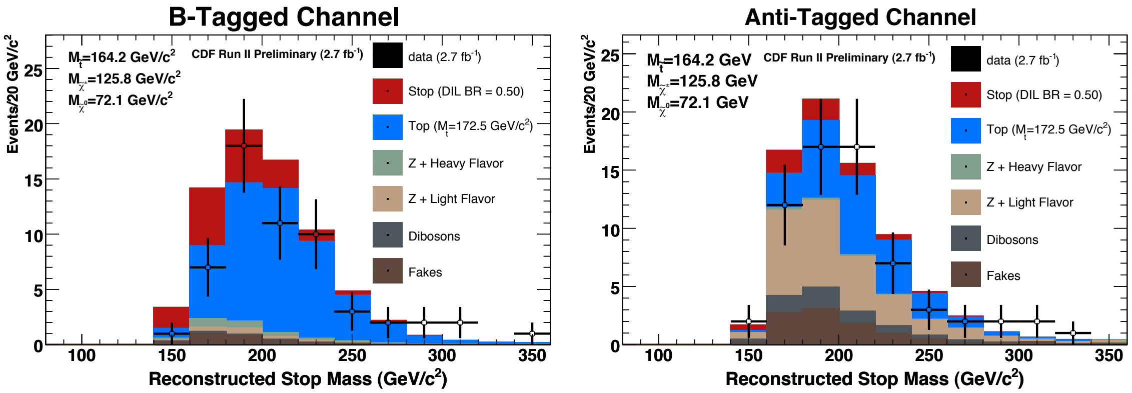

FIGURE 10.8. The reconstructed stop mass distributions for the b-tagged (left) and not-b-tagged (right) channels. Signal is plotted at the dilepton branching ratio of 0.5, the level excluded at the 95% CL for the SUSY mass scenario of $m(\tilde{t}) = 164.2\ \mathrm{GeV}/c^2$, $m(\tilde{\chi}^{\pm}) = 125.8\ \mathrm{GeV}/c^2$, and $m(\tilde{\chi}^0) = 72.1\ \mathrm{GeV}/c^2$.

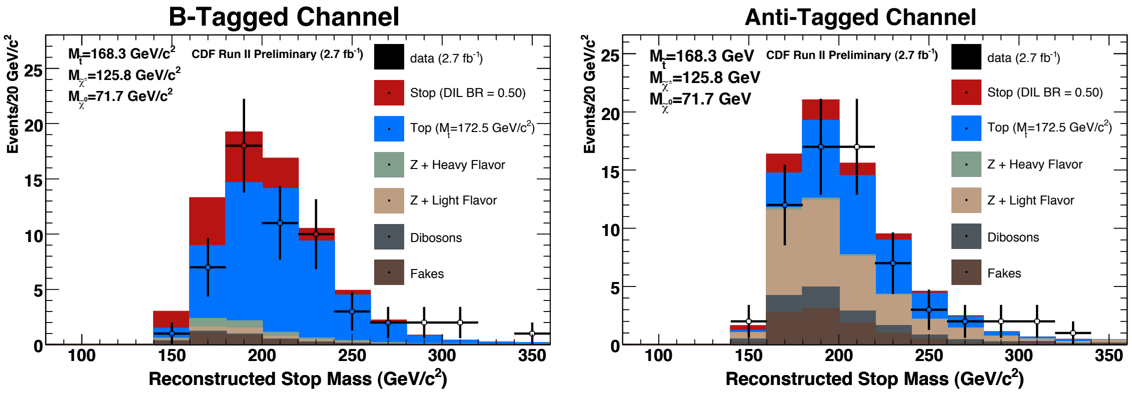

FIGURE 10.9. The reconstructed stop mass distributions for the b-tagged (left) and not-b-tagged (right) channels. Signal is plotted at the dilepton branching ratio of 0.5, the level excluded at the 95% CL for the SUSY mass scenario of $m(\tilde{t}) = 168.3\ \mathrm{GeV}/c^2$, $m(\tilde{\chi}^{\pm}) = 125.8\ \mathrm{GeV}/c^2$, and $m(\tilde{\chi}^0) = 71.7\ \mathrm{GeV}/c^2$.

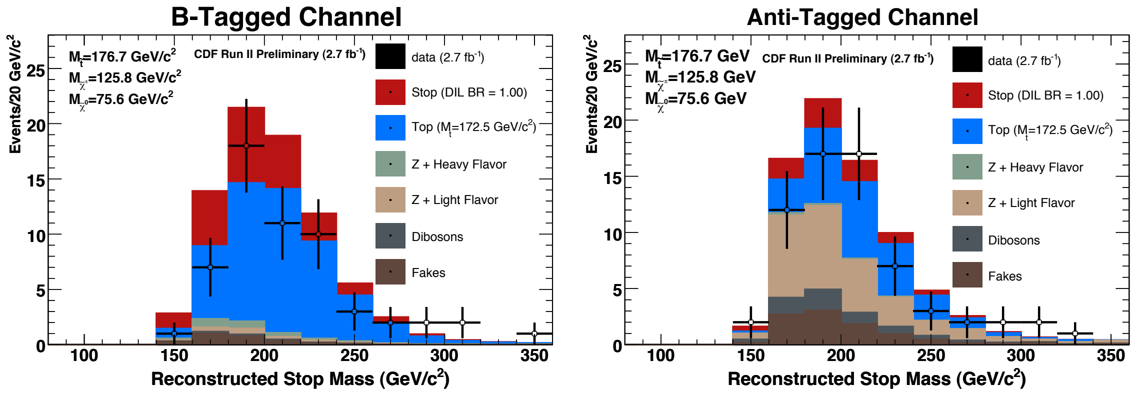

FIGURE 10.10. The reconstructed stop mass distributions for the b-tagged (left) and not-b-tagged (right) channels. Signal is plotted at the dilepton branching ratio of 1.0, the level excluded at the 95% CL for the SUSY mass scenario of $m(\tilde{t}) = 176.7$ GeV$/c^2$, $m(\tilde{\chi}^{\pm}) = 125.8$ GeV$/c^2$, and $m(\tilde{\chi}^0) = 75.6$ GeV$/c^2$.

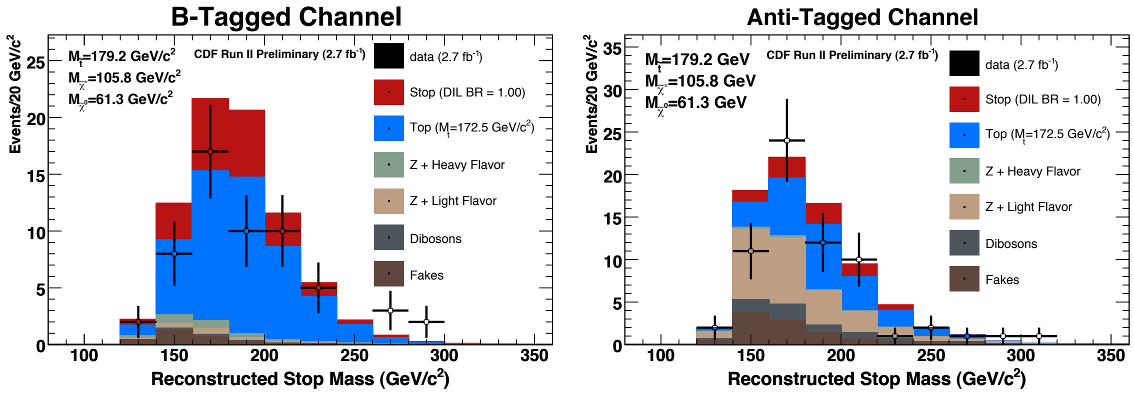

FIGURE 10.11. The reconstructed stop mass distributions for the b-tagged (left) and not-b-tagged (right) channels. Signal is plotted at the dilepton branching ratio of 1.0, the level excluded at the 95% CL for the SUSY mass scenario of $m(\tilde{t}) = 179.2$ GeV$/c^2$, $m(\tilde{\chi}^{\pm}) = 105.8$ GeV$/c^2$, and $m(\tilde{\chi}^0) = 61.3$ GeV$/c^2$.

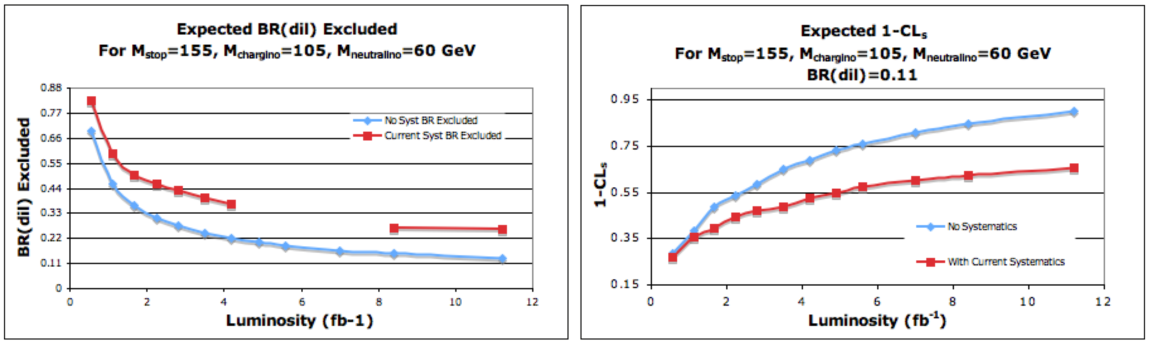

FIGURE 10.12. Left: The expected dilepton branching ratio which could be excluded at the 95% CL as a function of integrated luminosity. Right: The expected exclusion confidence level (1-CL$_S$) for $\tilde{t}_1\bar{\tilde{t}}_1$ at a dilepton branching ratio of 0.11, as a function of integrated luminosity. Both graphs are for the SUSY mass scenario of $m(\tilde{t}) = 155\,\mathrm{GeV}/c^2$, $m(\tilde{\chi}^{\pm}) = 105.8\,\mathrm{GeV}/c^2$, and $m(\tilde{\chi}^0) = 58.8\,\mathrm{GeV}/c^2$, using the final event selection cuts. The red lines are considering systematic uncertainties at the $2.7\,\mathrm{fb}^{-1}$ levels, while the blue lines do not include any systematic uncertainties.

Bibliography

[1] Eugene Paul Wigner. Symmetries and reflections : scientific essays, 1967.

[2] Emmy Noether and M. A. Tavel. Invariant variation problems, 2005. `http://www.citebase.org/abstract?id=oai:arXiv.org:physics/0503066`.

[3] Michael Peskin and Daniel Schroeder. *An Introduction to Quantum Field Theory*. Addison-Wesley, 1995.

[4] Quang Ho-Kim and Pham Xuan Yem. *Elementary Particles and Their Interactions*. Springer, 1998.

[5] John Jackson. *Classical Electrodynamics*. Wiley, 1998.

[6] B. Odom, D. Hanneke, B. D'Urso, and G. Gabrielse. New measurement of the electron magnetic moment using a one-electron quantum cyclotron. *Physical Review Letters*, 97(3):030801, 2006.

[7] S. F. Novaes. Standard model: An Introduction. 1999.

[8] Stephen L. Adler. Axial-vector vertex in spinor electrodynamics. *Phys. Rev.*, 177(5):2426–2438, Jan 1969.

[9] Alan R. White. Electroweak high-energy scattering and the chiral anomaly. *Phys. Rev. D*, 69(9):096002, May 2004.

[10] Ian Aitchison and Anthony Hey. *Gauge Theories In Particle Physics*. IoP, 2003.

[11] C. amsler et al. (particle data group), physics letters b667, 1, 2008.

[12] Gerard t' Hooft and Martinus Veltman. Regularization and renormalization of gauge fields. *Nucl. Phys. B*, 44:189 – 213, 1972.

[13] R. N. Mohapatra et al. Theory of neutrinos: A white paper, 2007.

[14] John Barrow. Cosmology, life, and the anthropic principle. *Annals of the New York Academy of Sciences*, 950:139–153, 2001.

[15] E H Thorndike. Production and decay of the b quark. *Annual Review of Nuclear and Particle Science*, 35(1):195–244, 1985.

[16] Stephen P. Martin. A Supersymmetry Primer. 1997.

[17] L. Girardello and M. T. Grisaru. Soft breaking of supersymmetry. *Nuclear Physics B*, 194(1):65 – 76, 1982.

[18] Ken ichi Hikasa and Makoto Kobayashi. Light scalar top quark at e^+e^- coliders. *Phys. Lett. D.*, 36(3):36–45, Aug 1987.

[19] A. Heister et al. Absolute mass lower limit for the lightest neutralino of the mssm from e+e- data at up to 209 gev. *Physics Letters B*, 583(3-4):247 – 263, 2004.

[20] Jean-Baptiste De Vivie and Jean-Francois Grivaz. Combined lower bound of the neutralino mass in a constrained mssm model. The LEP SUSY Working Group final results, June 2004.

[21] C. Balázs, M. Carena, and C. E. M. Wagner. Dark matter, light top squarks, and electroweak baryogenesis. *Phys. Rev. D*, 70(1):015007, Jul 2004.

[22] LEP2 SUSY Working Group. Combined lep chargino results, up to 208 gev for large m0. The LEP SUSY Working Group final results, Feb 2001.

[23] CDF Collaboration. Search for supersymmetric top quarks decaying to a b quark and a tau lepton, 2005. `http://www-cdf.fnal.gov/physics/exotic/r2a/20050728.jtau_rpvstop/`.

[24] CDF Collaboration. Search for scalar top quark production in $p\bar{p}$ collisions at $\sqrt{s} = 1.8$ TeV. *Phys. Rev. Lett.*, 84(23):5273–5278, Jun 2000.

[25] D0 Collaboration. Search for scalar top admixture in the $t\bar{t}$ lepton+jets channel at D0, 2007.

[26] Accelerator concepts rookie books, 2009. `http://www-bdnew.fnal.gov/operations/rookie_books/rbooks.html`.

[27] D. Amidei et al. The CDF II Detector Technical Design Report. 1996.

[28] D. Acosta et al. The performance of the CDF luminosity monitor. *Nucl. Instrum. Meth.*, A494:57–62, 2002.

[29] J. Thom, D. Glenzinski, M. Herndon, C.-J. Lin, and A Yagil. Determination of the Run II COT Tracking Efficiency Using the WNotrack Sample. Internal CDF note 6866, 2004.

[30] Douglas Glenzinski Victoria Giakoumopoulou, Nikos Giokaris. The COT Pattern Recognition Algorithm and Offline Code. Internal CDF note 9281, 2008.

[31] Chris Hays, Peter Tamburello, Ashutosh Kotwal, Peter Wittich, and Rick Snider. The COT Pattern Recognition Algorithm and Offline Code. Internal CDF note 6992, 2004.

[32] D. Glenzinski, P. Merkel, J. Thom, A. Yagil, C. Hill, J. Incandela, C. Mills, N. Lockyer, P. Wittich, P. Savard, and R. Tafirout. Addition of PHX Electrons to the Dilepton Analysis using the Tight Lepton and Isolated Track Sample. Internal CDF note 6787, 2004.

[33] Carsten Rott and Daniela Bortoletto. Primary Vertex Algorithm Comparison for High p_T Physics. Internal CDF note 6472, 2003.

[34] Salvatore Rappoccia and Joao Guimaraes da Costa. Impact of PrimeVtx on SecVtx For Summer 2003 Conferences. Internal CDF note 6666, 2004.

[35] A. Bhatti *et al.* Determination of the jet energy scale at the collider detector at fermilab. *Nuclear Instruments and Methods in Physics Research Section A: Accelerators, Spectrometers, Detectors and Associated Equipment*, 566(2):375 – 412, 2006.

[36] H. L. Lai, J. Huston, S. Kuhlmann, J. Morfin, F. Olness, J. F. Owens, J. Pumplin, and W. K. Tung. Global qcd analysis of parton structure of the nucleon: Cteq5 parton distributions. *European Physical Journal C*, 12:375, 2000.

[37] J. Pumplin, D. R. Stump, J. Huston, H. L. Lai, P. Nadolsky, and W. K. Tung. New generation of parton distributions with uncertainties from global qcd analysis, 2002.

[38] Matt A. Dobbs, Stefano Frixione, Eric Laenen, and Kirsten. Tollefson. Les houches guidebook to monte carlo generators for hadron collider physics. *Lawrence Berkeley National Laboratory*, 54641, 2004.

[39] Torbjorn Sjostrand, Stephen Mrenna, and Peter Skands. Pythia 6.4 physics and manual. *JHEP*, 0605:026, 2006.

[40] Michelangelo L. Mangano, Mauro Moretti, Fulvio Piccinini, Roberto Pittau, and Antonio D. Polosa. ALPGEN, a generator for hard multiparton processes in hadronic collisions. *JHEP*, 07:001, 2003.

[41] Z. Was. Tauola the library for tau lepton decay, and kkmc/koralb/koralz/... status report. *Nuclear Physics B - Proceedings Supplements*, 98:96, 2001.

[42] QQ Pharoah David Jaffe. Comprehensive qq documentation. `http://www.lns.cornell.edu/public/CLEO/soft/QQ/qq_expert.html`.

[43] S. Agostinelli et al. GEANT4: A simulation toolkit. *Nucl. Instrum. Meth.*, A506:250–303, 2003.

[44] G. Grindhammer and S. Peters. The parameterized simulation of electromagnetic showers in homogeneous and sampling calorimeters, 2000.

[45] T. et el Aaltonen. Measurement of the top quark mass at cdf using the "neutrino ϕ weighting" template method on a lepton plus isolated track sample. *Phys. Rev. D*, 79(7):072005, Apr 2009.

[46] T. et el Aaltonen. First simultaneous measurement of the top quark mass in the $lepton + jets$ and dilepton channels at cdf. *Phys. Rev. D*, 79(9):092005, May 2009.

[47] Doug Glenzinski, Daniel Whiteson, and Erik Brubaker for the CDF Collaboration. CDF Combined Top Mass for Spring 2006. `http://www-cdf.fnal.gov/physics/new/top/2006/mass/combination/CDFApr06.html`, April 2006.

[48] The CDF Collaboration. Summary of CDF Top Mass Results - March 2009. `http://www-cdf.fnal.gov/physics/new/top/2009/mass/cdfcombination_march/`, March 2009.

[49] W. Beenakker *et al.* PROSPINO - To be filled in when I get internet. *Nucl. Phys B*, 515:3–14, 1998.

[50] Matteo Cacciari, Stefano Frixione, Giovanni Ridolfi, Michelangelo L. Mangano, and Paolo Nason. The t&bart; cross-section at 1.8 and 1.96 tev: a study of the systematics due to parton densities and scale dependence. *Journal of High Energy Physics*, 2004(04):068–068, 2004.

[51] J. M. Campbell and R. K. Ellis. Update on vector boson pair production at hadron colliders. *Phys. Rev. D*, 60(11):113006, Nov 1999.

[52] et al. C. Plager. Updated search for the flavor changing neutral current decay $t \rightarrow zq$ with 1.9 fb^{-1} of cdf ii data. Internal CDF note 9161, 2007.

[53] The cdf jet energy and resolution group. Website, 2008. `http://www-cdf.fnal.gov/internal/physics/top/jets/corrections.html`.

[54] E. Brubaker, et al. Updated Measurement of the Top Quark Mass in the Lepton + Jets Channel. Internal CDF note 6845, 2004.

[55] F. James and M. Roos. Minuit - a system for function minimization and analysis of the parameter errors and correlations. *Computer Physics Communications*, 10(343), 1975.

[56] The CDF Collaboration. Summary of Tevatron Top Mass Results - July 2008. `http://www-cdf.fnal.gov/physics/new/top/2008/mass/tevcombination_july/`, July 2008.

[57] D. Acosta, S. Klimenko, J. Konigsberg, A. Korytov, G. Mitselmakher, V. Necula, A. Nomerotsky, A. Pronko, A. Sukhanov, A. Safonov, D. Tsybychev, S. M. Wang, and M. Wong. The performance of the cdf luminosity monitor. *Nuclear Instruments and Methods in Physics Research Section A: Accelerators, Spectrometers, Detectors and Associated Equipment*, 494(1-3):57 – 62, 2002.

[58] R. D. Cousins. Comments on methods for setting confidence limits. *Workshop on Confidence Limits, held at CERN*, CERN2000-005:49–58, 2000.

[59] A. L. Read. Linear interpolation of histograms. *Nuclear Instruments and Methods in Physics Research Section A: Accelerators, Spectrometers, Detectors and Associated Equipment*, 425(1-2):357 – 360, 1999.

[60] Tom Junk. Sensitivity, Exclusion and Discovery with Small Signals, Large Backgrounds, and Large Systematic Uncertainties. `http://www-cdf.fnal.gov/publications/cdf8128_mclimit_csm_v2.pdf`, October 2007.

[61] Thomas Junk. Confidence Level Computation for Combining Searches with Small Statistics. *Nucl. Instrum. Meth.*, A434:435–443, 1999.

[62] A L Read. Presentation of search results: the cls technique. *Journal of Physics G: Nuclear and Particle Physics*, 28(10):2693–2704, 2002.

[63] A. G. Frodesen, O. Skjeggestad, , and H. Tofte. *Probability and statistics in particle physics / A. G. Frodesen, O. Skjeggestad, H. Tofte*. Universitetsforl., Bergen :, 1979.

[64] Tmva toolkit for multivariate data analysis with root. 2009. `http://tmva.sourceforge.net/`.

[65] John Holland. Genetic algorithms. *Scientific American*, pages 66–72, July 1992.

[66] L. He and N. Mort. Hybrid genetic algorithms for telecommunications network back-up routeing. *BT Technology Journal*, 18(4):42–50, Oct 2000.

[67] Clive Davidson. Creatures from primordial silicon. *New Scientist*, 156(2108):30–35, November 1997.